DAMPING IN ZINC-BASED ALLOYS

HAMID BAJALAN

Doctor of Philosophy

THE UNIVERSITY OF ASTON IN BIRMINGHAM

JANUARY 1993

THE UNIVERSITY OF ASTON IN BIRMINGHAM

DAMPING IN ZINC-BASED ALLOYS

HAMID BAJALAN Ph.D. 1993

THESIS SUMMARY

The damping behaviour of the cold chamber pressure-die-casting alloy: M3, ZA8, ZA27, ZM11, Cosmal, Supercosmal and newly developed ZA27H1 and ZA27H2 was investigated at room temperature and elevated temperatures of up to 90 degrees C. The damping properties of the alloys were established at all temperatures. Formulas were established to predict damping properties of each alloy at any given temperature. The prediction formulae were found to be very accurate. All of the experimental alloys were heterogenous with varying microstructure and grain size; this was the major contribution and dominated the damping properties of the alloys. Supercosmal and ZA27 possessed the highest tensile strength but ZA27H1, ZA27H2 and ZM11 showed the highest damping properties. The relationship between microstructure and damping capacity of all alloys was also examined using back-scattered electron on the SEM. Further more detailed examinations of the microstructures of alloys ZM11, Cosmal and Super cosmal were carried out on the transmission electron microscope in order to establish the phases present in all alloys. These helped to obtain the mechanism of damping in the experimental alloys. The main damping mechanism in most of the experimental alloys was due to grain-boundary-sliding. Micro structural examinations also revealed the absence of ε-phase in the Cosmal and Supercosmal, this was thought to be due to a change in solid solubility of the alloys , which could have been caused by the addition of Si.

Key words: **Damping, Metallography, Die-casting, Zinc-Aluminium alloys.**

DEDICATION

To my parents : for their tolerance, understanding and support over the years.

ACKNOWLEDGEMENTS

I would like to take this opportunity to express my sincerest gratitude to my supervisor Dr. S. Murphy for his ceaseless help, guidance and encouragement throughout the duration of this work.

I wish also to thank my associate supervisor Dr. J.E.T. Penny for his help and fruitful discussions during the course of this work.

I would also express my gratitude to the staff of the Mechanical and Electrical Engineering Department of Aston University, particularly R.Howell, J.Foden, D.Farmer, J.Jeff, B.Muddyman, P.A.Pizer, A.G.Evitts and ex-staff M.J.Scattergood for their valuable assistance.

Particular thanks are due to my colleague Dr.K.Sawalha for his help during the preparation of this thesis.

Last, but not least, I am grateful to my wife Mehrdokht for her valuable support and understanding throughout the period of research.

LIST OF CONTENTS

	PAGE
TITLE PAGE	1
SUMMARY	2
ACKNOWLEDGEMENTS	3
LIST OF CONTENTS	4
LIST OF TABLES	8
LIST OF FIGURES	11
1.0 INTRODUCTION	23
2.0 LITERATURE SURVEY	25
2.1 **Basic concepts and Theoretical Consideration of Structural Damping**	25
2.1.1 Damping Mechanism	27
2.1.1.1 Dislocation Damping	28
2.1.1.2 Twin Boundary Movement	31
2.1.2 Dynamic Hysteresis	32
2.1.2.1 Anelastic Damping	32
2.1.2.1 Behaviour of Grain Boundaries	34
2.2 **Damping Measurement Techniques**	37
2.2.1 Free Decay Method	37
2.2.2 The Half Power point Method	38
2.2.3 Nyquist Diagram (Locus Plot)	41
2.2.4 Low stress Method	48
2.3 **Effect of Variables on Damping Properties**	45
2.3.1 Amplitude of Vibration	45
2.3.2 Frequency of Vibration	46
2.2.3 Temperature	46
2.3.4 Grain Size	47
2.4 **Damping in Zn-Al Alloys**	48

2.5 **The Equilibrium Phase Diagrams** 51

2.5.1 The Binary Zn-Al System 51

2.5.2 The Binary Zn-Cu system 56

2.5.3 The Ternary Zn-Al-Si System 57

2.6 **Phase Transformations** 61

2.6.1 The Binary Zn-Al Alloys 61

2.6.2 The Ternary Zn-Al-Si System 69

2.6.2.1 Alloys of Monotectoid and Eutectic Compositions 69

2.6.2.2 Al-rich Alloys 70

2.7 **Pressure Die-casting Zn-Al Alloys** 71

2.7.1 Commercial Pressure Die-casting Zn-Al Based Alloys 71

2.8 **Effect of Alloying Elements on General properties** 78

2.8.1 Copper 78

2.8.2 Magnesium 78

2.8.3 Silicon 78

2.8.4 Manganese 79

2.8.5 Lead and Tin 79

2.8.6 Cadmium 79

2.8.7 Iron 79

3.0 **EXPERIMENTAL PROCEDURE** 80

3.1 **Alloys** 80

3.1.1 Cosmal Alloys 80

3.1.2 Commercial Pressure Die-casting Alloys 81

3.1.2.1 Preparation of Ingots 82

3.1.2.2 Die Casting of the Alloys 82

3.2 **Damping Tests** 89

3.2.1 Frequency Sweep Method 89

3.2.2 Modal Analysis Method 90
3.2.3 Free Decay Method 91
3.3.4 Q-metre Method 92
3.3 **Metallography** 97
3.3.1 Optical and Scanning Electron Microscopy 97
3.3.2 Transmission Electron Microscopy 98
3.3.2.1 Preparation of Thin Foils 98
3.3.2.2 Transmission Electron Microscopy 99

4.0 **EXPERIMENTAL RESULTS** 101
4.1 **Chemical Composition of Experimental Alloys** 101
4.2 **Metallography of the experimental Alloys** 102
4.2.1 M3 102
4.2.2 ZA8 105
4.2.3 ZA27 Alloys 108
4.2.3.1 ZA27 108
4.2.3.2 ZA27H1 114
4.2.3.3 ZA27H2 114
4.2.4 ZM11 114
4.2.5 Cosmal 123
4.2.6 Supercosmal 131
4.3 **Damping Results** 138
4.3.1 Modal Analysis Method 138
4.3.2 Half Power Point Method 138
4.3.3 Free Decay Method (Q-Metre) 140
4.4 **Tensile Test Results** 151
4.5 **Hardness Test Results** 151

5.0 **DISCUSSION OF THE EXPERIMENTAL RESULTS** 153

5.1 **Metallography of M3** 153

5.2 **Metallography of ZA8** 154

5.3 **Metallography of ZA27** 156

5.4 **Metallography of ZA27H1 and ZA27H2** 158

5.5 **Metallography of ZM11** 158

5.6 **Metallography of Cosmal** 160

5.7 **Metallography of Supercosmal** 163

5.8 **Damping of the experimental Alloys** 165

5.9 **Correlation of Damping Data** 174

5.10 **Tensile and Hardness Properties of the experimental alloy** 176

5.11 **Theoretical and Metallographical Considerations** 177

6.0 **CONCLUSIONS** 181

7.0 **SUGGESTIONS FOR FUTURE WORK** 184

REFERENCES 185

LIST OF TABLES

		PAGE
Table 1	The solid solubility of zinc in aluminium.	54
Table 2	The solid solubility of copper in zinc (52)	56
Table 3	Zinc alloy die casting composition.	72
Table 4	Physical properties of zinc-base casting alloys.	73
Table 5	Mechanical properties of zinc-base casting alloys.	73
Table 6	Chemical composition of zinc-base casting alloys.	74
Table 7	Chemical composition of Cosmal Z-alloys.	80
Table 8	Chemical composition of commercial alloys.	81
Table 9	Chemical alloys of H1 and H2.	82
Table 10	Composition of the experimental alloys (%wt).	101
Table 11	T.E.M. analysis of ZM11.	122
Table 12	T.E.M. analysis of Cosmal.	122
Table 13	T.E.M. analysis of Supercosmal.	
Table 14	Results obtained from modal analysis method, frequency span of 800 Hz.	139
Table 15	Results obtained from modal analysis method, frequency span of 1.6kHz.	139
Table 16	Results obtained from modal analysis method, frequency span 3.2 kHz.	139
Table 17	Results obtained from the half power point method.	140
Table 18	Results obtained from free decay method (ZM11).	140
Table 19	Results obtained from free decay method (Cosmal).	143
Table 20	Results obtained from free decay method (S.Cosmal).	143
Table 21	Results obtained from free decay method (ZA27).	144
Table 22	Results obtained from free decay method (ZA27H1).	144
Table 23	Results obtained from free decay method (ZA27H2).	145

Table 24	Results obtained from free decay method (ZA8).	145
Table 25	Results obtained from free decay method (M3).	146
Table 26	Results obtained from free decay method at elevated temperatures (ZM11).	146
Table 27	Results obtained from free decay method at elevated temperatures (Cosmal).	147
Table 28	Results obtained from free decay method at elevated temperatures (S.Cosmal).	147
Table 29	Results obtained from free decay method at elevated temperatures (ZA27).	148
Table 30	Results obtained from free decay method at elevated temperatures (ZA27H1).	148
Table 31	Results obtained from free decay method at elevated temperatures (ZA27H2).	149
Table 32	Results obtained from free decay method at elevated temperatures (ZA8).	149
Table 33	Results obtained from free decay method at elevated temperatures (M3).	150
Table 34	Tensile test results for all alloys.	152

Table 35	U.T.S. of all alloys at different temperatures.	152
Table 36	Vicker hardness test results (10Kgf load).	151
Table 37	Damping capacity Q^{-1} predictions of experimental alloys at any given temperature.	175

LIST OF FIGURES

		PAGE
Figure 1	A schematic representation of hysteresis loop. Typical of metals at high stress level. By Lazan (18).	26
Figure 2	The K.G.L. Model.	29
Figure 3	Loss coefficient caused by dislocation in linear region for high purity copper. (14).	30
Figure 4	Crystallographical representation of twinning (16).	31
Figure 5	Variation of internal friction with temperature in poly-crystalline and single crystal aluminium.	36
Figure 6	Vibration decay.	39
Figure 7	Amplitude - Frequency response, single resonance.	40
Figure 8	Amplitude frequency response, frequency multi resonance.	42
Figure 9	Receptance vector locuse for a system with viscous damping.	44

Figure 10	The effect of temperature on the damping capacity of Zinc-Aluminium alloy (28).	49
Figure 11	Variation of damping capacity with shear stress for zinc-aluminium alloy (28).	50
Figure 12	Zinc-Aluminium phase diagram compiled by Anderko (53).	52
Figure 13	Accepted phase diagram of binary zinc-aluminium system.	53
Figure 14	The equilibrium phase diagram of binary Zn-Cu system.	55
Figure 15	Isothermal section of Zn-Al-Si system at 350° C.	58
Figure 16	Isothermal section of Zn-Al-Si system at 300° C.	59
Figure 17	Isothermal section of Zn-Al-Si system at 280° C.	59
Figure 18	Isothermal section of Zn-Al-Si system at 272° C.	60
Figure 19	Isothermal section of Zn-Al-Si system at 230° C.	60
Figure 20	A scheme of transformation in Zn Al alloys according to Toldin et al (91).	66

Figure 21	Phase diagram of Zn-Al system with metastability boundaries (a, b).	67
Figure 22	Variation of U.T.S.of alloys M3, ZA27 with temperature.	75
Figure 23	Variation of 0.2% proof stress of alloys M3, ZA8 and ZA27 with temperature.	76
Figure 24	Variation of the % elongation of alloys M3, ZA8 and ZA27 with temperature.	76
Figure 25	E.M.B. 10B Cold-chamber die casting machine.	84
Figure 26	Die cavity design for thin section plates.	85
Figure 27	Decrease of the section along the flow path of the feed system of the die.	87
Figure 27a	An example of the actual casting with runner system.	87
Figure 28	Schematic diagram of the instrumentation set-up used in the half power point method.	93
Figure 29	Schematic diagram of the instrumentation set-up used in the modal analysis method.	94

Figure 30	Schematic diagram of the instrumentation set-up used in the free decay method.	95
Figure 31	Schematic diagram of the instrumentation set-up used in the Q-meter method.	96
Figure 32	Instrumentation set-up used in the Q-meter method.	100
Figure 33	The electropolisher (Tenupol, Struers Ltd).	100
Figure 34	SEM as-cast structure of M3 showing primary η of different sizes surrounded by the eutectic, also seen in this figure is some gas porosity.	103
Figure 35	SEM as-cast structure of M3 showing primary η of different sizes surrounded by the eutectic, which is in lamellar or particulate form.	104
Figure 36	SEM as-cast structure of M3 showing a few former β particles formed on the primary η particles, also present are some pseudoprimary β in the bottom right hand corner.	104
Figure 37	SEM as-cast structure of ZA8 showing primary β particles of different sizes and shapes surrounded by eutectic η particles of similar size and shape as the primary β are also present in this figure, at the left hand edge some shrinkage porosity can also be seen.	105

Figure 38	SEM as-cast structure of ZA8 showing a variety of decomposition structures in the former β dendrites, and lamellar eutectic morphologies.	106
Figure 39	SEM as-cast structure of ZA8 showing decomposed β and eutectic matrix, figure also shows some particulate eutectic morphologies.	106
Figure 40	SEM as-cast structure of ZA8 showing decomposed β and eutectic matrix. The figure focused on a peculiar shaped β dendrite.	107
Figure 41	SEM as-cast structure of ZA8 using different contrast to figure 40 showing the decomposition of β into nicely formed lamellae and a coarse mixture of phases at the edge.	107
Figure 42	SEM as-cast structure of ZA27, showing dark phases of fine α' dendrites surrounded by β with small amounts of interdendritic η.	109
Figure 43	SEM as-cast structure of ZA27 showing a fine structure of former α' particles surrounded by β and interdendritic η.	109
Figure 44	SEM as-cast structure of ZA27 showing the decomposed α' and β.	110

Figure 45	SEM as-cast structure of ZA27 showing the decomposition of α' particles.	110
Figure 46	SEM as-cast structure of ZA27 at high magnification showing the final product of decomposition of α' and β.	111
Figure 47	SEM as-cast structure of ZA27H1 showing α' dendrites surrounded by β with small amounts of interdendritic η, also seen are some rod like intermetallic particles.	112
Figure 48	SEM as-cast structure of ZA27H1 showing the decomposition of α' into fine particles or lamellar products.	112
Figure 49	SEM as-cast structure of ZA27H2 showing a fine structure of former α' primary particles surrounded by β and interdendric η, also present in this figure are some silicon particles.	113
Figure 50	SEM as-cast structure of ZA27H2 showing the decomposition of α' into particles.	113
Figure 51	SEM as-cast structure of ZM11 showing the former α' dendrites in a mixture of transformed β and eutectic η. The dark particles are silicon.	116

Figure 52	SEM as-cast structure of ZM11 showing a coarse mixture of $\alpha+\eta$ (eutectoid), also present are some silicon particles which are associated with the α'.	116
Figure 53	SEM as-cast structure of ZM11 showing an α dendrite with nicely formed lamellae.	117
Figure 54	SEM as-cast structure of ZM11 showing Figure 53 at higher magnification, showing nicely formed patterns of cellular decomposition in α and β. The cells are nucleated on the η and thickened as they grew into the α' phase.	117
Figure 55	TEM as-cast structure of ZM11 taken from an α dendrite showing lamellar arm branching out from the centre in a three dimensional network sectioned by the plane of the thin foil. The irregular mats of dark particles are oxides formed during electro-polishing.	118
Figure 56	TEM as-cast structure of ZM11 taken from the edge of the α dendrite showing the lamellae arms, also enclosed within these arms were precipitates of different sizes and shapes.	118
Figure 57	TEM as-cast structure of ZM11 at high magnification showing large precipitates (arrowed) enclosed within the lamellae, these precipitates were analysed and were found to be α_m phase.	119

Figure 58	TEM as-cast structure of ZM11 (the numbers on this micro-graph are the points of analyses).	119
Figure 59	a) SADP taken from the arrowed area on Figure 57, showing a diffraction pattern with a beam direction of [211] α. b) Indexing of the above pattern	120
Figure 60	Stereographic projection of Al, with the great circle on which points of indexing lie marked.	121
Figure 61	SEM as-cast structure of Cosmal showing α' dendrites with different sizes and shapes and a mixture of β and η, and a eutectic matrix of α+Si.	124
Figure 62	SEM as-cast structure of Cosmal showing aluminium-rich α' phase surrounded by spinodally decomposed β.	124
Figure 63	SEM as-cast structure of Cosmal showing a higher magnification and at two different contrasts to highlight that the lamellar decomposition of β stops when reaching the α phase.	125
Figure 64	TEM as-cast structure of Cosmal alloy showing a zinc-rich area surrounded by spinodally decomposed β.	126

Figure 65	TEM as-cast structure of Cosmal showing decomposed β particles in the centre surrounded by α' phase.	126
Figure 66	TEM as-cast structure of Cosmal showing an interdendritic η region in the centre surrounded by eutectic β phase. SADP taken from the arrowed area.	127
Figure 67	TEM as-cast structure of Cosmal showing on the right hand side the eutectic η phase and on the left-hand side a decomposed β phase. (The numbers on this micro-graph are the points of analyses.	127
Figure 68	TEM as-cast structure of Cosmal showing decomposed β, also shown in this figure, are fine precipitates. (The numbers on this micrograph are the points of analyses).	128
Figure 69	a) SADP taken from the arrowed area on Figure 66, showing a diffraction pattern with a beam direction of [1011] η. b) Indexing of the above pattern.	129
Figure 70	Stereographic projection of Zn with the great circle on which points of indexing lie marked.	130
Figure 71	SEM as-cast structure of Supercosmal showing the α' phase and a mixture of β and η.	132

Figure 72	SEM as-cast structure of Supercosmal showing aluminium-rich α' phase surrounded by decomposed β, also seen are some silicon particles associated mainly with the α' phase.	133
Figure 73	SEM as-cast structure of Supercosmal showing a higher magnification mottled contrast due to the decomposition of α' cores.	133
Figure 74	SEM as-cast structure of Supercosmal at higher magnification and different contrast to show lamellar decomposition of the β regions.	134
Figure 75	TEM as-cast structure of Supercosmal showing spinodal decomposition of α' and also showing a decomposed β particle (numbers on this micrograph are the points of analysis).	135
Figure 76	TEM as-cast structure of Supercosmal showing a decomposed β particle which had produced lamellae with different orientations.	135
Figure 77	TEM as-cast structure of Supercosmal showing discontinuous decomposition of α' dendrite cores into a lamellar final product, also seen in this figure, a silicon rich particle.	136

Figure 78	TEM as-cast structure of Supercosmal showing a Si-rich particle taken from Fig. 77 after tilting the specimen to high-light the Si-rich area. (The number on this micrograph is the point of analyses).	136
Figure 79	a) SADP taken from the arrowed area on Fig. 75, showing a diffraction pattern with a beam direction of [013] α' b) Indexing of the above pattern.	137
Figure 80	Frequency response curve showing the first mode of vibration.	141
Figure 81	Frequency response curve showing the first two modes of vibration.	141
Figure 82	Frequency response curve showing the first three modes of vibration.	141
Figure 83	Frequency response curve showing the first two modes of vibration.	142
Figure 84	Frequency response curve showing the magnification of one of the modes of vibration.	142
Figure 85	The damping capacity of the experimental alloys as obtained by the modal analyses method.	169

Figure 86	Damping capacity v frequency of vibration. (modal analyses method).	171
Figure 87	Damping capacity v frequency of vibration. (half power point method).	170
Figure 88	The damping capacity of the experimental alloys as obtained by the half power point method.	169
Figure 89	Damping capacity of the experimental alloys as obtained by the free decay method.	172
Figure 90	Damping capacity of the experimental alloys at elevated temperatures.	173
Figure 91	U.T.S. v temperature.	180

CHAPTER 1

1 INTRODUCTION

The term 'damping' has been defined by Lazan (9) as the energy dissipation properties of a material or system under cyclic stress. In most cases, a conversion of mechanical energy to heat is involved. Within the context of this definition, energy must be absorbed and dissipated within the specific system before the term 'damping' is applicable. Once the energy has been accepted by the structure in modes of vibration, it will either be dissipated internally or re-radiated back into the space. The former is the internal damping and the latter, the radiation damping. Material damping, sometimes called internal friction, internal damping or hysteretic damping, is related to the energy dissipation in a volume of macro-continuous media.

In general, material damping is associated with the energy dissipation which takes place when a more or less homogeneous volume is subjected to cyclic stress and the damping mechanisms are associated with the internal micro and macro-structure of the material.

It has been known for some time that certain zinc aluminium alloys fall into the category of alloys with high damping capacity. Some industrial designers of engineering structures are becoming aware of the cost-effectiveness and simplicity of using the intrinsic damping capacity of a well-chosen, high damping material to attenuate the mechanical vibration of the structure from which it is built. Others are not yet aware of the potentials of high damping alloys, and it is part of the material scientist's job to characterise the intrinsic

damping capacity of these alloys and bring it to the attention of designers. Of course in choosing an alloy with high damping properties for a given application, strength, corrosion resistance and a whole host of other physical properties must be considered, as well as its intrinsic damping capacity.

The object of this work is therefore, to determine the damping capacity of several commercial and newly developed high damping alloys at room temperatures and elevated temperatures and to compare damping properties to their other physical properties.

CHAPTER 2

2.0 LITERATURE SURVEY

2.1 Basic Concepts and Theoretical Consideration of Structural Damping

Damping capacity is important as a means of limiting the stresses and amplitudes of vibration in materials and structures. When a structure is subjected to forced vibration at a frequency corresponding to the natural or resonance frequency of the structure, a small exciting force will induce large vibratory inertia force and thus cause severe stresses in the members. Neglecting energy losses by air damping and those absorbed in the base of the structure, only the damping capacity of the structure can keep the amplitude of these vibrations from increasing indefinitely. A material with high damping capacity is therefore more effective in limiting resonance vibration than a low damping material. However, a simple comparative list of relative damping constants alone is of little value to the designer since other factors such as fatigue strength, modulus of elasticity and stress distribution also play a part in determining the resonance strength of a material (7).

High damping materials may conveniently be divided into two groups; organic systems and metallic systems. Viscoelastic damping coating is easily contaminated by its environment (oil, water, etc) and it is useful only over limited frequency and temperature ranges. Certain metals however, are strong and tough for structural applications and also possess high inherent damping that is independent of frequency and less temperature dependent than that of plastics (8).

Many types of variables, loads and environments are encountered in service and a large variety of inelastic mechanisms dissipate energy. In all cases however, materials or structural systems that dissipate energy under cyclic loading display one phenomenon in common; the cyclic load-deformation (or stress-strain) curve is not a singularly valued function, but forms a hysteretic loop. Since energy is absorbed by a materials system under cyclic load, the unloading branch of the loop must lie below the loading branch as shown in Figure 1. The area between these two branches (the area within the hysteretic loop) is proportional to the energy absorbed. The energy dissipation property so defined is identified by the term "damping".

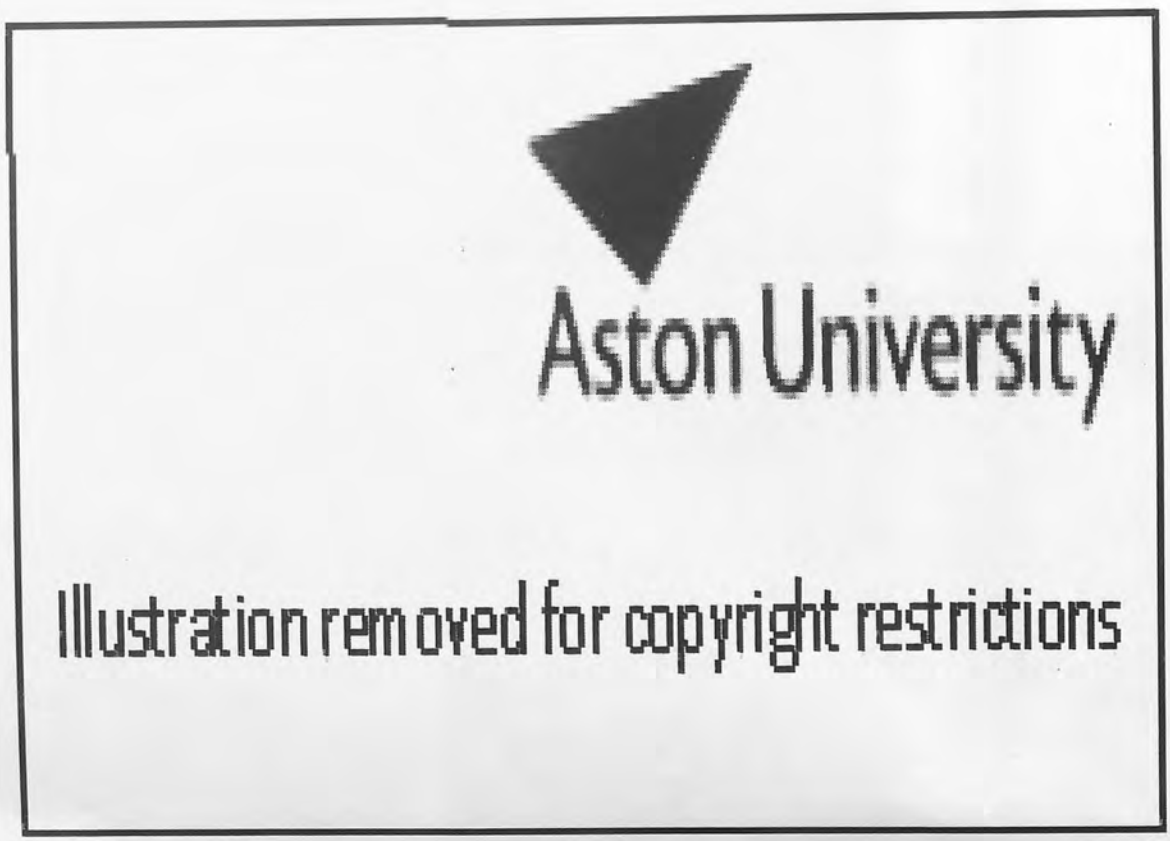

Fig 1. A schematic representation of hysteresis loop. Typical of metals at high stress level. By Lazan (18)

2.1.1 Damping Mechanism

A high damping material is one which possesses a facility for the conversion of mechanical (vibrational) energy into an alternative form, usually thermal energy. The mechanisms responsible for this conversion may conveniently be divided into two groups. The first group is characterised by complete, though relatively slow recovery of the small residual strain that occurs when a low stress is applied and removed. These are termed 'dynamic hysteretic mechanisms' and are often diffusion-controlled. The second group contains systems which leave a small permanent set. This residual strain can be removed only by a reversed stress. Frequencies in the megacycle range are required to prevent this 'hysteretic' strain occurring. In the most widely used damping tests, these high frequencies are never encountered. Consequently, stress relaxation appears to be instantaneous and the mechanisms are therefore termed 'static hysteretic' (10).

We will first look at static hysteretic where damping is independent of the frequency of the cyclic stress wave passing through the material (the vibration) but is strongly dependent on its amplitude.

Examples are:

a) Dislocation motion

b) Twin boundary movement

2.1.1.1 Dislocation Damping

During the past years considerable attention has been given to the problem of constructing a dislocation theory capable of quantitatively discribing the part of the internal friction and modulus change in metals.

Where dislocation motion contributes to the total strain produced by a specified stress under alternating stress, the dislocation component of the strain may lag behind the applied stress, thus forming a hysteretic loop and contributing to the dissipation of energy. Estimates of the magnitude of this effect for typical dislocation densities, assuming that the dislocations are perfectly mobile with no restrictions on their motion, yield a much larger value than that observed experimentally. Impediments to the motion of dislocations or other types of interactions must therefore be present. Examples of such impediments are pinning points, network points, jogs, and other dislocations.

One generally accepted dislocation model for damping is that proposed and developed by Koehler (11) and by Granato and Lucke (12-14) known as the KGL theory. In this model dislocation motions are viewed as being analogous to a vibrating string in a viscous medium, and an equation for the motion can be written considering the effective mass per unit length and the effective tension in the dislocation.

This model is shown schematically in Figure 2. The successive drawings indicate schematically the bowing out of a pinned dislocation line by an increasing applied stress. The length of the loop determined by impurity pinning is denoted by Lc, and that determined by the network by Ln. As the stress

increases, the loops Lc bow out until break-away occurs. For very large stresses, the dislocations multiply.

Figure 2. The K.G.L. model.

Dislocation damping in the linear region is a function of frequency similar to that observed for anelastic phenomena. At low frequencies the velocity of the dislocation is small so that the viscous force and damping are small.

Under these conditions the displacement is limited by the tension forces in the dislocation and it is parabolic in shape as shown by the Lf arcs in Figure 2c.(15) As the frequency increases, the viscous forces become dominant and the displacement of the dislocation cannot achieve its full parabolic values, under these circumstances it behaves like a rigid rod except for curvature at its ends near the pinning points as shown by Hf lines in Figure 2c. At very high

frequency the drag force may be large but the displacement is very small, thus damping is small. At some intermediate or optimum frequency the integral of drag force and displacement is maximum and thus the damping is maximum. As a result the damping versus frequency curve displays a typical relaxation or resonance type peak. this is illustrated in figure 3, for high purity Copper.

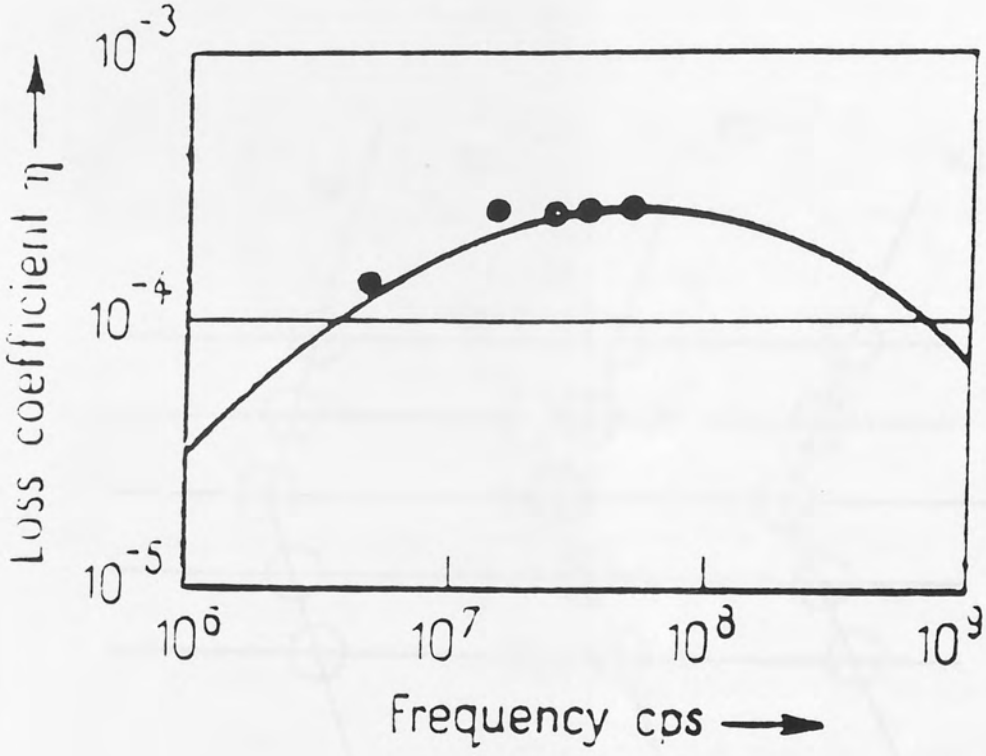

Figure 3. Loss coefficient caused by dislocations in linear region for high purity copper.(14)

2.1.1.2 Twin Boundary Movement

Some metals and alloys deform plastically under an applied stress by the formation of deformation twins.

Crystallographically, twinning can be represented by the reflection of the crystal across a plane called the twin plane, or alternatively, by a rotation of one part of the crystal through 180 degrees about an axis perpendicular to the twin plane.

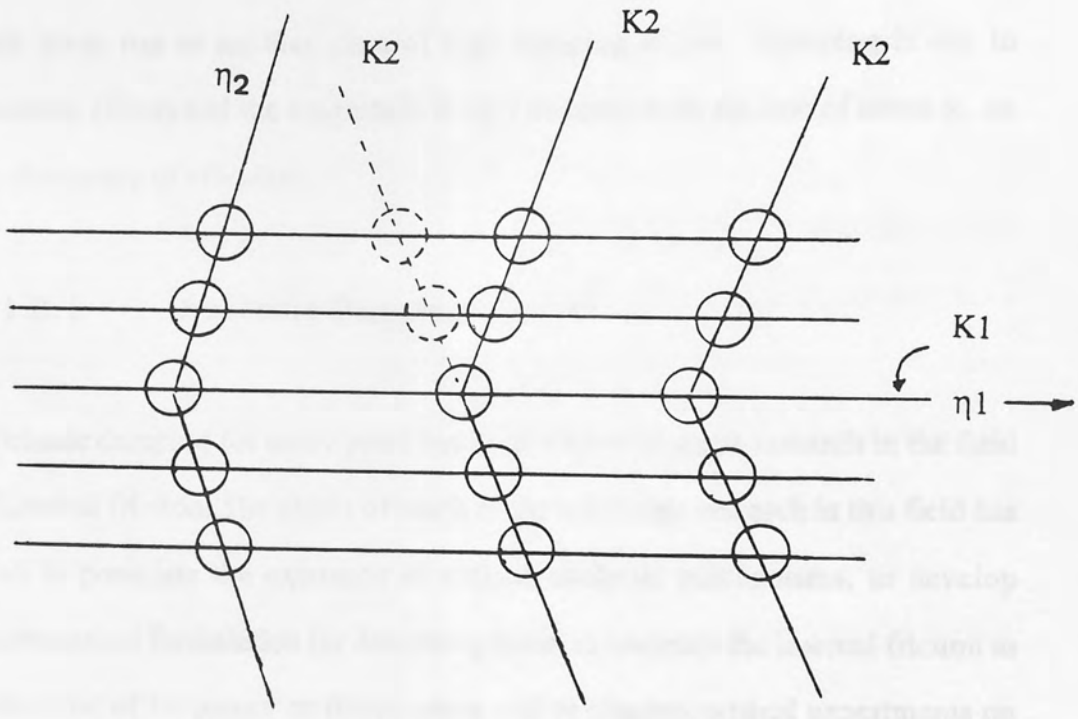

Figure 4 Crystallographical representation of twinning (16)

Figure 4 shows that twinning can occur if each layer of atoms parallel to the twin plane is sheared relative to its neighbour by an amount which is less than that needed to move the layer to equivalent positions in the crystal.

Normally, it is expected that twin formation would take place at stress levels above the yield point, but if the shear is small and the grain size large, deformation twins may start to form at low stresses. The larger the stress, the more twins will form, hence the amplitude dependence of this form of damping.

2.1.2 Dynamic Hysteresis

This gives rise to another class of high damping alloys. Damping is due to anelastic effects and the magnitude is very dependent on the rate of stress ie. on the frequency of vibration.

2.1.2.1 Anelastic Damping

Anelastic damping for many years has been subject of much research in the field of internal friction. The object of much of the solid-state research in this field has been to postulate the existence of various anelastic mechanisms, to develop mathematical formulation for describing these, to compute the internal friction as a function of frequency or temperature, and to conduct critical experiments on internal friction to check the validity of the mechanisms postulated (17). Such work has been fruitful in clarifying important anelastic mechanisms and in refining their microstructural basis.

The values of internal friction observed in anelasticity studies are generally found to be independent of stress amplitudes. However, damping is generally found to

be dependent on frequency and temperature, and in various critical ranges of these variables sharply peaked values of the loss coefficient (η) are often observed. Each of these peaks in the curves for η versus frequency (or temperature) can generally be associated with some physical machanisms operating in the materials under cyclic stress in such a way as to dissipate maximum energy under some optimum condition.

In addition to above, several types of anelastic relaxation peaks have been identified. Three of these are the Snoek effect, Stress-induced ordering and an electronic effect.

The Snoek effect (107) is associated with presence of interstitial carbon or nitrogen impurity atoms in Iron or Steel and their motion under cyclic stress.

Ordering effects induced by stress can also cause relaxation peaks. In an unstressed specimen the interstitial atoms within a metal lattice generally have random distribution. The application of stress tends to produce atom motions that give rise to an increase in lattice order. Under cyclic stress the cyclic re-distribution of interstitial atoms through a diffusion process leads to internal friction and characteristic relaxation peaks. In hardened and tempered austenitic steel, for example, carbon diffusion phenomena provide the damping mechanism.

Relaxation peaks have also been associated electronic effects. At very low temperatures at frequencies in the megacycle range the internal friction has been observed to increase rapidly with increasing frequency. Since the magnitude of internal friction decreases rapidly as the metal passes from the normal to the

superconducting state, the mechanism involved has been associated with the presence of free electrons.

2.1.2.2 Behaviour of Grain Boundaries

Grain boundaries are in a relatively disordered state and thus display viscous-like properties. The unit of energy dissipated in the grain boundaries under cyclic shear stress or strain is therefore larger, in general than that dissipated within the grain. The internal friction associated with grain boundary shear depends on the shear and relaxation properties of the grain boundary (a function of temperature) and also on strain rate (or frequency).

The phenomenon of grain boundary sliding was discovered by Ke (27) who discovered an internal friction peak in the relaxation spectrum of polycrystalline aluminium which was not found in single crystals, Figure 5.

Ke showed that when the temperature is high enough, disordered materials in the boundaries can be rearranged so that the boundary shear stresses are relieved. This process is thermally activated and to accomplish the rearrangement, the grains must undergo relative sliding motion. The internal friction is reflected by the energy dissipated as grain boundary strain energy is relieved. A peak energy is produced where the viscosity is not too large to allow energy dissipation and not too small to allow energy storage.

Because this mechanism is thermally activated, it is associated with a relaxation time, τ, which is dependant on temperature through an activation energy hence an equation can be produced.

$$\tau = \tau_o \exp(-\Delta H/RT)$$

Where τ_o = constant

ΔH = activation energy

R = gas constant

T = temperature ^oK.

For a fixed frequency of vibration it is possible to show an internal friction peak will occur at,

$2\pi F\tau = 1$ F = frequency of vibration

Ke postulated that damping peak in polycrystalline aluminium was due to shear stress relaxation by sliding at the grain boundaries, limited by the elastic constraints at the grain corners, Ke produced an equation for viscous sliding,

$$P^{\cdot} = A\sigma \exp(-\Delta H/RT)$$

Where $P^{\cdot}$ = velocity of sliding

A = constant

σ = shear stress at boundary.

The calculated activation energy was found to be equal to that for self-diffusion.

Most investigators are convinced that shear stress relaxation at the grain boundaries is the mechanism which produces the damping peaks. However this theory can not explain some phenomena easily, such as the presence of two peaks in substitutional alloys, the increase in activation energy due to alloying elements, and the variation of peak height with grain size.

The theories of anelastic sliding are numerous. Ke deduced that the boundary acts as a viscous layer a few atoms wide, and that the basic act of sliding was adjacent atoms squeezing past each other, thus providing an equation,

$$P^{\cdot} = K\sigma/RT \exp. (-\Delta H/RT)$$

The activation energy corresponding to that for grain boundary self-diffusion.

Other investigators discount the hypothesis of a viscous layer completely. Some investigators have based their theory on a dislocation mechanism. Sliding takes place by movement of partial dislocations parallel to the boundary plane. This theory does not produce a satisfactory sliding mechanism, though structures which are analagous to dislocation could exist in the boundary plane which may play some part in sliding.

The mechanism of grain boundary sliding is one of the most important in producing high damping capacities, particularly in alloys which exhibit a very fine grain size, a good example is the zinc-aluminium eutectoid alloy.

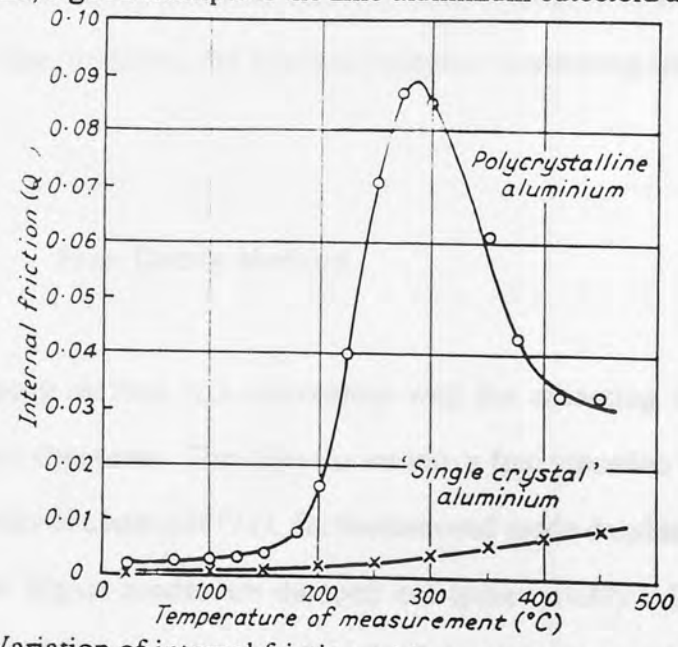

Figure 5. Variation of internal friction with temperature in polycrystalline and single crystal aluminium

2.1 DAMPING MEASUREMENT TECHNIQUES

Modal identification of structures to experimentally determine natural frequencies, mode shapes and damping factors, is critical to the accurate mathematical modelling of structures. These extracted modal parameters, besides being directly related to the physical parameters of the structures, are very useful in applications such as response and load predictions, trouble shooting excessive vibrations, stability and control, verification and/or modification of analytical dynamic models, structural integrity monitoring and incipient failure detection, design against fatigue among others (19).

While undampened natural frequencies and normal mode shapes can be estimated from analytical models, damping characteristics of structures and high damping alloys are determined mainly from experimentation. Even with the tremendous advances in the 'state of the art' of modal identification in both frequency and time domains, the accuracy of damping identification, unlike frequencies and mode shapes, is an area of active current research efforts. Damping identification accuracy becomes more critical in applications such as incipient failure, detection and structural integrity monitoring and fatigue design (20).

2.2.1 Free Decay Method

The free decay method is a convenient way for assessing the damping in materials and structures. The object is set into a free vibration by a shock load such as a strike of a hammer (21), the fundamental mode dominates the response since all the higher modes are damped out quite quickly. It is not usually possible to excite any mode other than the fundamental using this method. By

measuring and recording the decay in the oscillation the logarithmic decrement " λ " is found. Figure 6.

$$\lambda = \ln \frac{\text{(Amplitude of motion)}}{\text{Amplitude of motion one cycle later}} .$$

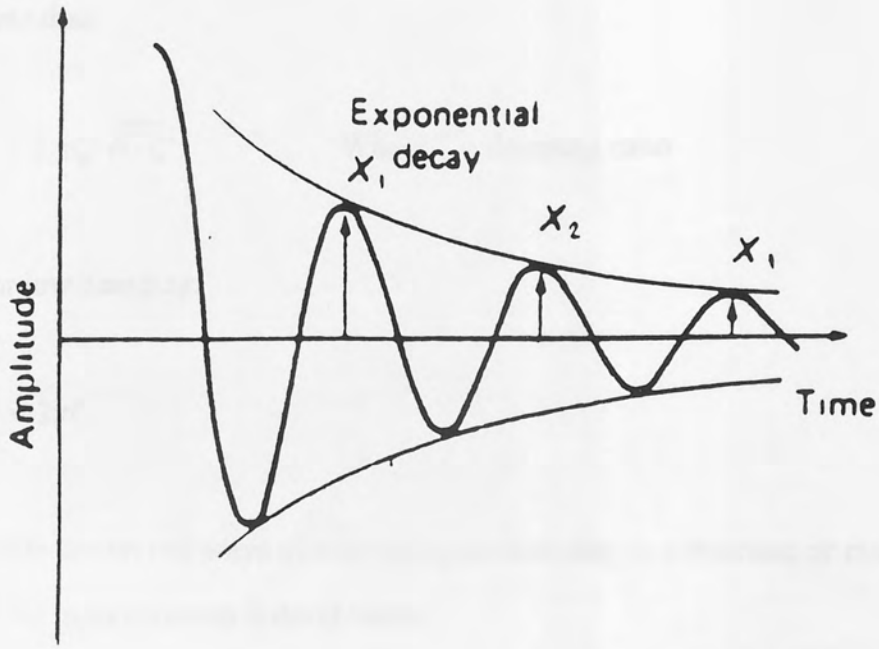

Figure 5 Vibration decay

For viscous damping:

λ = Ln(X1/X2) = (In(X2/X3) = In(X3/X4) = ...In(Xn-1/xn)

Where λ = logarithmic decrement

Thus,

n λ = in X1/X2. X2/X3 .....Xn-2/Xn-1. Xn-1/Xn

Therefore,

$\lambda = 1/n.\ \mathrm{Ln}(X1/Xn)$

Which is a useful expression to use if λ is small

Note that:

$\lambda = 2\pi\zeta/\sqrt{1-\zeta^2}$ Where ζ = damping ratio

For low damping:

$\lambda = 2\pi\zeta$

There are several ways of expressing the damping in a structure or material, one of the most common is the Q factor.

When a structure is forced into resonance by a harmonic exciting force, the ratio of the maximum dynamic displacement at steady state condition to the static displacement under a similar force is called the Q factor (22).

That is $Q = \frac{\text{Xmax dyn}}{\text{Xmax static}} = \frac{1}{2\zeta}$

2.2.2 The Half Power Point Method

This technique is widely used since it basically uses the same equipment used for free decay method (23).

Since structures can be excited into resonance at any of their modes, a 'Q' factor can be determined for each mode. This can be achieved by carrying out a resonance test. Figure 7 shows a typical response.

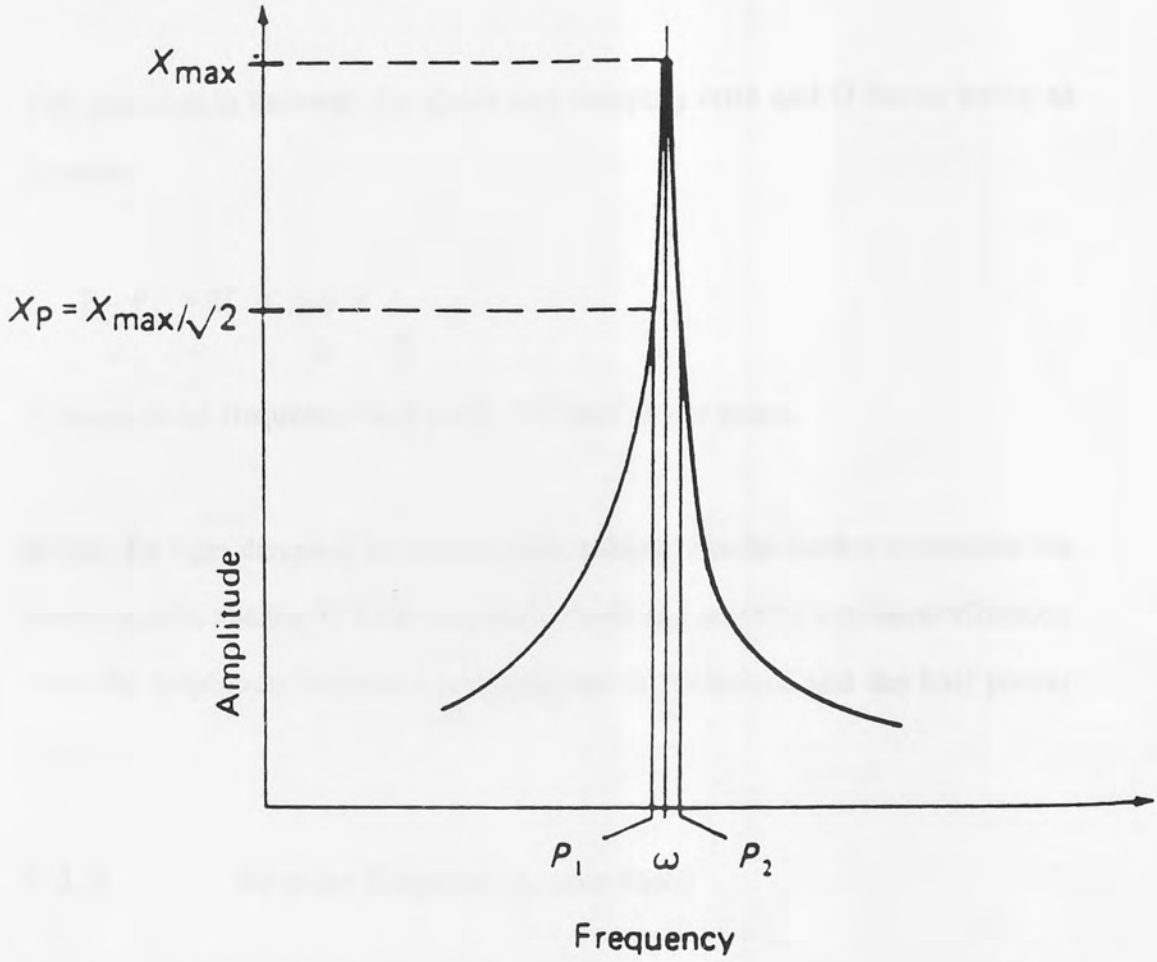

Figure 7: Amplitude - Frequency response, single resonance.

This method of measurement requires very accurate measurement of the vibration amplitude for extraction frequencies in the region of resonance.

If damping is assumed to be light, as for most materials:

ω= undamped frequency

$\omega = k/m$ where k = stiffness

m = mass

at the mode of vibration considered

Then $Xp = Xmax / \sqrt{2}$

and the corresponding frequencies either side of 'ω' are P_1 and P_2.

The relationship between the above and damping ratio and Q factor being as follows:

$$\frac{P_2 - P_1}{\omega} = 2\zeta = \frac{\Delta\omega}{\omega} = \frac{1}{Q}$$

Where ω is the frequency band width the half power point.

Hence, for light damping the above relationships, can be used to determine the damping ratio and the 'Q' factor associated with any mode of structural vibration from the amplitude frequency measurement at resonance and the half power points.

2.2.3 Nyquist Diagram (Locus Plot)

Another measure of the damping in materials and structures is the relationship between the component of response that is in-phase with the force (real) and the component 90 degree out of phase (imaginary), as plotted in the complex plane as a Nyquist diagram (24).

It is sometimes difficult to use the half power point method accurately to measure damping when a mode exhibits extremely low damping. This will produce a large % error in 'ω' because it is so small. Another difficulty arises when modes are very close together that they interfere with each other, and the half power points cannot be accurately found from this data, as shown in Figure 8.

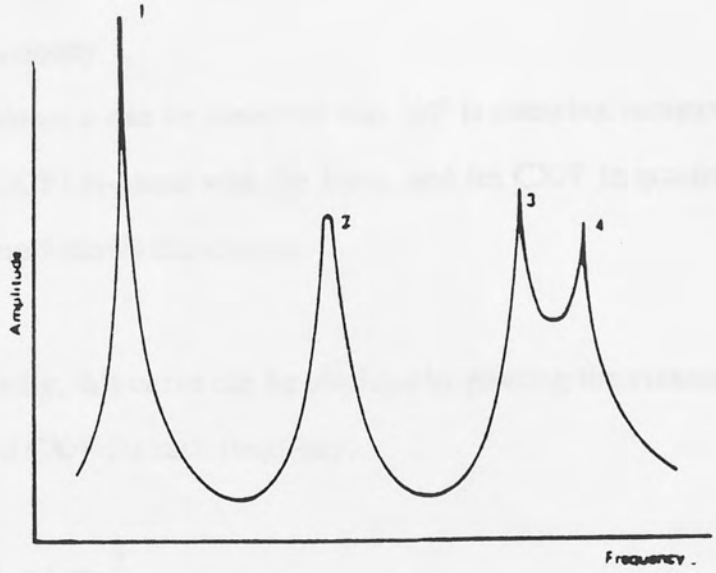

Figure 8. Amplitude frequency response, frequency multi resonance.

It is possible however, to improve the accuracy of measurement by measuring both amplitude and phase of response for a range of exciting frequencies. Consider a single degree of freedom system represented by the differential equation.

$$m\ddot{x} + c\dot{x} + kx = Fe^{jvt}$$

Where c = coefficient of viscous damping

F = exciting force amplitude

When $x = Xe^{jvt}$

Where x = displacement , and X = amplitude of motion

Then $-mv^2 X + jcvX + kX = F$

Hence $X/F = \frac{k-mv^2}{(k-mv^2)^2+(cv)^2} - j \frac{cv}{(k-mv^2)^2 + (cv)^2}$.

Where v = velocity

From the above it can be observed that X/F is complex receptance with two vectors Re(X/F) in-phase with the force, and Im CX/F in quadrature with the force. Figure 9 shows this clearly:

Experimentally, this curve can be obtained by plotting the measured amplitude and phase of CX/F for each frequency.

Since $\tan\phi = \frac{k-mv^2}{cv}$

when ϕ = 45 degrees and 135 degrees

then $mp_1^2 + cp_1 - k = O$ and $mp_2^2 - cp_2 - K = 0$

Subtracting gives;

$p_2 - p_1 = c/m$

or

$$\frac{P_2 - P_1}{\omega} = \frac{\Delta\omega}{\omega} = 2\zeta = \frac{1}{Q}$$

This method is even more effective when the damping is hysteretic because in this case, the locus of (X/F) as 'v' increases from zero as a path of a circle, centre (0 ,- 1/2 η k)* and radius 1/2 ηk. In this case, it is very easy to draw an accurate locus from a few experimental results, and hence find P_1 and P_2.

* where η = damping loss factor.

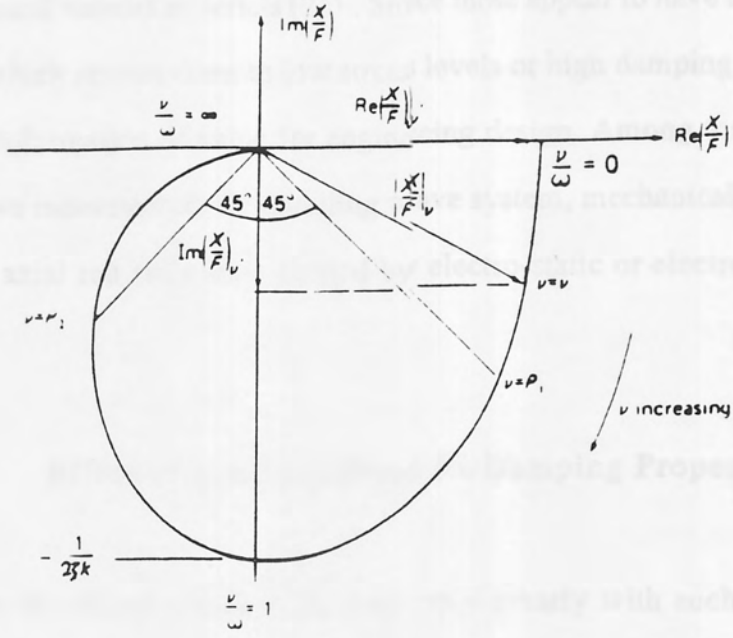

Figure 9. Receptance vector locus for a system with viscous damping.

2.2.4 Low Stress Methods

A number of low stress devices are in use to investigate the physical characteristics of various materials (25) . Since these appear to have fundamental limitations which restrict them to low stress levels or high damping value, they do not give information of value for engineeing design. Among these (26) are standing wave measurement in travelling wave system, mechanical impedance bridges and axial rod resonance excited by electro-static or electro-magnetic devices.

2.3 Effect of some variables on Damping Properties

In any alloy the damping properties may vary greatly with such factors as amplitude of vibration, frequency of vibration, temperature and grain size just to name a few. A combination of these factors, which are usually encountered, complicate the process of damping capacity measurement. For this reason the influence of each must be understood.

2.3.1 Amplitude of Vibration

Material is subjected to cyclic stress conditions when vibrated with repeated reversal of the direction of stress. As the amplitude of vibration is increased, so does the strain that the specimen undergoes, with a maximum at the extremes of amplitude.

Many attempts have been made to correlate vibration amplitude and damping capacity, Brophy (34) found for steel that damping is proportional to the cube of

the amplitude. Kimball (35) related damping as a function of amplitude and frequency.

However, there is a lack of agreement between these generalisations except that they all agree that amplitude has an effect on damping.

2.3.2 Frequency of Vibration

This can be critical in its effect on damping capacity, particularly when diffusion processes are involved in the damping mechanism.

If the frequency is high, then the period of vibration may be too short to allow a particular diffusion process to occur, before the next half cycle reverses the stress. However, if the frequency is very low, the process takes such a small portion of each cycle that its effect is negligible. Thus, if the process was diffusion controlled, then the rate of energy absorption would be so low that its damping would be low. However, there will be a frequency which has a period corresponding to the relaxation time of the material, thus neither of these factors has an effect and damping reaches a maximum at this frequency.

2.3.3 Temperature

At vibration amplitudes the effect of increasing the temperature of the specimen is to increase the damping capacity, due to increases in plasticity and diffusion rate. This phenomenum is demonstrated in Figure 10. The effect is more complicated at low amplitudes.

This of particular importance in materials which have diffusion controlled damping mechanisms, for example grain boundary sliding in the Zinc-Aluminium alloys.

A complication which does arise with increased temperature, is that grain growth can occur above the recrystallisation temperature, thus creating a change in the damping capacity.

2.3.4 Grain Size

The grain size of a metal has a marked effect on the damping properties. There are two main effects produced by a change in grain size. The first effect is that an increase in grain size increases in effect the relaxation time of the metal. Therefore, maximum damping capacity is achieved under certain conditions.

The second and more important effect of grain size, is how to control the amount of grain boundary present; the amount increasing as the grain size decreases. Thus, a specimen which has a sufficiently small grain size has as its major damping mechanism the absorption of energy by grain boundary sliding, the classic case being the Zinc-Aluminium alloys.

2.4 Damping in Zn-Al Alloys

The zinc-aluminium eutectoid alloy (78%wt zinc and 22%wt aluminium) has been studied and is well known for its superplastic behaviour. It has only recently become known as an alloy with high damping capacity under the same conditions which produce superplasticity (28).

In these alloys superplasticity is produced by quenching from a temperature greater than 275 degrees C. Nuttall and Nicholson (29) recommend 3 hours at 380 degrees C while Chaudari (30) used 24 hours at 350 degrees C. This treatment produces the prerequisite of superplasticity that is an extremely fine equiaxed grain size. The coarse grain high temperature phase when quenched gives a metastable structure, this however quickly decomposes to produce a two-phase equilibrium state of ultra fine grain size, which is known as a microduplex structure (31).

Investigations carried out into the mechanism of superplastic deformation indicate the importance of grain boundary sliding (29, 30, 34, 35).

Because of the grain boundary sliding which occurs in these alloys it is not surprising that high damping capacity is produced in these alloys. The damping of Zn-Al alloys is dependent upon temperature, the damping capacity being only 10% at 50 degrees C while increasing to 85% at 200 degrees C, as shown in Figure 10. The production of a damping peak is strong evidence for the damping mechanism to be grain boundary sliding, the temperature of peak damping corresponds to the temperature of maximum superplastic properties, where grain boundary sliding is a maximum.

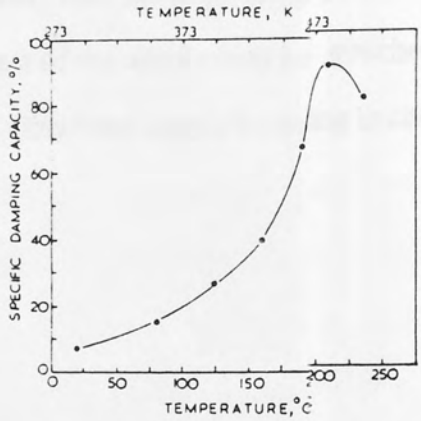

Figure 10. The effect of temperature on the damping capacity of Zinc-Aluminium alloy (28).

A fairly good damping capacity can still be produced in slow cooled alloys, though not as high as in the quenched alloys. A relaxation peak is not observed in the slow cooled alloy, maximum damping is produced at the phase transformation temperature. Nuttall (28) suggested a process of coupled relaxations between interfaces on the damping mechanism, a concept first postulated by Norwick.

Another important feature of Zn-Al alloys is that the damping behaviour is not dependent upon the applied stress (28) as shown in Figure 11. In most of other high damping alloys, high applied stress is required to produce maximum damping, thus applications where a high stress is not possible, are ruled out. Zn-Al alloys however, can be used simply as a damping pad or insert if required, that is a sheet of the alloy could be attached to a component where it would then damp out vibrations simply by being in contact with the component.

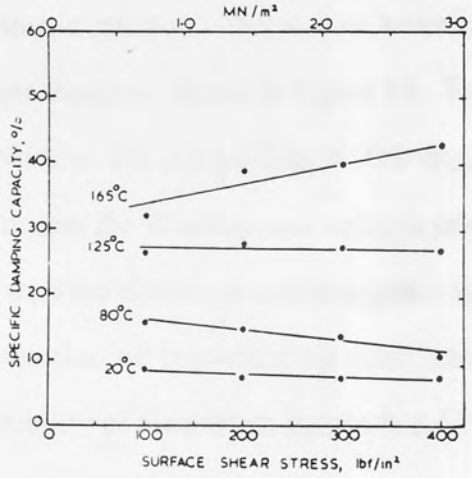

Figure 11. Variation of damping capacity with shear stress for zinc-aluminium alloy (28).

2.5 The Equilibrium Phase Diagrams

2.5.1 The Binary Zn-Al System

One of the best known and extensively studied phase diagram is that of zinc-aluminium system (37, 38). Aluminium is added to zinc to increase strength, reduce grain size and decrease the rate of attack of zinc on iron and steel parts of die casting machine or mould. Aluminium will also help to increase the fluidity of zinc and hence result in improved mechanical properties (39).

For many years there has been disagreement between investigators about the possibility of a peritectic reaction. The earliest investigation (40, 42) proposed the equilibrium phase diagram, shown in Figure 12. This shows a eutectic alloy of composition 95% Zn, 5% Al melting at 382 degrees C. At the eutectic temperature there occurs the simultaneous solidification of a solid solution of aluminium in zinc with the closed-packed hexagonal lattice of zinc, and a zinc-aluminium solid solution of face-centered cubic structure. At the eutectic temperature the solubility of aluminium in zinc is 1.14% falling to 0.05% at 20 degrees C.

The face centred cubic structure containing up to 83% zinc at the eutectic temperature is stable only at temperatures above 275 degrees C. On cooling below this temperature β phase containing 78% Zn undergoes an eutectoid transformation into zinc rich η phase with about 0.7% Al in solid solution and an aluminium rich solid solution of fcc α and containing 30% Zn.

Subsequent later studies by Owen and Pickup (42) and Elwood (44, 45) using high temperature X-ray camera methods, were unable to confirm the existence of

a peritectic reaction. Fink and Willey (46) denied the possibility of the peritectic reaction. Gayler and Sutherland (47) later also reached the same conclusion that at 443 degrees C the phenomenon of thermal arrest is due to a rapid change in composition of the α' solution along the solidus.

This lead researchers to believe that the diagram shown in Figure 12 was not satisfactory; Presnyakov et al (48) and Goldak and Parr (49) who disagreed with Gayler and Sutherland carried out further investigations. Presnyakov showed that there was indeed a peritectic reaction at about 443 degrees C and that a β phase, distinct from the α phase, existed and involved a discontinuity in the high temperature solubility of Zinc in Aluminium. He further discovered a second eutectoid decomposition of the α' into $(\alpha+\beta)$ at about 340 degrees C with the eutectoid point at about 70% Zn.

Figure 12 Zinc-Aluminium phase diagram compiled by Anderko (35)

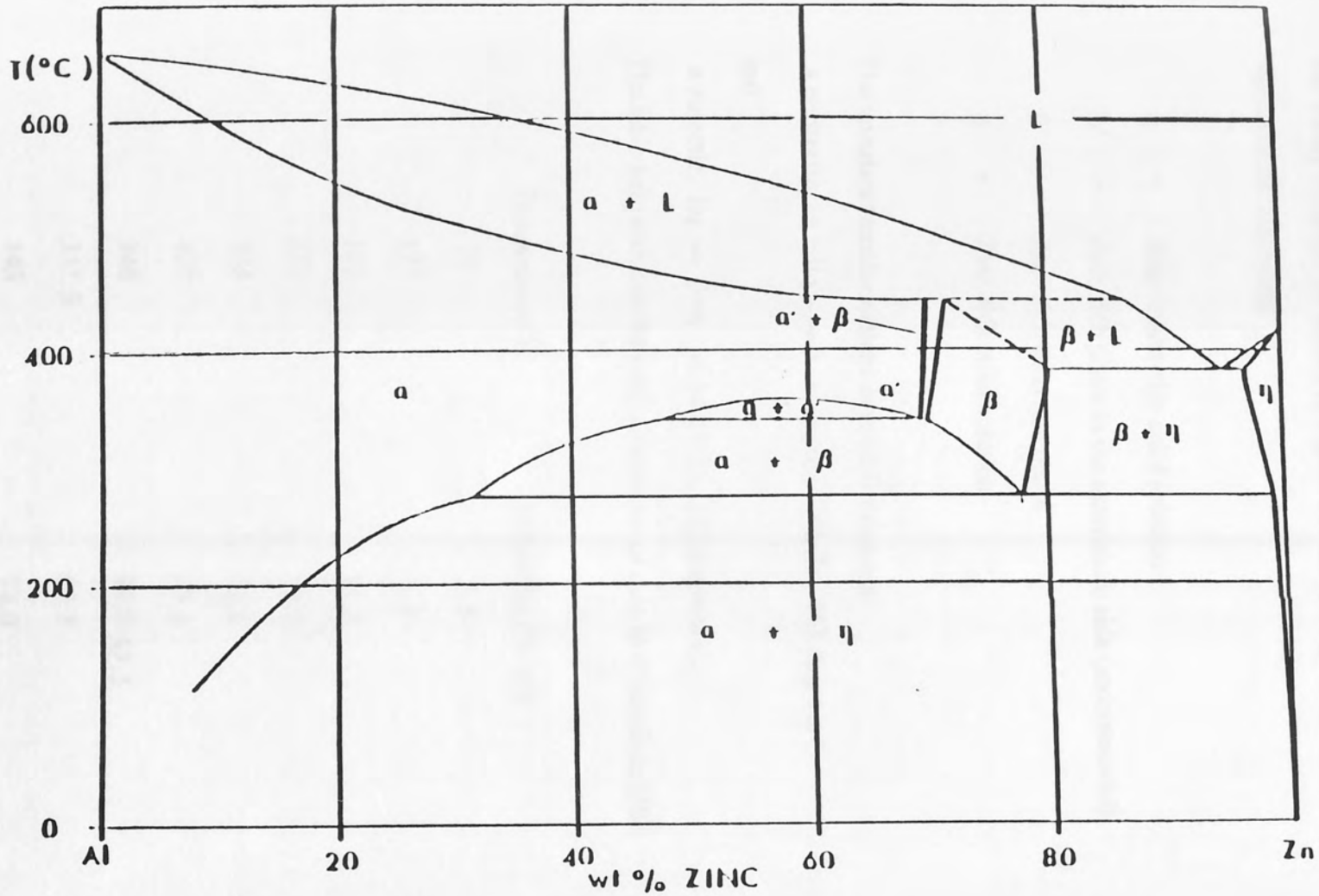

Figure 13 Accepted phase diagram of binary zinc-aluminium system.

Goldak and Parr later confirmed Presnyakov's investigation and the phase diagram which was produced is probably the most accurate representation of the binary diagram, as shown in Figure 13. In this figure the following symbols represent the following:

α = Aluminium-rich solid solution

α' = Zinc-rich phase in the aluminium side (monotectoid)

β = Zinc-rich eutectoid phase

η = Zinc-rich solid solution.

The invariant transformations in solidification are:

a peritectic, $\alpha + liq \longrightarrow \beta$ at approx 70% Zn, 443 degrees C

and

a eutectic, $liq \longrightarrow \beta+\eta$ at 94.9%Zn, 382 degrees C.

The table below shows the solid solubilities of zinc in aluminium (50).

Temperature ^{o}C	Solubility (% wt)
77	2.5
127	6.2
177	11.5
227	18.0
275	31.6
327	43.5
340	49.0-69.5
351.5	61.3
443	70.0

Table 1 . The solid solubility of zinc in Aluminium

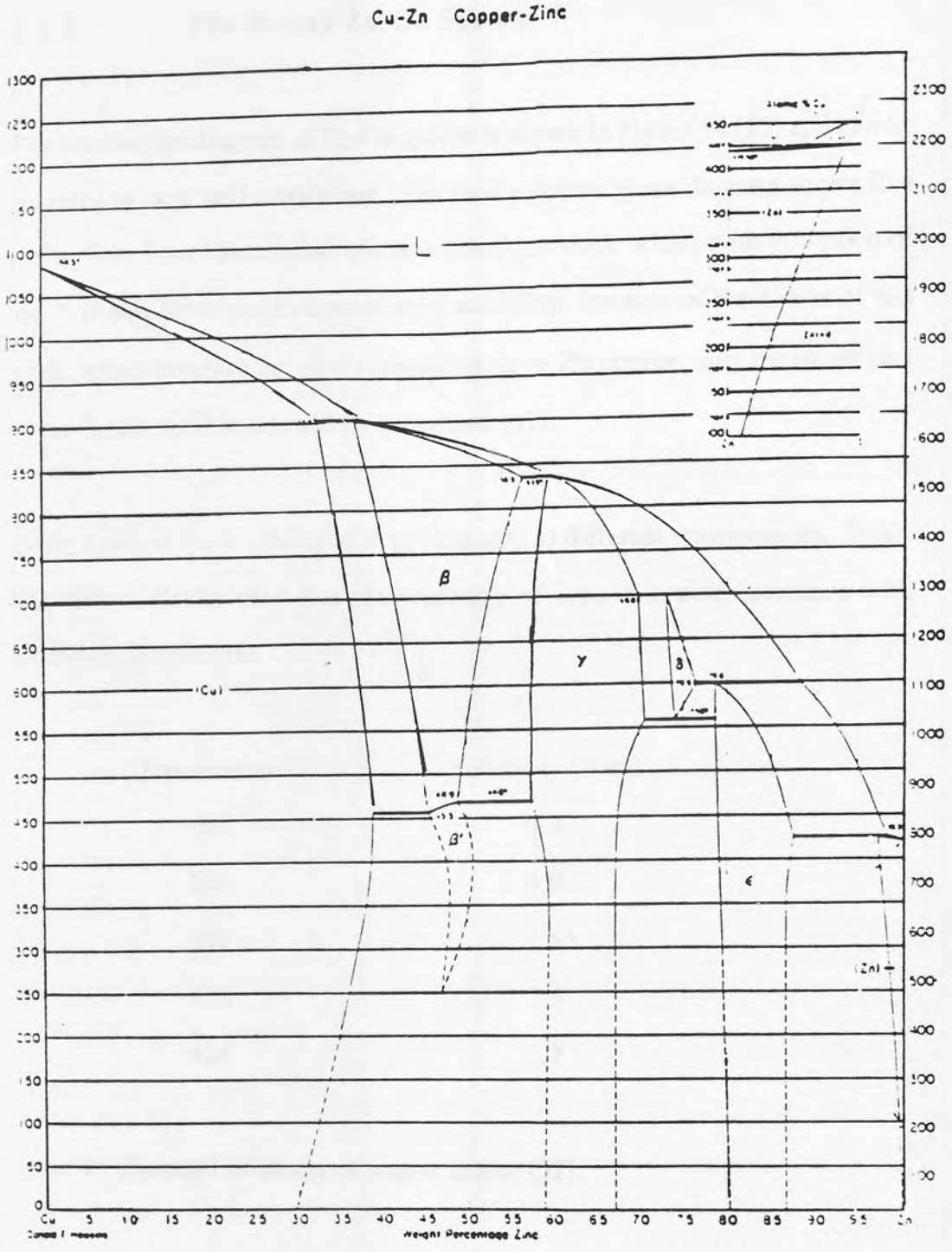

Figure 14 The equilibrium phase diagram of binary Zn-Cu system.

2.5.2 The Binary Zn-Cu System

The equilibrium diagram of Zn-Cu system is shown in Figure 14 (53) and can be regarded as very well established. The Zn-Cu system phase diagram shows five peritectics. Four intermediate phases exist, β,γ,σ and ε which with exception of the σ phase, have broad range of solid solubility. because of the nature of this work,.which involves the alloys containing up to 2% copper, only the lower part of the Zn-Cu equilibrium will be considered (51).

Table 2 shows the solubility of copper in zinc at different temperatures. From this table it can be seen that the solubility of copper in zinc increases with increasing temperature:

Temperature ^{o}C	Solubility (%wt)
100	0.3
200	0.9
300	1.65
400	2.5
424	2.7

Table 2. The solid solubility of copper in zinc (52).

Upon ageing the supersaturated solid solution of η phase decomposes into the $\eta+\varepsilon$ phases. Both the ε and the η phase have essentially the same crystal structure and the lattice spacing as follows:

ε: a = 2.735 Å c = 4.285 Å at 21 at % Cu (54)

η: a = 2.668 Å c = 4.870 Å at 1.5 at % Cu (55)

In the ε phase, the c/a ratio decreases from about 1.580 to 1.550 with increasing concentration of zinc in the region of 68-88% conversely, while on the other hand, the initial c/a ratio of η increases from about 1.780 near the (ε+η)/η boundary to 1.856 at pure zinc (56-57).

2.5.3 The Ternary Zn-Al-Si System

The Zn-Al-Si system is not a very well studied system but recently Zhu (58) has studied this system.

The isothermal sections of Zn-Al-Si system at 350 deg C, 300 deg C, 280 deg C, 272 deg C and 230 deg C are in shown in Figures 15,16,17, 18 and 19 respectively as compiled by Zhu (58). Diagrams were compiled using alloys ranging from 80% Al - 8.75% to 19% Al, 3.41% Si.

There are no intermetallic phases introduced by adding silicon to the Zn-Al system. The silicon exists as a terminal solid solution with limited solid solubility of aluminium and zinc, and this phase shown as σ in the isothermal sections is in equilibrium with the phases introduced by the Zn-Al boundary.

The isothermal sections are characterised by two enlarging three-phase fields of α+β+σ , and β+η+σ with decreasing temperature. When the temperature falls to 266 deg C, the phase transformation $\beta \longrightarrow \alpha+\eta$ occurs. Below this temperature β-phase disappears and the three phase α+η+σ is formed. Only the zinc-rich η phase is found to change very little in composition.

Comparison of the isothermal sections shows that the low solubility of Si in α, β, and η does not change drastically with temperature, so silicon precipitation is unlikely to contribute significantly to the hardness of the alloys on quench-ageing.

In the aluminium-rich solid solution α , the lattice parameter decreases from 4.044 Å to 4.021 Å (or 4.024 Å) with increasing zinc up to about 33% Zn.

Zinc rich phase has a closed packed hexagonal structure with

a_o = 2.675 Å $\quad$ c_o = 4.961 Å and $\quad$ c_o/a_o =1.855 Å

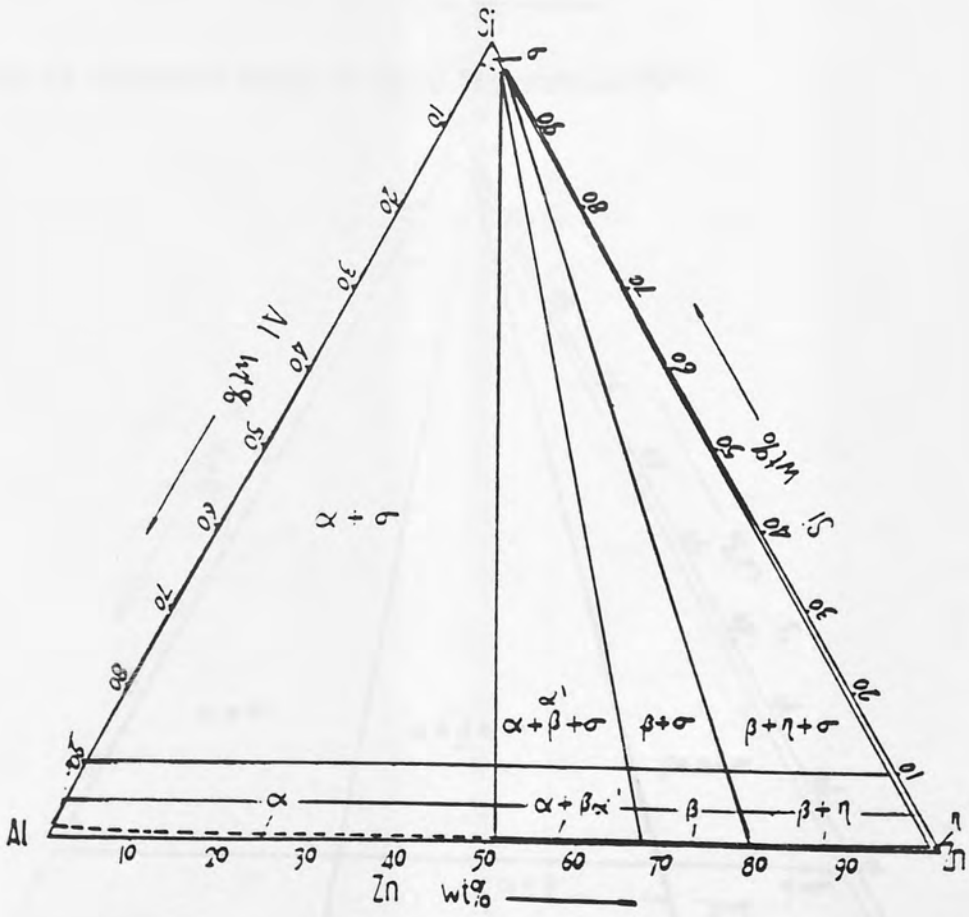

Figure 15 Isothermal section of Zn-Al-Si system at 350° C.

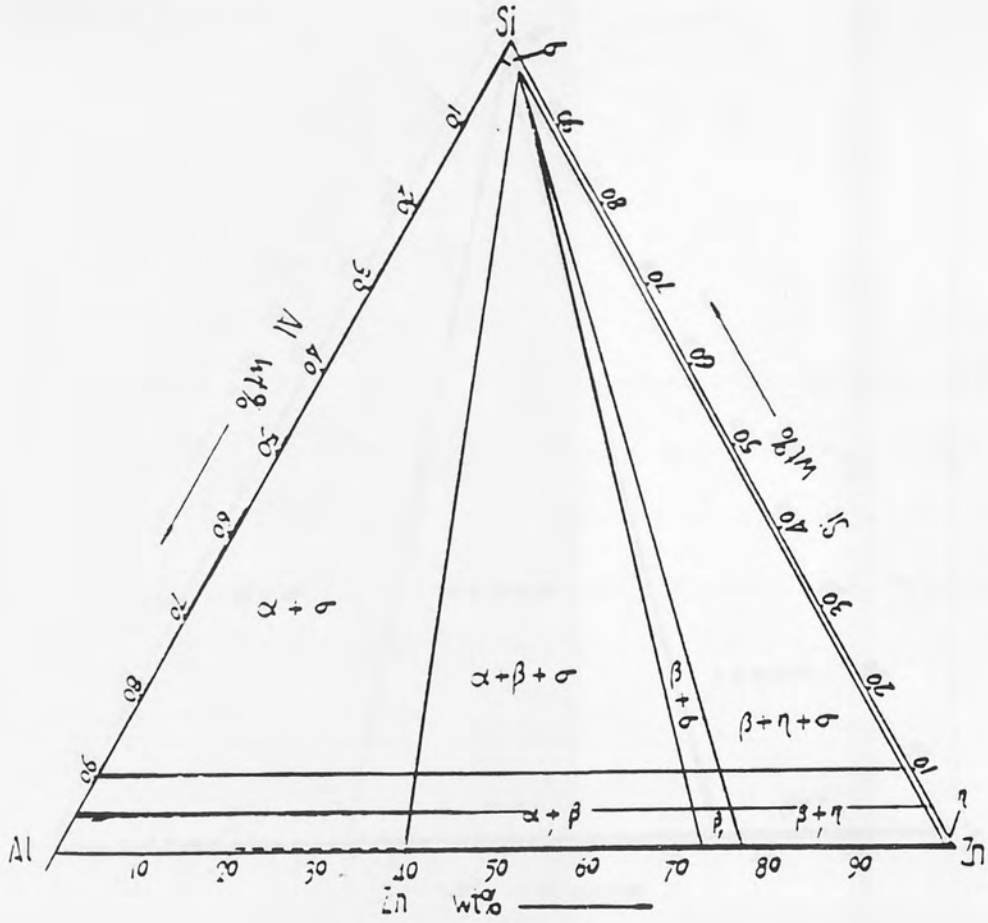

Figure 16 Isothermal section of Zn-Al-Si system at 300° C.

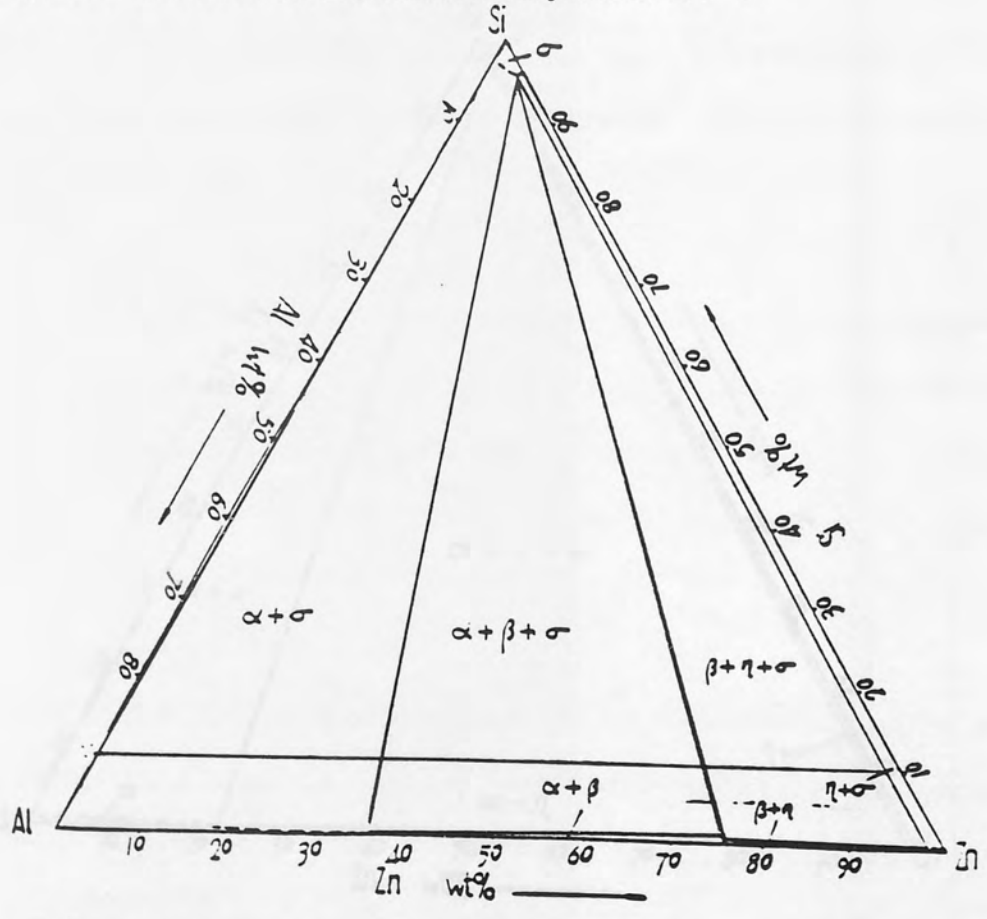

Figure 17 Isothermal section of Zn-Al-Si system at 280° C.

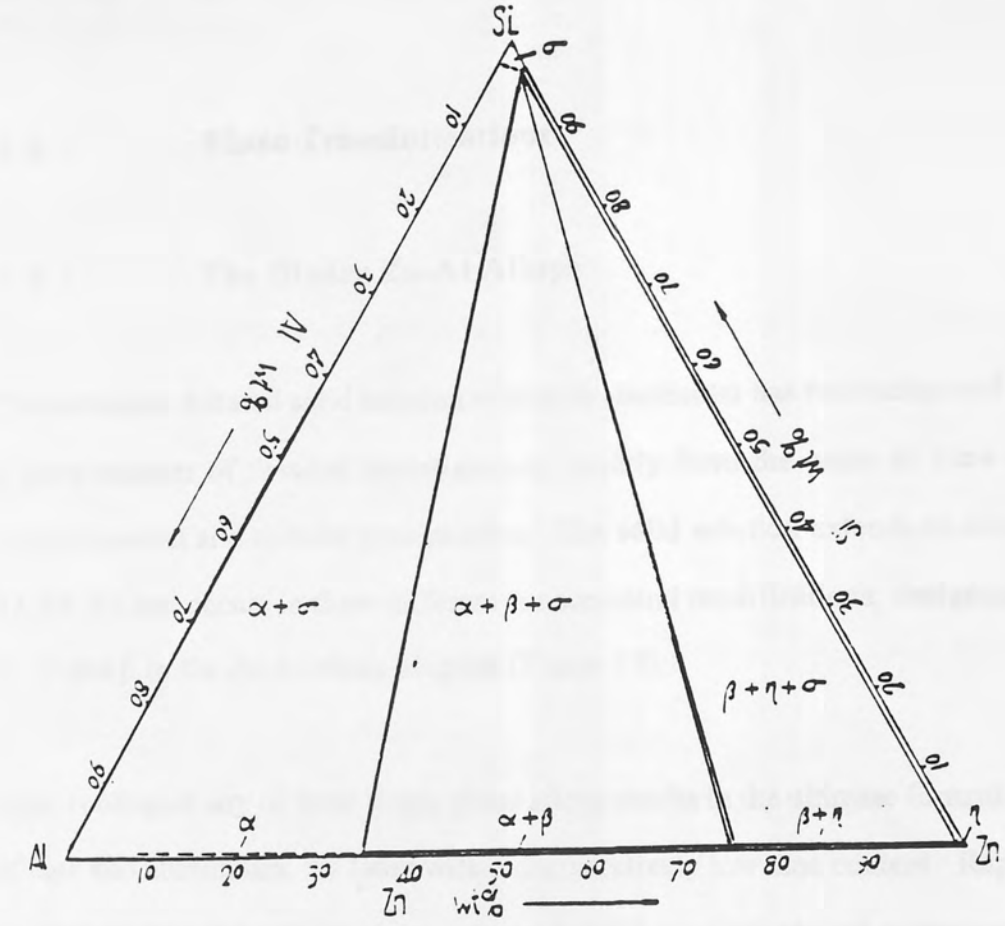

Figure 18 Isothermal section of Zn-Al-Si system at 272° C.

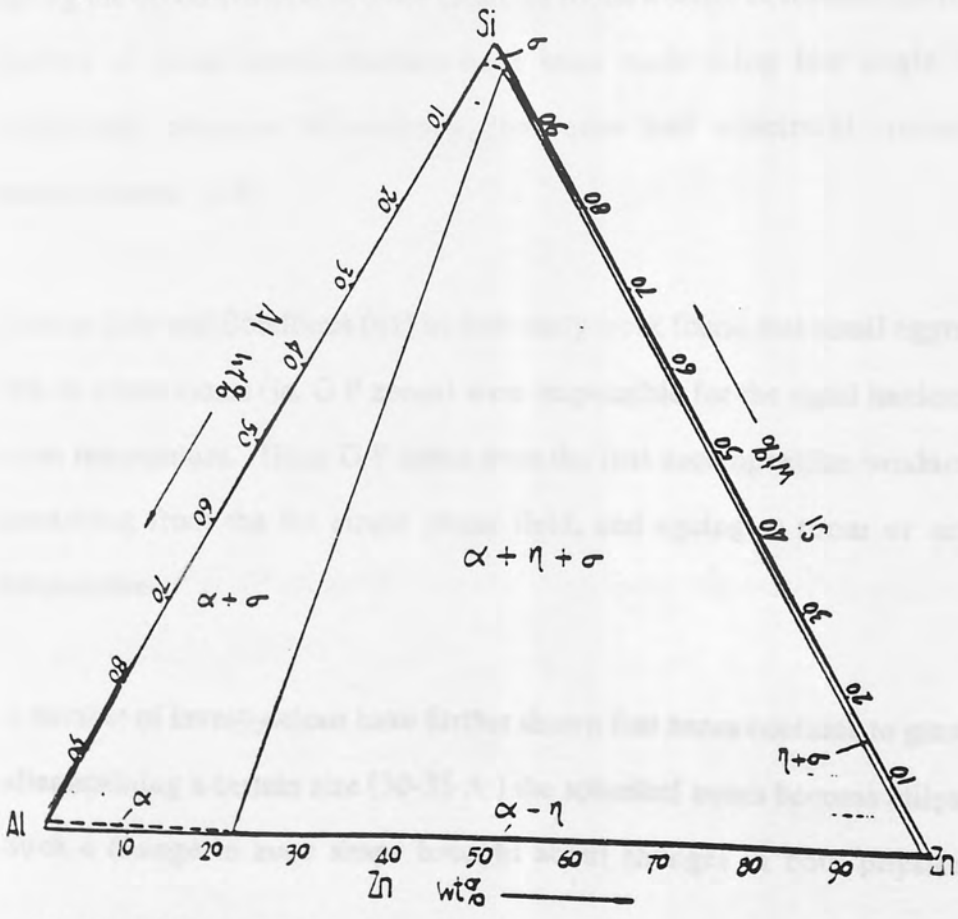

Figure 19 Isothermal section of Zn-Al-Si system at 230° C.

2.6 Phase Transformations

2.6.1 The Binary Zn-Al Alloys

The extensive α-based solid solution of zinc in aluminium has been subjected to a large number of detailed investigations, mainly from the point of view of transformation and cellular precipitation. The solid solution extends to about 82.5% Zn and occurs in three different iso-structural modifications, designated α, α' and β in the Zn-Al phase diagram (Figure 13).

Slow cooling of any of these single phase alloys results in the ultimate formation of zinc and aluminium, the latter with a comparatively low zinc content. Rapid cooling retains the zinc in super-saturated solid solution and on subsequent ageing the decomposition of these solutions forms a series of transitional phases. Studies of these transformations have been made using low angle X-ray scattering, electron microscopy, hardness and electrical resistivity measurements. (59).

Guinier (60) and Borellinus (61) in their early work found that small aggregates rich in solute atoms (ie. G P zones) were responsible for the rapid hardening at room temperature. These G P zones were the first decomposition product after quenching from the fcc single phase field, and ageing at room or subzero temperature.

A number of investigations have further shown that zones continue to grow, and after attaining a certain size (30-35 A) the spherical zones become ellipsoidal. Such a change in zone shape brought about changes in both physical and

mechanical properties of the alloy that occur during the early stages of ageing in this system. (62-67).

These ellipsoidal zones further transform into a rhombohedral transition phase, R, which is precipitated in the form of plates, partially coherent with the matrix but with a zinc content less than that of the zones (65-74).

Recently, there has been direct evidence (71) of the transition of G P zones to another phase, α''_m which is formed at high temperature either on direct quenching or by zone reversion.

On prolonged ageing at a certain composition the α''_m phase grows to such an extent that coherency is completely lost in the [111] habit planes. Since the elastic strain due to coherency is responsible for the rhombohedral distortion, the structure becomes fcc. This new cubic phase is called α'_m phase (75). The rhombohedral α''_m phase differs only slightly in lattice parameters (a = 3.992 Å α' = 91.36) from the cubic α'_m phase (a = 3.995 Å) (76).

Finally, stable Zn-rich precipitates are formed with the lattice parameters of

a = 2.859 Å , c = 4.947 Å , (77)

The orientation relationship between zinc precipitates and the aluminium matrix was determined (78-80) as

(111) Al // (0001) Zn, [110] Al // $[10\bar{1}0]$ Zn

The whole ageing sequence in the Al-Zn system up to a certain composition would seem to be as follows:

Supersaturated solid solution α'_s ⟶ spherical

G P zones ⟶ Ellipsoidal G P zones ⟶

Rhombohedral transition α''_m phase ⟶

fcc transition phase α'_m ⟶ zinc-rich stable η phase.

More concentrated Zn-Al alloys have been less thorough. The decomposition products of the solid solution in high Zn alloys entirely depends on the cooling rate and the heat treatment temperature, and may result from one of two (or both) distinct decomposition mechanisms given below:

1) A conventional cellular (or discontinuous) reaction, mainly resulting in grain boundary nucleated lamellar segregates of $\alpha+\beta$.

2) Spinodal decomposition of the Al-rich matrix.

The conventional cellular decomposition occurs more frequently than the spinodal decomposition in the Zn-Al system. A detailed study of this reaction was made by Ramaswamy et al (81) on alloy Al-50% Zn. A more recent investigation was made by Vijayalakshmi et al (82, 83), where investigations involved two types of alloys one of 60% Zn and the other of 75% Zn. After solution treatment and ageing the alloys, it was observed in both areas that a cellular reaction started at the grain boundaries. The evidence for the nucleation stage at grain boundaries was explained by the aid of mechanisms proposed by Fournelle and Clark (84). According to this mechanism, the migration of a curved grain boundary of α' matrix leads to a net reduction in the grain

boundary area. The high diffusitives of the solute atoms across a mobile boundary facilitates the nucleation of stable η precipitates, resulting in the pinning of the boundary. The migrated boundary leaves a narrow region depleted of solute atoms by diffusion to the newly formed allotromorphs of η , thus a narrow precipitates-free zone is formed. However, lamellar structures were observed to have developed from these grain boundary allotrimorphs and tended to grow into the parent grain at later stages of the decomposition. Two mechanisms were involved in achieving and establishing their unique lamellar spacing.

1) By branching of existing lamellae (81-83), and less frequently.

2) By the nucleation of fresh lamellae at an advancing interface (81-83).

Boswell and Chadwick (85) and Cheetham and Ridley (86) have concluded that the rate of increase of the interlamellar spacing is a function of the applied undercooling and thus of ageing temperature. They observed a decrease in the interlamellar spacing when decreasing the temperature. A relationship between the two was proposed by Cheetham and Ridley (86).

$$S \alpha \Delta T^{-0.9}$$

It was reported (85) that during the growth of the cells, the lamellae maintain the following orientation relation across their interface:

$$(111)\ \alpha \,//\, (0001)\ \eta \text{ with } \langle 111 \rangle\ \alpha \,//\, \langle \bar{1}2\bar{1}0 \rangle \eta$$

Other workers (86-88) carried out their studies on the decomposition of the eutectoid alloy during quench-ageing, isothermal transformation and slow cooling to the transformation temperature. These workers reported that depending on the transformation temperature, more than one type of decomposition product was found on ageing those alloys with a composition corresponding to the eutectoid β phase (86-89, 90). Decomposition of the eutectoid alloy during slow cooling, or isothermally transforming at high temperature produced a lamellar structure. However, decomposition at room temperature after a rapid quench produced a fine (1μm) mixture of equiaxed zinc rich α''_m and aluminium rich grains. A possible interpretation of these changes may be that a spinoidal decomposition took place at about room temperature (86, 88). Toldin et al (91) studied in detail the process of decomposition of supersaturated solid solution in Al-Zn alloys with 40, 50 and 60% Zn (AlZnII) and in an alloy containing 73% Zn(AlZn III). They generalised the possible sequence of transformations that could occur depending on composition, cooling rate and heat treatment temperature, as shown in Figure 20. As can be seen from the figure, there are 11 sequences of phase transformation that could occur through metastable phases (R, α'_m) or from GP zones. α'_m is formed in AlZn II alloys by both isothermal transformation and quench-ageing process. A number of sequences (6-9) which begin with the formation of GP zones is formed on quench-ageing. R-phase is formed preferably by the mechanism of spinodal decomposition and metastable α'_m phase by nucleation.

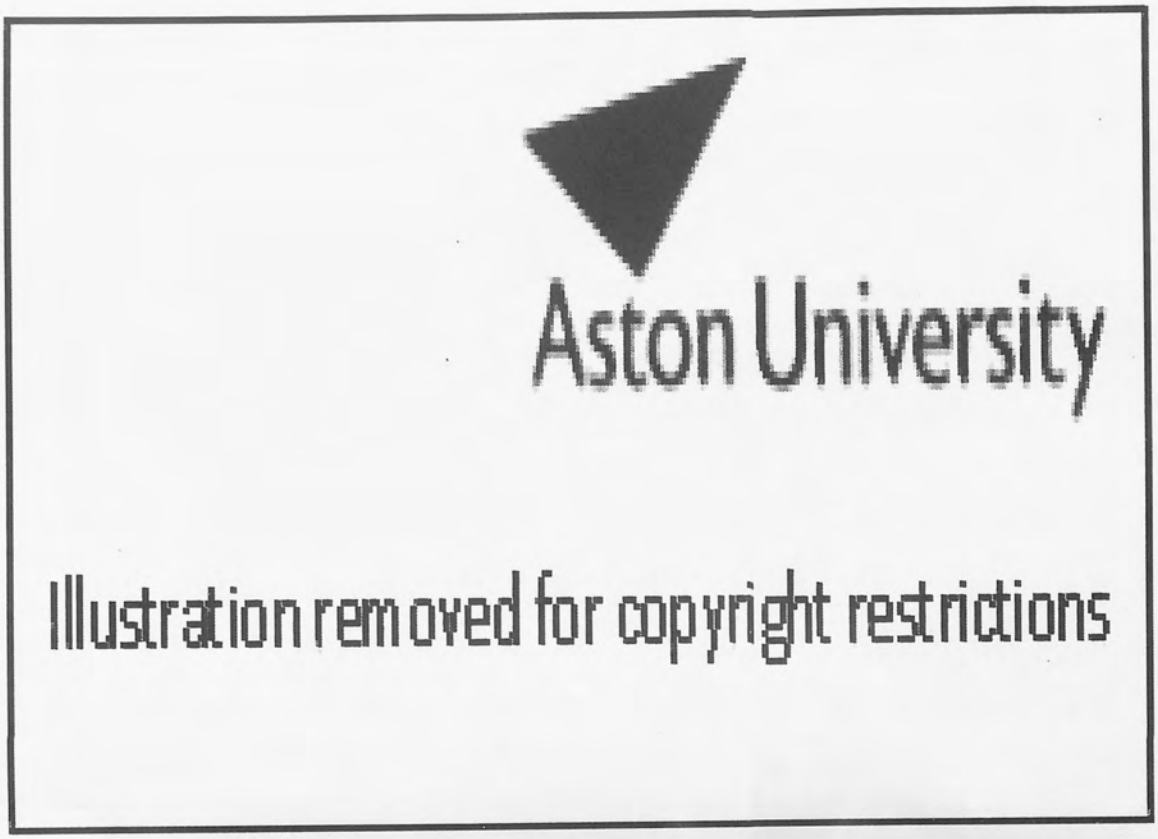

Figure 20 A scheme of transformation in Zn Al alloys according to Toldin et al (91)

Metastable state of the phases which might exist in the binary system was investigated further by the same authors in their extended works (92, 93) and Krupkowski et al (94). They indicated that two types of metastable state might exist in the low temperature ($\alpha+\eta$) region, one being defined by solubility limits of the ($\alpha+\beta$) region, which continue to the low temperature ($\alpha+\eta$) region, and the other bounded in the same way by the boundaries of ($\alpha+\alpha'$) region which continue to the low temperature ($\alpha+\eta$) region shown in Figure 21.

A recent study at Aston university (120) showed that the transformation of metastable phases in as-cast or heat-treated Zn-Al based alloys gives rise to irreversible dimensional change on aging. Short-term effects are associated with the breakdown of supersaturated, aluminium-rich solid solution, and usually pose no problems. The long-term effects are caused by the slow approach to equilibrium of copper-rich phases, and this may cause significant change in the dimensions of cast components.

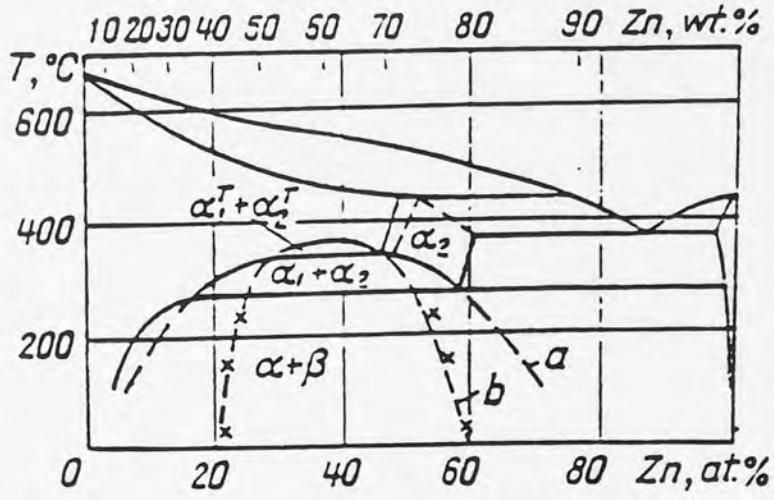

Figure 21. Phase diagram of Zn-Al system with metastability boundaries (a, b).

Another recent work here at Aston university on the solidification structure of pressure- die-cast commercial alloy M3 (121) has shown that the rapidly cooled alloy commenced solidification by the formation of small rounded primary zinc (η) particles followed by pesudo-primary β particles and then a fine eutectic of $\beta+\eta$. The high temperature β phase subsequently decomposed into α-aluminium and η, the phases stable at ambient temperature, but an intermediate transitional phase was found in alloys examined shortly after casting. Chemical analysis by energy -dispersive spectroscopy showed that this phase contained zinc with 11.8 wt. % Al, suggesting that it was a transitional phase since none of the stable phases in the Al-Zn system has that composition. This transitional phase had almost entirely disappeared after aging for a period of 5 years.

2.6.2 Ternary Zn-Al-Si System

2.6.2.1 Alloys of Monotectoid and Eutectoid Compositions

The Zn-Al-Si system has only recently been investigated by Zhu (92). In his work he shows that the phase transformation of ageing in alloy Al 35%, Zn 60%, Si 5% starts with a cellular reaction:

$$\alpha'_s\ (+\sigma) \longrightarrow \alpha'_T + \eta\ (+\sigma)$$

Four phases were present at the as-quenched stage. The supersaturated α'_s phase starts to decompose into the metastable phase α'_T and zinc-rich η phase. After the cellular reactions are completed, the alloy enters into the G.P. zone stage and then decomposes into the first transitional phase α''_m in equilibrium with the matrix phase α''. On prolonged ageing, the α'' phase and the first transitional phase α''_m is transformed to α' and the second transitional phase α'_m. Finally, α_f and η are formed by continuous precipitation from α' and α'_m phases. Because the transformation occurs rapidly, the contribution of the cellular reaction and the formation of G.P. zones to the increases in hardness combined to give rise to a hardness peak at an early stage of ageing.

The sequence of the phase transformation is as follows:

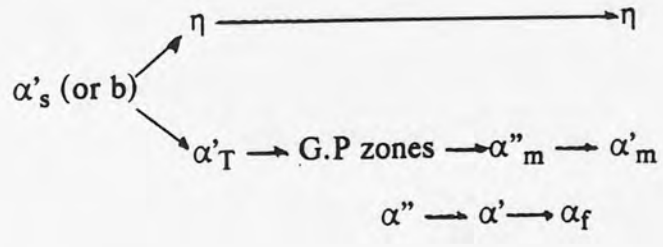

2.6.2.2. Al-rich Alloys

The phase transformation of these alloys consists of four typical steps:

1) Formation of GP zones

2) The first transitional phase α''_m in equilibrium with the matrix phase α''.

3) The second transitional phase α'_m in equilibrium with the matrix phase α'

4) Final stable α_f and η phase.

The sequence is described as follows:

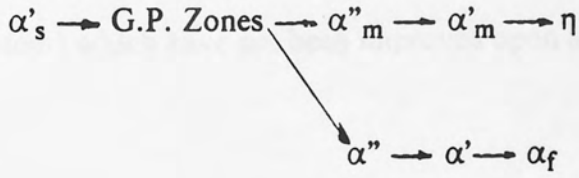

It is believed that the Si-rich σ phase has only a minor influence in phase transformations (92).

2.7 Pressure Die-casting Zn-Al Alloys

2.7.1 Commercial Pressure Die-casting Zn-Al Based Alloys

For over 100 years permanent iron moulds have been used for the repetitive production of numbers of metal castings, and with increasing mechanisation die castings have become an important production operation. Since the beginning of the century, attempts were made to die cast zinc alloys, but in many cases rapid deterioration set in after a few months of service, and results were disastrous. The problem was studied by the New Jersey zinc company and in 1923 it was discovered that the commercial alloys had failed owing to intercrystalline corrosion, caused by impurities such as lead or tin which have almost negligible solubility in solid zinc (93). No deterioration occurred if the alloys were compounded of high purity zinc (99.99 + percent) so that the offending impurities could be held to very low levels. The investigators soon put forward a series of alloys to which they gave the name Zamak (known as Mazak in the United Kingdom) which have not been improved upon and which are still used today (94).

These alloys, compared to die casting alloys such as aluminium and magnesium alloy, have many advantages. Zinc alloys are more easily cast, are stronger and more ductile, require less finishing, can be held to lower tolerances and can be cast in thinner sections. The die life for zinc die castings far exceeds that for other die casting materials because of low casting temperatures. The production rate is also much higher (95). They are used in numerous applications ranging from the simplest drawer handle to the most complex precision automotive part (96). Table 3 shows the nominal composition of these alloys, and compares the British Standard (BS1004) to that of American Society for Material Testing(B-86).

Zinc alloys with a higher aluminium content and often some copper eg. ALZEN 305, containing 30% aluminium and 5% copper developed in Austria during the second world war as a substitute for phosper-bronze in bearings achieved some commercial success, but engineers showed little real interest in them. During the 1960's, the International Lead Zinc Research Organisation developed an alloy first called ILZRO 12, containing 12% aluminium and 1% copper with 0.025% magnesium. It was recommended for making sand or plaster-cast prototypes for zinc die castings as its tensile strength was similar though its ductility was much less. Eventually, it was realised that the alloy, after its contents had been reduced to 10.5%, was very good for sand or gravity castings. In competition with aluminium alloys, copper alloys and even cast iron, for numerous applications, compared with other alloys, it is cheaper to melt and provides better working conditions at the lower casting temperatures. The alloy is now known internationally as ZA12 despite its reduced aluminium content. Its properties are shown in Table 4 and 5. More recently, two further alloys have become commercially available, ZA27 and ZA8. The properties are also shown in Tables 4 and 5 (94) and the composition of all three alloys are given in Table 6 (94).

		Alloy Zamak 3 (USA) Mazak 3 (UK)		Alloy Zamak 5 (USA) Mazak 5 (UK)	
		UK Specification BS 1004 A	USA Specification B-86	UK Specification BS 1004 B	USA Specification B-86
Aluminium	min.	3.8	3.5	3.8	3.5
	max.	4.3	4.3	4.3	4.3
Copper	min.	–	–	0.75	0.75
	max.	0.03	0.25	1.25	1.25
Magnesium	min.	0.03	0.02	0.03	0.03
	max.	0.06	0.05	0.06	0.08
Iron	max.	0.10	0.10	0.10	0.10
Nickel	max.	0.02	0.02	0.02	0.02
Manganese	max.	0.01	0.01	0.01	0.01
Lead	max.	0.005	0.005	0.005	0.005
Cadmium	max.	0.005	0.004	0.005	0.004
Tin	max.	0.002	0.003	0.002	0.003
Zinc		remainder	remainder	remainder	remainder

Table 3. Zinc alloy die casting composition

	Alloy 8 gravity cast	Alloy 12 sand cast	Alloy 27 sand cast
Density at 20°C (g/cm^3)	6.30	6.03	5.00
Solidification shrinkage (%)	1.1	1.3	1.3
Solidification temperature range (°C)	404–375	432–377	484–375
Thermal expansion (μm/m °C) at 20°C to 100°C	23.2	24.1	26.0
Thermal conductivity (Wm^{-1} K^{-1}) at 24°C	115	116	125.5
Electrical conductivity (% I.C.A.S.)	27.7	28.3	29.7
Specific heat capacity (J/kg °C) at 24°C to 92°C	435	450	525
Electrical resistivity ($\mu\Omega$ cm) at 20°C	6.2	6.1	5.8
Pattern maker's shrinkage (mm/m)	10.4	13	13

Table 4 Physical properties of zinc-base casting alloys.

	Alloy 8	Alloy 12			Alloy 27
	cast gravity	sand cast	permanent mould cast	sand cast	[a]sand cast and homogenised
Ultimate tensile strength (MNm^{-2})	221–255	275–317	310–345	400–440	310–325
Yield strength (MNm^{-2}) (0.2% offset)	208	207	214	365	255
Elongation on 51 mm (per cent)	1–2	1–3	1–2	3–6	8–11
[a]Hardness (B.H.N.)	85–90	92–96	88–90	110–120	90–100
Shear strength (MNm^{-2})	241	248–262	N.A.	283–297	221–228
[a]Impact strength (J) (10 mm X 10 mm bar unnotched) at 20°C	N.A.	27 ± 3	N.A.	48 ± 7	58 ± 12
Fatigue strength (MNm^{-2}) (5 X 10^8 cycles)	51.8	103.4	N.A.	172.5	103.5
Creep strength (MNm^{-2}) stress to produce creep rate of 0.01%/1000 h at 20°C	59 approx.	59 approx.	59 approx.	69 approx.	86 approx.
Creep rate at 138 (MNm^{-2}) stress (% 1000 h) at 20°C	0.2	0.2	0.2	0.1	0.07

[a] Homogenised for 3 h at 320°C followed by furnace cooling. N.A. Not available.

Table 5 Mechanical properties of zinc-base casting alloys.

		Alloy 8 (%)	Alloy 12 (%)	Alloy 27 (%)
Aluminium	not less than	8.0	10.5	25.0
	not more than	8.8	11.5	28.0
Copper	not less than	0.8	0.5	2.0
	not more than	1.3	1.25	2.5
Magnesium	not less than	0.015	0.015	0.010
	not more than	0.030	0.030	0.020
Impurities				
Iron	not more than	0.10	0.075	0.10
Lead	not more than	0.004	0.004	0.004
Cadmium	not more than	0.003	0.003	0.003
Tin	not more than	0.002	0.002	0.002
Zinc		remainder	remainder	remainder

Table 6 Chemical composition of zinc-base casting alloys.

They can all be die-cast in cold chamber machines; ZA8 alloy because of its lower melting point and low Al content, could even be used in conventional hot chamber machines (97-99). Within the family ZA27 has the highest strength and hardness followed by ZA12 and ZA8. The tensile strength of ZA27 is not significantly affected by casting techniques, whereas the tensile properties and hardness of ZA8 and ZA12 are significantly higher in die-cast conditions. It is believed that the significant improvement brought forward as a result of die-casting these alloys are due to microstructural refinement resulting from the fast-cooling rate, a characteristic of the die-casting process (97).

Recent work carried out by Murphy, Hill and Durman (100) on the effect of elevated temperature in the range of 20 degrees C to 260 degrees C on the tensile properties of the die-cast alloy Mazak 3, ZA8 and ZA27 are represented in Figures 21, 22 and 23.

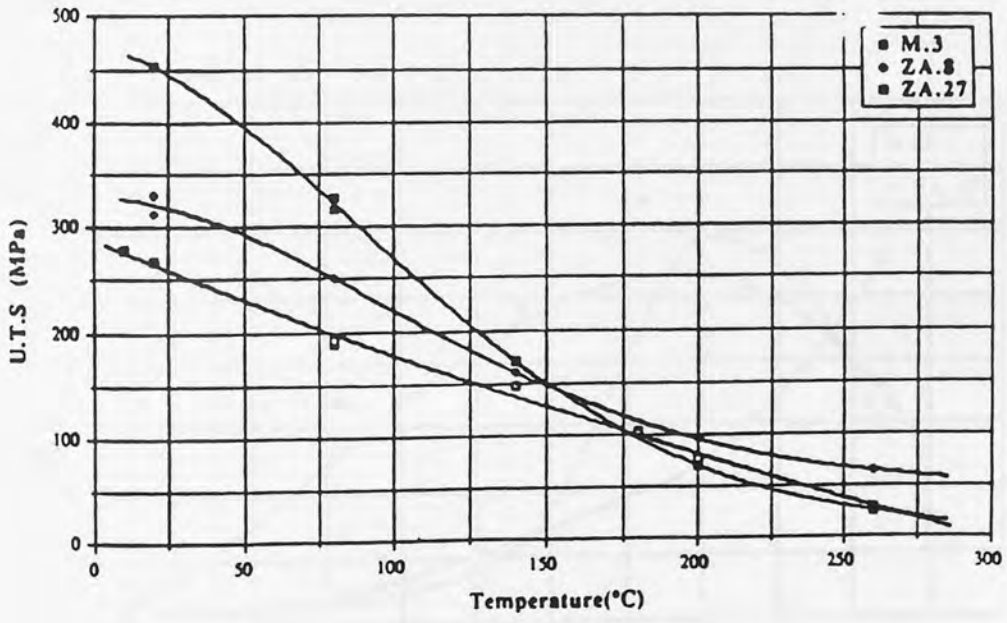

Figure 22 Variation of U.T.S. of alloys M3, ZA8 and ZA27 with temperature.

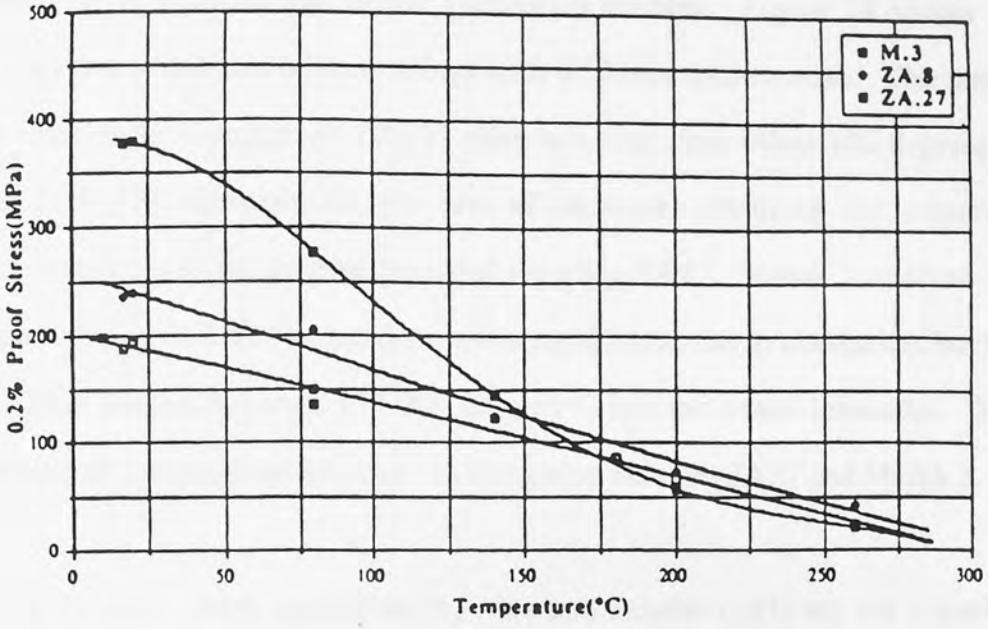

Figure 23 Variation of 0.2% proof stress of alloys M3, ZA8 and ZA27 with temperature.

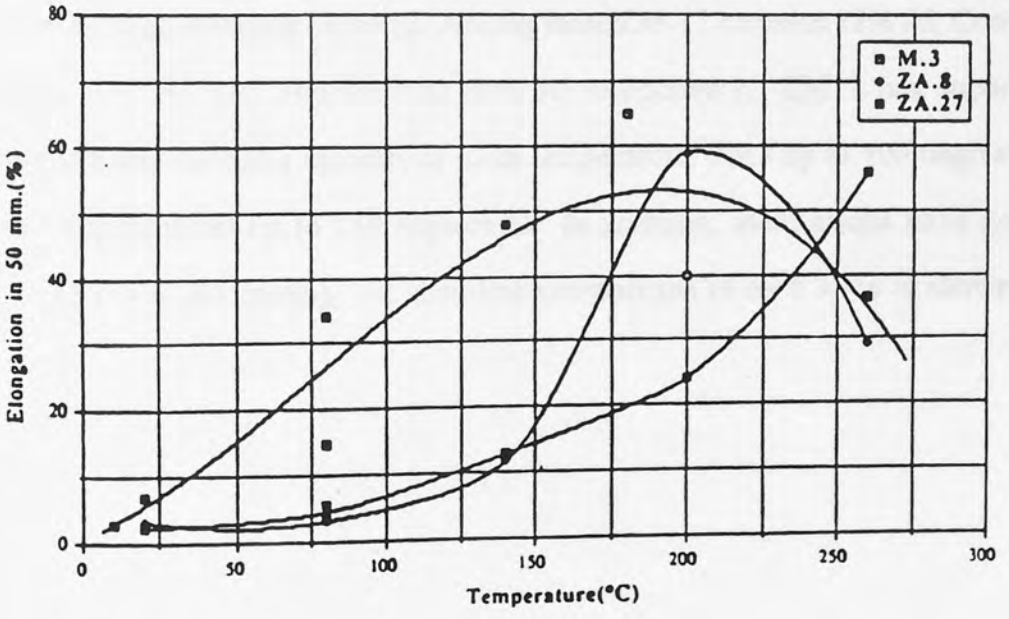

Figure 24 Variation of the % elongation of alloys M3, ZA8 and ZA27 with temperature.

These figures show that the ultimate tensile strength and proof stress of these alloys decreased with an increase in temperature. The rate of decrease was found to be proportional to the aluminium content. Figure 24 shows the elongation properties of these alloys with different temperatures. The rate of increase in the elongation of ZA27 alloy was very slow below 100 degrees C, but at higher temperature, the rate of increase exhibited the expected characteristics of the superplasticity of the alloy ZA27. Mazak 3 behaved in a different way to ZA27 in that there was a rapid initial rise in elongation, but this increase peaked between 150-200 degrees C and decreased thereafter. ZA8 showed an intermediate behaviour in elongation between ZA27 and Mazak 3.

Very recently, work carried out by Mae and Sakono (101) set out a goal of developing a new family of alloys with high damping capacity. These alloys were developed not only to have high damping capacity but also to satisfy the needs of structural materials such as lightness, strength and low cost. This lead to the development of new family of Zn-Al alloys for die-casting (Trade Mark Cosmal-Z) by alloying it with Si, Cu and Mn to strengthen without lowering the inherent high damping capacity. Among these ZM-11 contains 22% Al, Cosmal ZM3 40% Al, and Supercosmal 60% Al respectively. ZM11 has superior strength and damping capacity at room temperature, ZM3 up to 100 degrees C and Supercosmal up to 150 degrees C. In addition, these alloys have good castability in die casting, the chemical composition of each alloy is shown in Table 7.

2.8 Effect of Alloying Elements on General Properties

2.8.1 Copper

Copper tends to increase tensile strength and hardness (102), but reduces impact strength and causes some dimensional instability on ageing. In consequence, the copper-free Mazak 3 is used for most applications and Mazak 5 is reserved for those applications where the highest tensile strength, hardness and castability are required.

2.8.2 Magnesium

Magnesium plays an important part in reducing the possibility of intercrystalline corrosion and increasing hardness and tensile strength. If present above 0.06%, impact strength and ductility are adversely affected.

2.8.3 Silicon

Silicon is virtually insoluble in pure zinc as well as in Zn-Al alloys (103, 104). The presence of silicon as low as 0.02% increases the ultimate tensile strength, but drastically reduces the elongation and impact properties (105). Silicon is also used for lowering the melting point (101).

2.8.4 Manganese

The solubility of manganese in zinc is 0.047 wt% at 400° C (106), this solubility decreases when decreasing the temperature, and at room temperature the solubility is very small, and gets smaller when zinc is alloyed with aluminium.

2.8.5 Lead and Tin

Lead and tin above 0.07% and 0.05% are highly dangerous, since if they are exceeded, corrosion in humid atmospheres can spread rapidly along the grain boundaries, where the impurities are concentrated, and the strength of the casting is seriously reduced.

2.8.6 Cadmium

Cadmium has a harmful effect on both mechanical properties and ease of casting and should not exceed 0.005%. It is not clear whether or not cadmium promotes intercrystalline corrosion.

2.8.7 Iron

Iron has little effect on the properties of the die-cast alloy. Approximately 0.02% is held in solid solution, but above this concentration, iron tends to form a hard compound with aluminium present, and can cause machining problems.

CHAPTER 3

3.0 EXPERIMENTAL PROCEDURE

3.1 ALLOYS

3.1.1. Cosmal Alloys

This family of alloys was chosen because of their reported high damping properties. The family of alloys tested were produced by Mitsubishi Metal Corporation (Japan) and have the following composition:

	Al	Si	Cu	Mn	Mg	Fe	Pb	Sn	Cd	Zn
ZM11	22	1.5	0.5	0.3	0.005	0.1	0.003	0.001	0.001	Bal.
Cosmal	40	3.0	1.0	0.3	0.005	0.1	0.003	0.001	0.001	Bal
S.Cosmal	60	6.0	1.0	0.3	0.005	0.2	0.003	0.001	0.001	Bal

Table 7. Chemical composition of Cosmal Z-alloys.

The above family of alloys are known on the Cosmal family of zinc-aluminium based alloys. The purposes of the alloying elements are as follows:

Si - Lower the melting point, strengthening the alloy.

Cu - Prevent intergranular corrosion.

Mn - Improve creep strength.

Mg - NOT used due to the deterious effect on the internal friction and

thermal stability of the alloy.

Pb, Sn, Cd - Kept to low levels due to causing the intergranual corrosion.

3.1.2 Commercial Pressure die-cast alloys

These were commercial alloys Mazak 3, ZA8 and ZA27. These alloys were chosen because they were readily available and also ZA27 is known as an alloy with good damping properties. The table below shows the chemical compositions of the alloys.

Alloy	Zn (%)	Al (%)	Cu (%)	Mg (%)	Ti (%)	Cr (%)
Mazak.3	balance	3.9-4.3	–	0.04-0.06	–	–
ZA.8	"	8.0-8.8	0.8-1.3	0.015-0.03	–	–
ZA.12	"	10.5-11.5	0.5-1.25	0.015-0.03	–	–
ZA.27	"	25.0-28.0	2.0-2.5	0.01-0.02	–	–

Table 8. Chemical composition of commercial alloys.

Two other experimental alloys were also cast at Aston Foundry. The compositions of these alloys were based on the standard ZA27 alloy and will from here on be referred to as alloys H1 and H2, with the following composition:

(H1)	0.3%	Mn	(H2)	0.3%	Mn
	1%	Cu		1%	Cu
	27%	Al		2.5%	Si
	rem	Zn		27%	Al
				rem	Zn

Table 9. Chemical composition of alloys H1 and H2.

3.1.2.1 Preparation of Ingots

The commercial alloys were provided by Mazak Ltd. in the form of standard ingots. The Cosmal alloys were produced by preparing ingots weighing 20 kg, from high purity (99.99%) zinc and (99.985%) aluminium, with the required additions.

In order to prepare each ingot the required amounts of zinc, aluminium and other alloying elements were melted in a silicon-carbide crucible, in the induction furnace at a temperature between 550-750 degrees C depending on the alloy compositions. The melt was then stirred vigorously to ensure even dispersion of alloying elements. The melts were then cast into a coated steel mould to form the required ingots.

3.1.2.2 Die Casting of the Alloys

All die castings were made at the Aston University Foundry using an industrial pneumatic cold-chamber pressure die-casting machine as shown in Figure 25. This

is an E.M.B 10B die-casting machine with a maximum locking force of 76 tons, and is operated in two phases:

Phase 1 : A fixed low-speed movement of injection plunger.

Phase 2 : An adjustable high speed acceleration of the injection plunger.

The purpose of phase one was to start pushing the melted metal into the sleeve and to draw as much as possible from the sleeve and die cavity. At the point when molten metal reaches die cavity a sudden acceleration (phase 2) takes place to force the metal into the die cavity at the required speed.

Some advanced industrial die casting machines work with an additional third phase, with the purpose of applying a high-pressure during final stages of solidification in order to minimise the occurrence of shrinkage and porosity defects. (1-2).

Figure 25 shows the cold-chamber pressure die casting machine used to carry out the above mentioned work

Figure 25. E.M.B 10B Cold-chamber die casting machine.

The die used in the die casting machine was designed at Aston by M Durman and K Sawalha. The die is designed to produce two identical impressions of thin section rectangular plates. The above mentioned designers carefully considered the following factors:

1. The feed systems.
2. Cavity fill time.
3. Gate velocity and fill pattern.

In order to make the job of designing a die easier a computer program developed by Mazak Ltd was used. The program basically works by knowing the characteristics of any die casting machine (the maximum available pressure of the machine, the

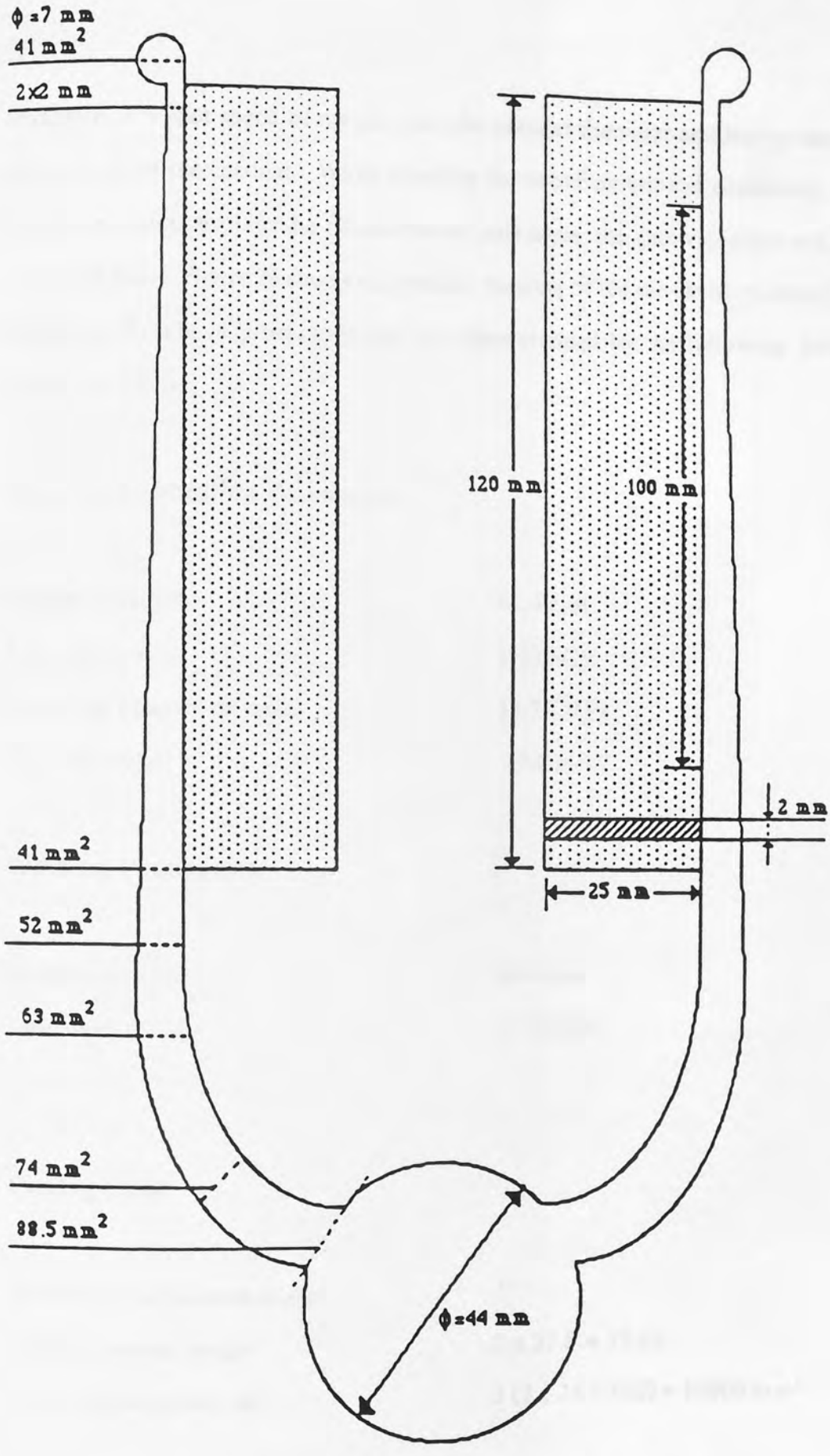

Figure 26 Die cavity design for thin section plates.

maximum dry shot speed of the plunger, the plunger diameter and line pressure) and volume of the castings. When selecting the above mentioned conditions, the computer screen displays the recommended gate areas, the gate velocities and the cavity fill time. Figure 26 shows a schematic drawing of the die cavity produced by following the above procedures and it is characterised by the following design parameters (3-4):

Machine Calibration Parameters:

Plunger diameter	44.4 mm
Line pressure	1.03 MPa
Maximum pressure on metal	33.73 MPa
Dry shot speed	7.6 m/s

Working Parameters:

Plunger diameter	44.4 mm
Line pressure	0.93 MPa

Casting Data:

Number of components in shot	2
Total component weight	2 x 37.8 = 75.69
Total component volume	2 (2 x 25 x 120) = 12000 mm^3

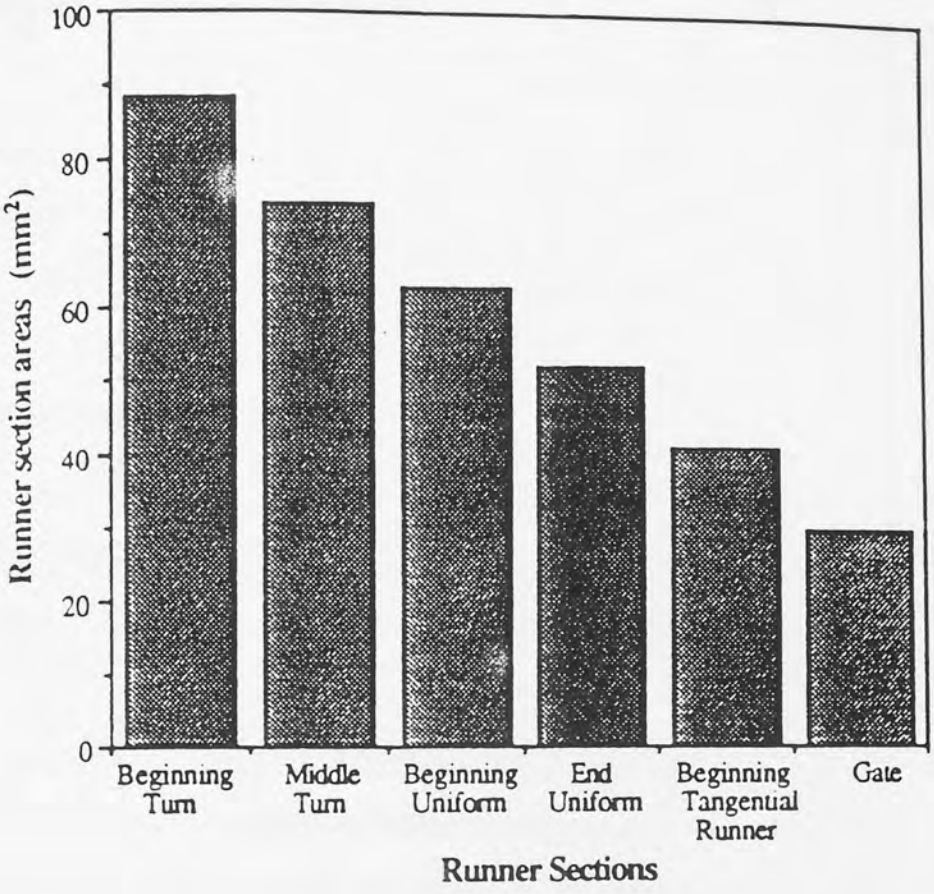

Figure 27 Decrease of the section along the flow path of the feed system of the die.

Figure 27a An example of the actual casting with runner system.

Selected Casting Conditions:

Gate area	60 mm
Gate velocity	58.1 m/s
Fill time	3.4 ms

Gate Dimensions:

Gate length	100 mm
Gate thickness	0.30 mm

Figure 27 shows a good hydrodynamic behaviour obtained from the design by smoothly decreasing sections from the feed system to the gate of the cavity. Earlier specimens, however show some porosity at the bottom corner of the samples, but by machining the gate length down to 110 mm this problem was overcome. Figure 27a shows an example of the actual casting with runner system.

3.1.2.2 Die Casting of the Alloys

The following procedures were followed due to recommendation of the guide-lines (5&6) which had been proposed for commercial alloy:

The ingots were placed into a clay-graphite crucible with a charge capacity of 20-30 kg. They were melted and left to stabilise at the required temperature in a small resistance furnace. Thermo couples were placed into the melt to monitor the temperature. During melting of ingots and prior to the metal transfer operation, the

bath was vigorously stirred to prevent aluminium segregation from the heavy zinc. The melt surface was then skimmed to remove any oxides and slags.

The die was preheated to a temperature of between 180-220 degrees C, two thermo couples (chromel/alumel) were located in the die block at a distance of 20 mm away from the middle of each impression.

The casting of the alloys was then started by varying the injection speed and pressure until optimum conditions were obtained During the casting the die faces were lubricated using an oil based lubricant (Dycote-2021). Once conditions were stabilised, about 30-50 castings were made in a batch. These were allowed to cool in still air to ambient temperature after ejection from the die. The rectangular castings were then removed from the runners and X-rayed to ensure that no grossly defective castings were used for experimentation.

3.2 DAMPING TESTS

A great deal of time was spent on finding a suitable method of measuring the damping capacity of the alloys produced. Four methods were used and they are as follows:

3.2.1 Frequency Sweep Method

A specimen was fixed to an electrodynamic vibrator and swept slowly through the frequency range 0-4000 hertz (using the frequency response analyser - FRA) to

excite the resonant frequencies. The FRA was driven by the programmed desk-top computer which also stored the response data which was then output to an X-Y plotter. The block diagram in Figure 28 describes the test instrumentations.

The resonant frequencies were identified by the attainment of a maximum vibration amplitude.

A low sweep rate with a step of 0.1 hertz, a delay of 1 second and a much lower frequency sweep was chosen. This improved the smoothness of the curve and it also magnified the curve in regions of resonance. The half power point method was then used to measure damping (as described in section 2.2.2).

3.2.2 Modal Analysis Method

A schematic diagram of the apparatus is shown in Figure 29. For this method the input forcing function was generated by an impact hammer type 8202 (manufactured by B & K) and measured by a force transducer attached to the hammer. The specimen's response was measured by a piezoelectric accelerometer of negligible mass which was mounted by means of wax.

The signals of both the hammer and the accelerometer were passed via amplifiers to a B & K dual channel analyser type 2032. The mentioned analyser offers many useful functions:

1) Automatic rejection of overload signals.
2) Advanced triggering facility, enabling the force and response

transducers to be connected directly to the analyser via the line drive amplifier.

The above mentioned are some of the many facilities available of the analyser.

After receiving the signals the analyser then transferred the signal data to a desk-top computer (IBM). The computer uses a software package capable of extracting modal parameters ie. natural frequency, modal constant and damping. The package was written by Pafec and is called Spiders II.

The damping was then calculated for each of the excited modes using the Nyquist diagram (described in section 2.2.3). A plot of the excited modes can also be produced.

As the beams used were quite small and with low mass it was thought that the mass of the accelerometer could have some effect on the test results. For this reason larger and heavier beams were gravity cast, and were tested in the same manner.

3.2.3 Free Decay Method

The B & K analyser was again used for this method, but was set to time domain so that the decay of vibration can be observed with respect to time.

For this test, a microphone of type B & K 2209 was used to pick up the signals produced from the specimen. This was done to eliminate any effect that the accelerometer may have had on damping properties, as the microphone is not

physically attached to the specimen. The microphone and the hammer were connected to the dual channel analyser and the specimen was excited, and then the vibration decay curve was seen on the screen of the B & K analyser. Measurements of the successive amplitudes of vibration were taken by moving the cursor to the point of each amplitude and taking a direct reading. The damping was then measured using the appropriate calculation for the free decay method (as described in section 2.2.1). A schematic diagram of the instrumentation set-up is shown in Figure 30.

3.2.3 Q Meter Method

For this method die cast beams were placed on highly stretched thin plastic wires on a purpose built rig. A microphone was placed beneath and in the middle of the sample to pick up signals from the beam. The beam was excited by a small hammer which was operated by a small electrical switch. This would ensure that all strikes of the hammer are all of the same force. A schematic diagram of the 'Q' meter is shown in Figure 31. After excitation of the beam, signals are passed through an amplifier and then through a 4-pole filter, this procedure amplifies the signals and then the filter filters out unwanted signals to produce a smooth vibration curve. The filtered signal is then passed to two comparators which produce a window in which the numbers of cycles are counted. The two counters then show frequency in hertz and the number of cycles counted which can be used to calculate 'Q'. A photograph of the instrumentation set-up is shown in Figure 32.

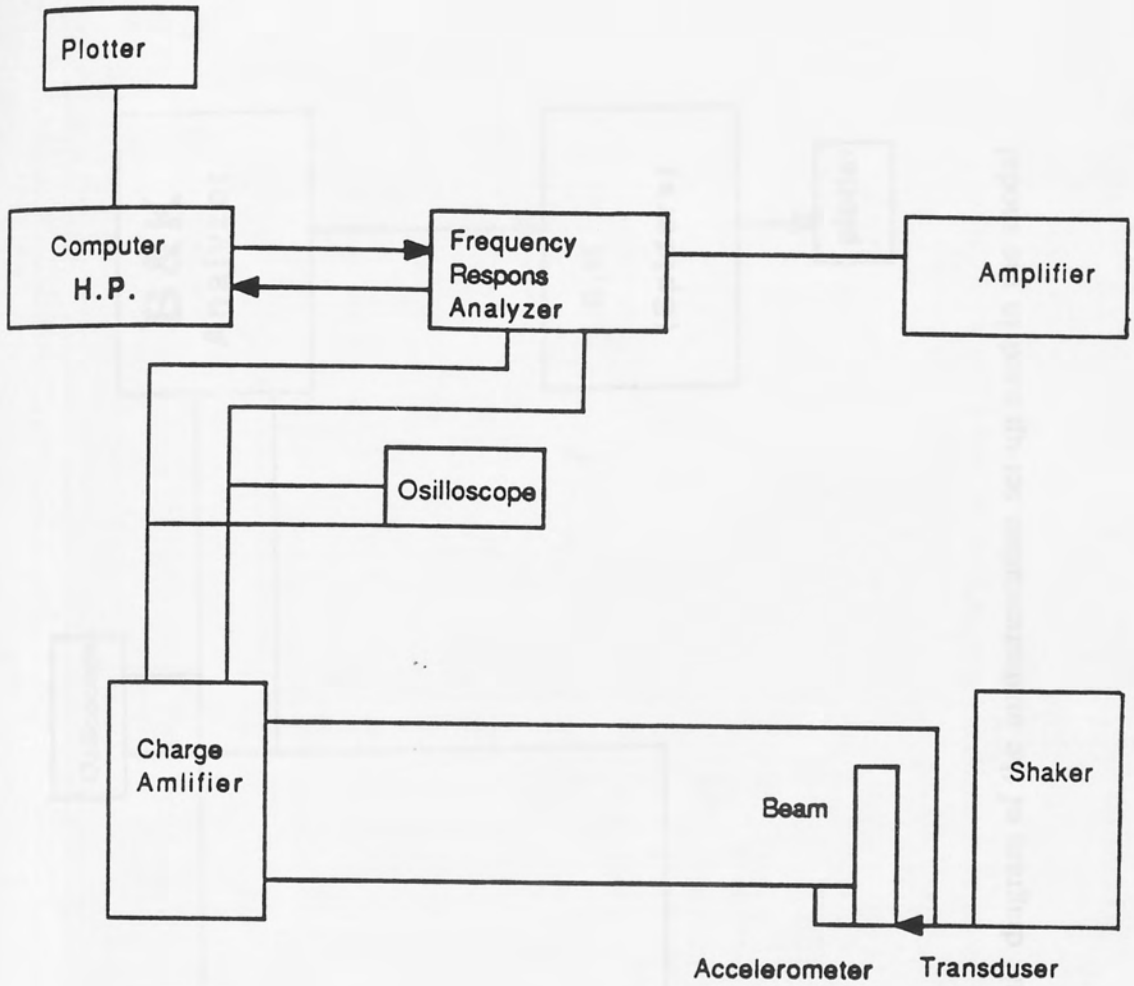

Figure 28 Schematic diagram of the instrumentation set-up used in the half power point method.

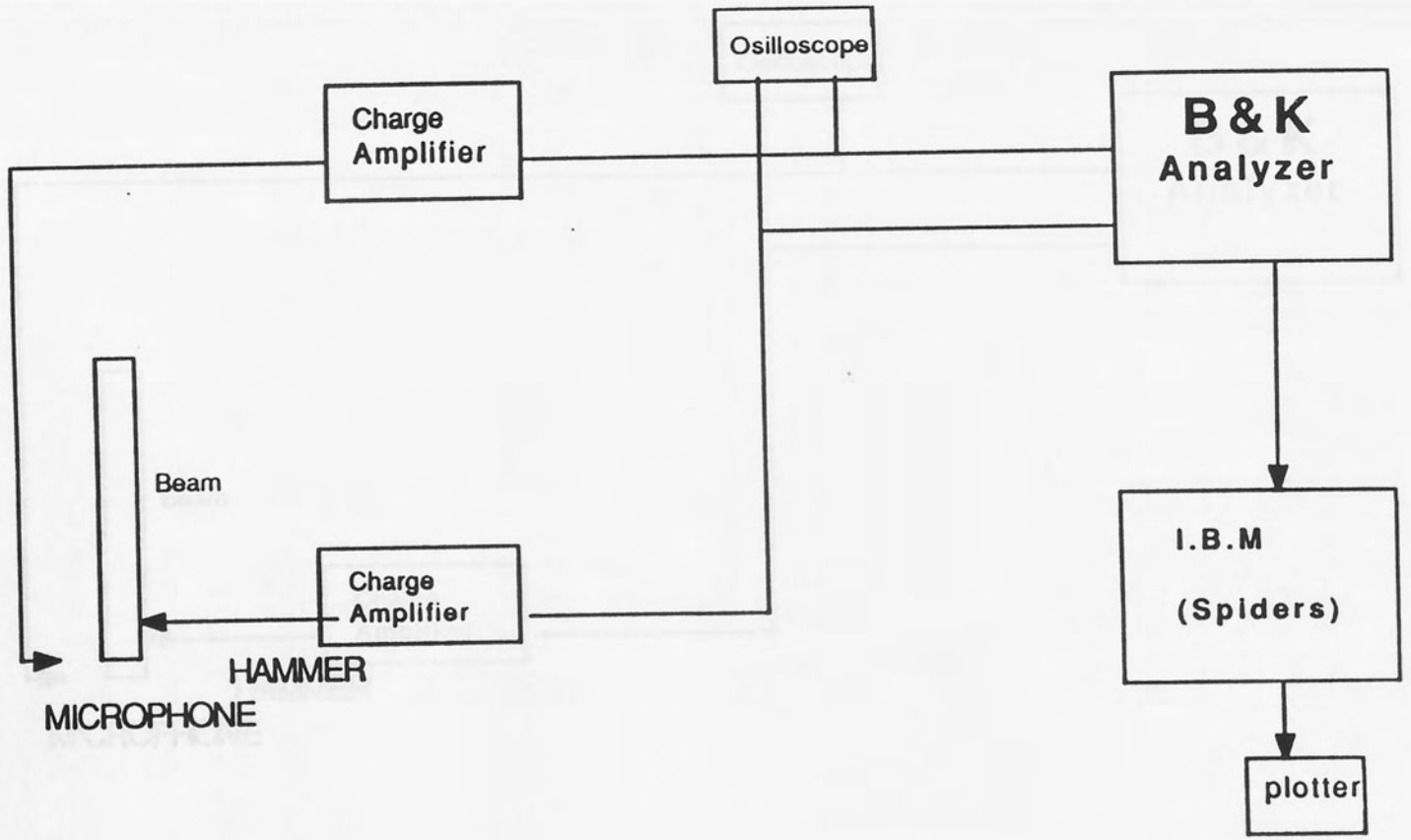

Figure 29 Schematic diagram of the instrumentation set-up used in the modal analysis method.

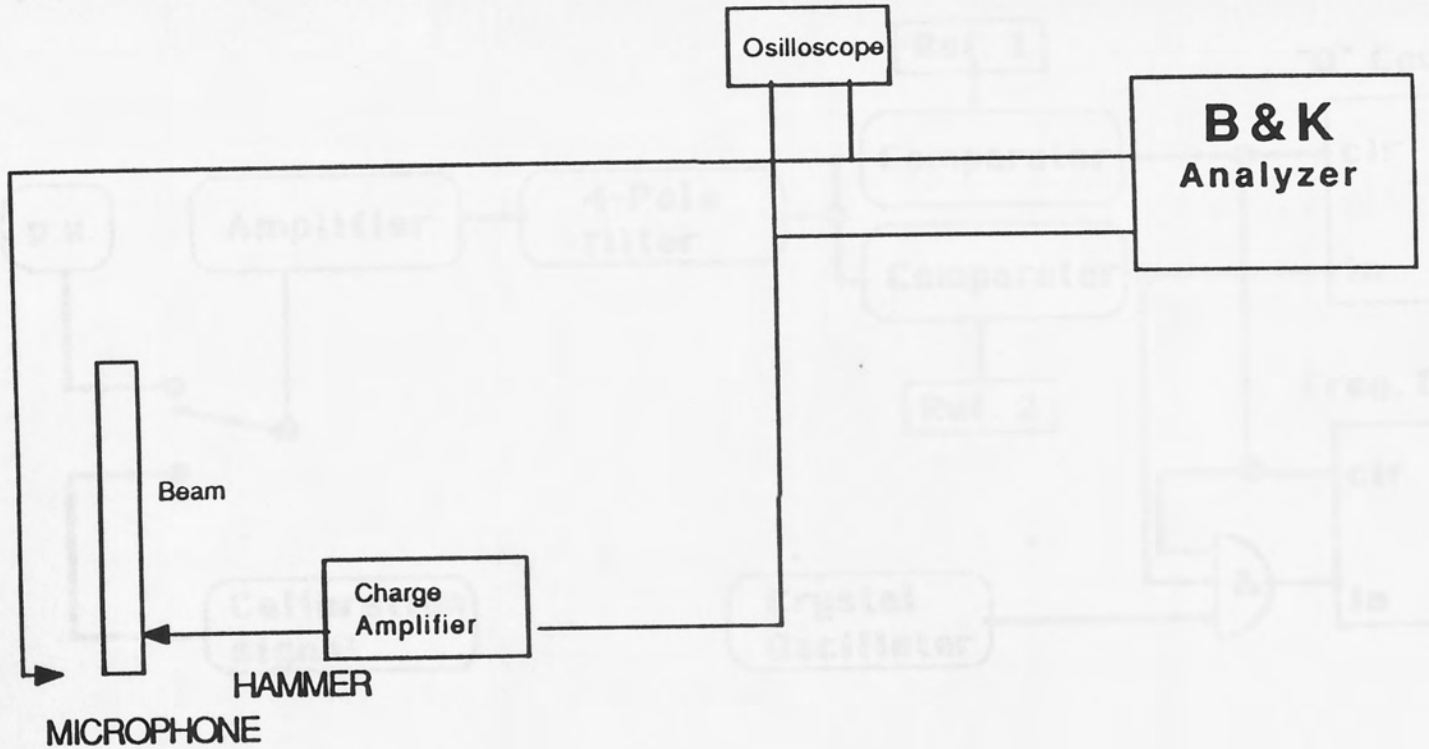

Figure 30 Schematic diagram of the instrumentation set-up used in the free decay method.

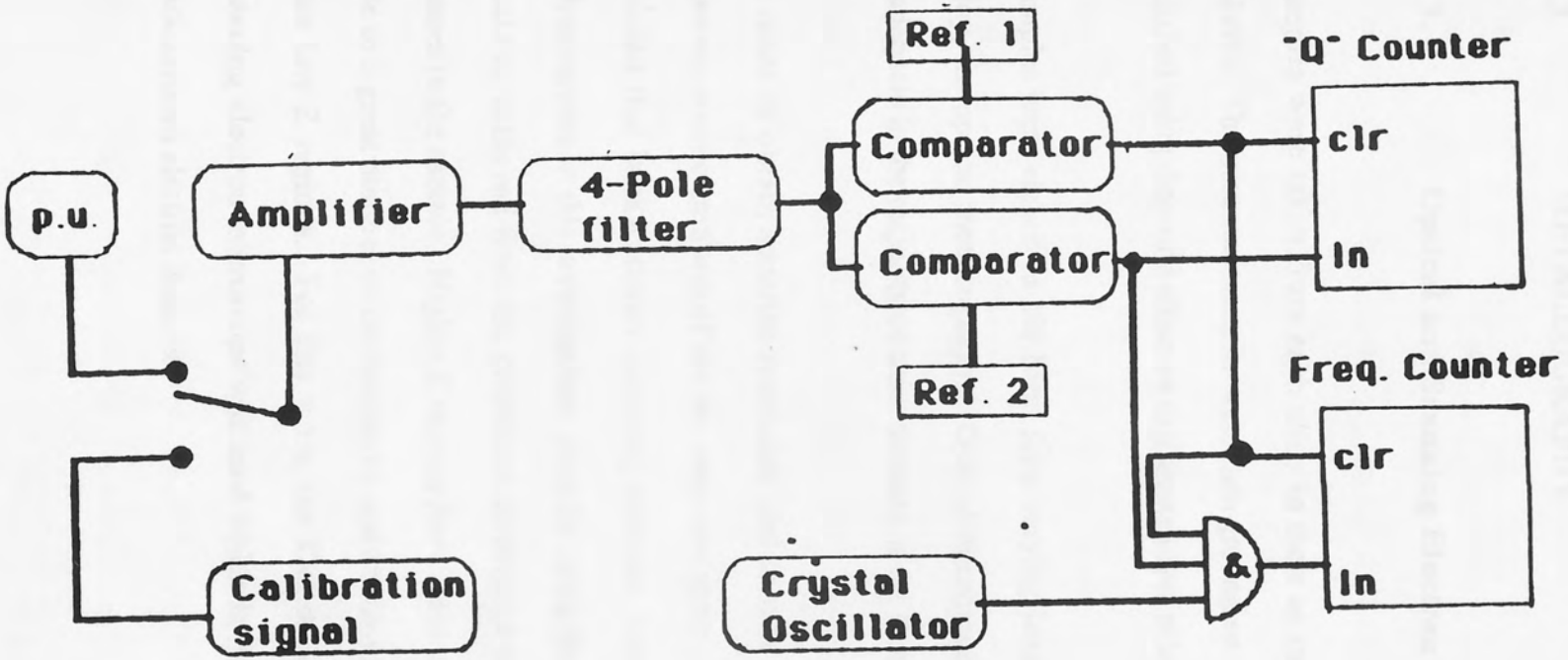

Figure 31 Schematic diagram of the instrumentation set-up used in the Q-metre method.

3.3 METALLOGRAPHY

3.3.1 Optical and Scanning Electron Microscopy

Samples were taken from each alloy in their as cast condition and mounted in bakelite. The mounted samples were then ground on silicon carbide paper, and then polished using diamond abrasive to a scratch-free mirror surface.

Samples were etched in 2% Nital for a varying length of time, depending on the alloy, for optical metallography. Optical microscopy, however, was found to be inadequate in the majority of cases because of the fine structure of the alloys.

In order to obtain superior resolution and to take advantage of the difference between atomic numbers of the two main elements (Zn and Al) of the alloys it was decided that backscattered scanning electron microscopy (S.E.M.) would be advantageous in this investigation, since by using backscattered electrons, contrast could be achieved from the difference in average atomic number (Z) of various phases in the sample. Higher Z regions have more nuclear change and hence give rise to a great number of backscattered and smaller number of absorbed electrons than low Z regions. For this work the Cambridge Instruments S.E.M. 150 scanning electron microscope was used which is fitted with a special large area, backscattered electron detector.

3.3.2 Transmission Electron Microscopy

Detailed examination of the as-cast structure of the die cast Cosmal alloys ZM11 , Cosmal and Super Cosmal were made on the transmission electron microscope using thin foil samples.

3.3.2.1 Preparation of Thin Foils

Samples were taken from test beams and initially thinned by wet-grinding on silicon carbide paper. Grit sizes used were 120 or 160. The next stage was to produce discs of 3mm diameter, these were produced from thinned samples by means of a spark-erosion in a Servomet spark-erosion machine. The cut discs were then further thinned by wet grinding with 1200 grit abrasive paper, down to about 100 μm to obtain flat and parallel sided faces.

Final thinning of the disc samples was carried out by electropolishing in a commercial double jet electropolisher - the Tenupol (Struers Ltd) - shown in Figure 33, which consists of the following:

Polishing cell and pump which circulates electrolyte through the dual jets which are directed at the centre of the 3mm disc sample. The sample was mounted in a removable sample holder and the anode potential was applied via a platinum strip which runs through the centre of the holder where the sample was placed.

Jets simultaneously thinning both sides of the sample produced a concave hollow on each of the sides, as soon as a complete penetration occurs, usually in the middle of the sample, the polishing was automatically stopped and a buzzer was sounded.

The electrolyte used in the electropolisher was a mixture of perchloric acid (10 - 20%) and ethanol and had to be kept at a temperature of -30 to -40 degrees C. Liquid nitrogen was used to keep the mixture at the above mentioned temperatures.

The electrolyte mixture was as follows:

30cc perchloric acid (d=1.54)

250cc 2-Butoxyethanol

700cc ethanol

3.3.2.2 Transmission Electron Microscopy

The polished thin foil samples were then examined in two different transmission electron microscopes, and Phillips EM300 and a Phillips EM400T. Both were operated at an accelerating voltage of 100 kV. The three main modes of operation of this equipment were as follows:

Conventional TEM mode - bright and dark field images of the structures were studied with corresponding selected area diffraction patterns (SADP).
The tilting technique, using a double-tilt stage, was used in order to obtain three dimensional information and allowed the section of particular crystallographic directions to reveal structure and to differentiate the diffraction patterns of small particle with similar lattice parameters to the matrix phase.

The second application for which transmission electron microscopy was used, was to obtain high magnification structural photographs and to observe them.

The third and final application was to use the STEM mode of the microscope and an X-ray energy analyser (EDS) to analyse the chemical composition of the present phases. To be able to analyse extremely small phases, the smallest probe was obtained by switching off the second condenser lens and increasing the strength of the first lens and using the second condenser lens' aperture. Then the probe was focused onto the area to be analysed using the objective lens.

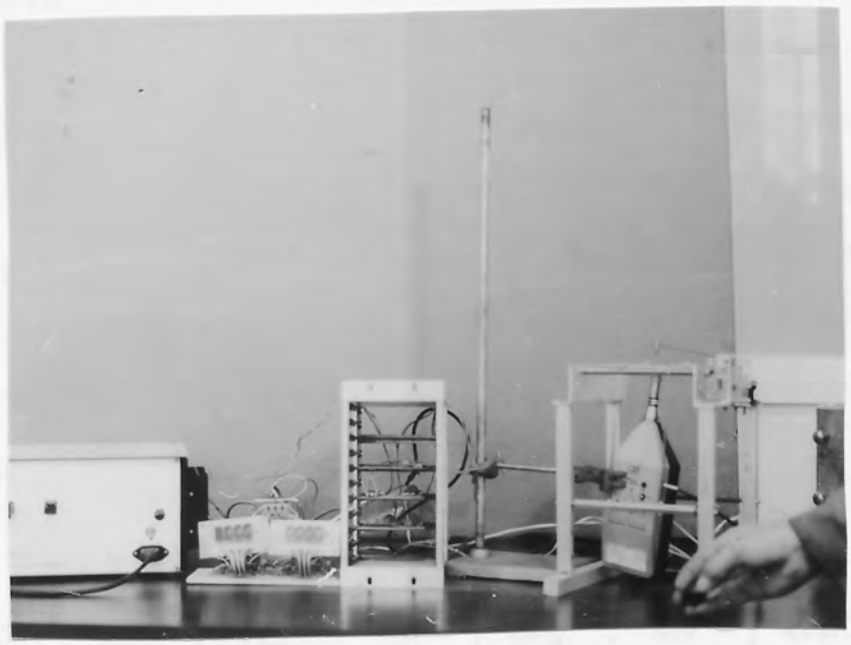

Figure 32 instrumentation set-up used in the Q-metre method.

Figure 33 The electropolisher (Tenupol, Struers Ltd).

CHAPTER 4

4.0 EXPERIMENTAL RESULTS

4.1 CHEMICAL COMPOSITIONS OF EXPERIMENTAL ALLOYS

Initially, experiments were carried out on M3, ZA8, ZA27, ZM11, Cosmal and Super Cosmal alloys. These alloys were produced by means of pressure die-casting at Aston's foundry. Two further alloys were based on standard ZA27 with variable copper and silicon contents, these alloys were called ZA27H1 and ZA27H2. Table 10 shows the chemical compositions of all the experimental alloys:

Alloy	% Al	% Cu	%Si	%Mg	%Fe	%Mn	%Zn
ZM11	23.1	0.57	0.8	0.049	0.05	0.34	rem
Cosmal	42.8	1.05	3.41	0.008	0.13	0.3	rem
S.Cosmal	54.9	0.97	5.72	0.002	0.15	0.33	rem
ZA27	28.5	2.1	-	0.016	0.1	-	rem
ZA27H1	30.8	1.12	-	0.002	0.06	0.46	rem
ZA27H2	30.1	1.15	1.88	0.002	0.006	0.27	rem
ZA8	8.1	1.06	-	0.024	0.01	-	rem
M3	4.2	<0.003	-	0.049	<0.01	-	rem

Table 10. Composition of the experimental alloys (%wt).

4.2 METALLOGRAPHY OF THE EXPERIMENTAL ALLOYS

The as-cast structures of the experimental alloys M3, ZA8, ZA27, ZA27H1,ZA27H2, ZM11, Cosmal and Supercosmal were examined under the SEM using the backscattered electron imaging. For further investigation, alloys ZM11, Cosmal and Supercosmal were examined under TEM.

4.2.1 M3 ALLOY

The as-cast structure of M3 alloy is shown at four different magnifications in Figures 34-36. The structure of this alloy consisted of primary η surrounded by pools of eutectic. The structure of this alloy was heterogeneous, but was clearly hypoeutectic, as shown in Figure 34 at low magnification. Also seen in Figure 34, were some dark areas. These are gas porosity, which has resulted from the pressure die casting process.

Figure 35 shows tiny dark particles on the edges of primary η. These were highlighted at higher magnification in Figure 36 these particles are pseudo-primary aluminium-rich former β phase, which are believed to be a result of the high undercooling during eutectic solidification. These had subsequently decomposed into aluminium-rich α phase and zinc-rich η phase mixtures at below the eutectoid temperature of 275°C. It is also seen in these figures that the edges of the primary η dendrites were decorated with thin haloes of the eutectic aluminium rich α phase. These haloes were formed due to the process of removing excess aluminium from the super-cooled liquid before normal eutectic solidification took place. This is because the solubility of aluminium in zinc is very small at low temperatures. In these Figures the eutectic phase had formed into plates or lamellae of β phase in a zinc-rich η matrix, the β phase

had also decomposed on cooling through the eutectoid temperature after solidification. The former β plates had decomposed into rows of aluminium α particles or thinner plates of α, the η constituent joining the η matrix.

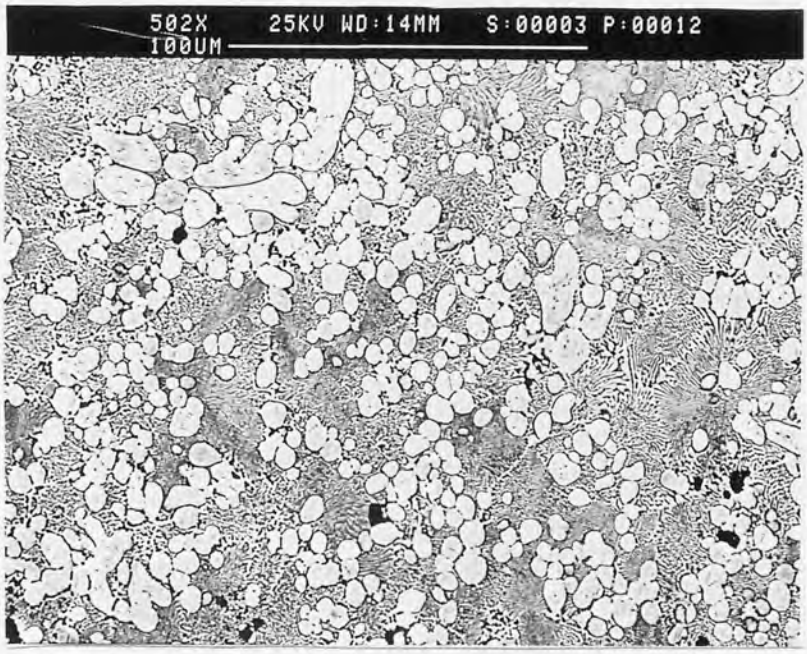

Figure 34: SEM as-cast structure of M3 showing primary η of different sizes surrounded by the eutectic, also seen in this figure is some gas porosity.

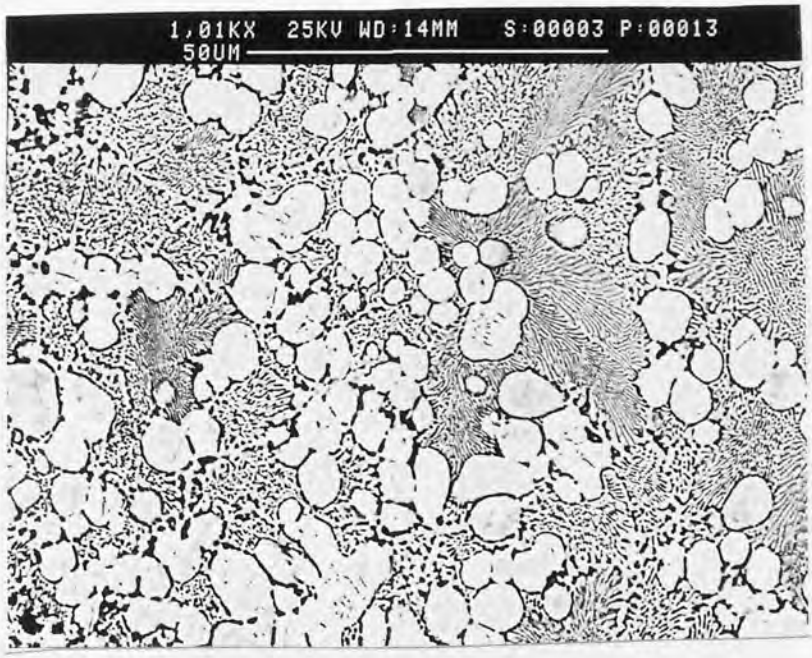

Figure 35: SEM as-cast structure of M3 showing primary η of different sizes surrounded by the eutectic, which is in lamellar or particulate form.

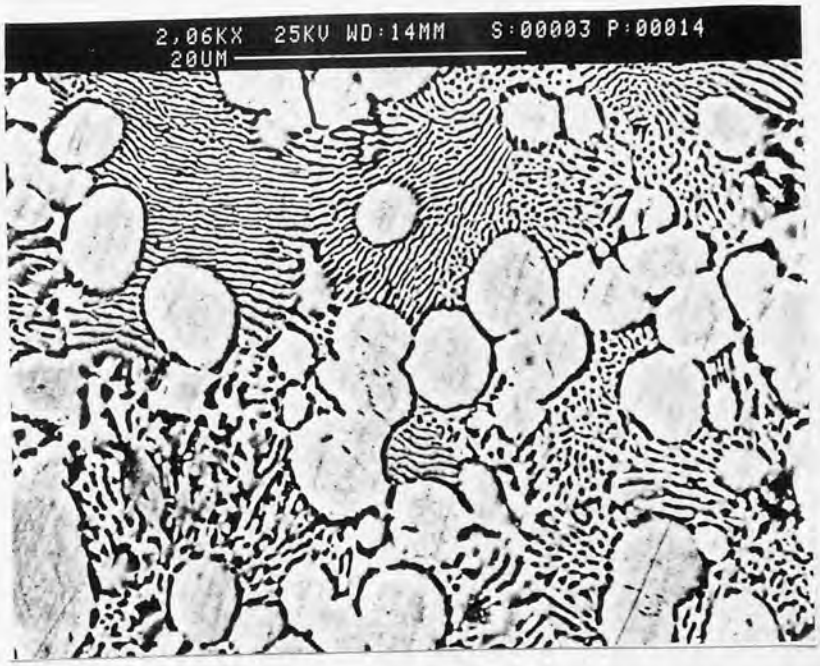

Figure 36: SEM as-cast structure of M3 showing a few former β particles formed on the primary η particles, also present are some pseudoprimary β in the bottom right hand corner.

4.2.2 ZA8

The as-cast structure of ZA8 alloy is shown at four different magnifications in Figures 37-41. The structure of this alloy was heterogenous and and was clearly hypereutectic. The structure of this alloy consisted mainly of primary β particles surrounded by pools of eutectic as shown in Figure 37, also seen in this figure, was the zinc rich η phase with almost the same size and shape as the primary β phase. The η areas are believed to be pseudoprimary η and they were believed to have formed from a highly supersaturated zinc-rich liquid below the eutectic temperature during the rapid cooling of the castings. Figures 38, 39, 40, and 41 show that β had decomposed into two different morphologies, a well developed lamellar form situated in the centre portion of the grains surrounded by a rim of coarser mixture of phases. Also seen but less frequently was a coarser mixture of phases which occupied the entire grain. Figures 39, 40 and 41 show the presence of thin layers of η phase formed around the edges of primary β dendrites and were formed by nucleation of η on the pre-existing β, as an alternative to pseudoprimary particle formation.

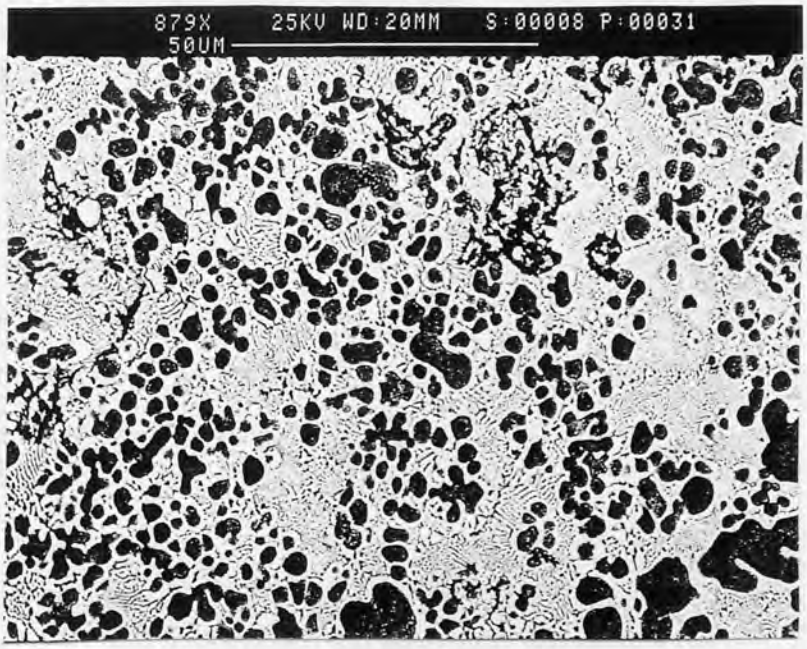

Figure 37: SEM as-cast structure of ZA8 showing primary β particles of different sizes and shapes surrounded by eutectic η particles of similar size and shape as the primary β are also present in this figure, at the left-hand edge some shirinkage porosity can also be seen.

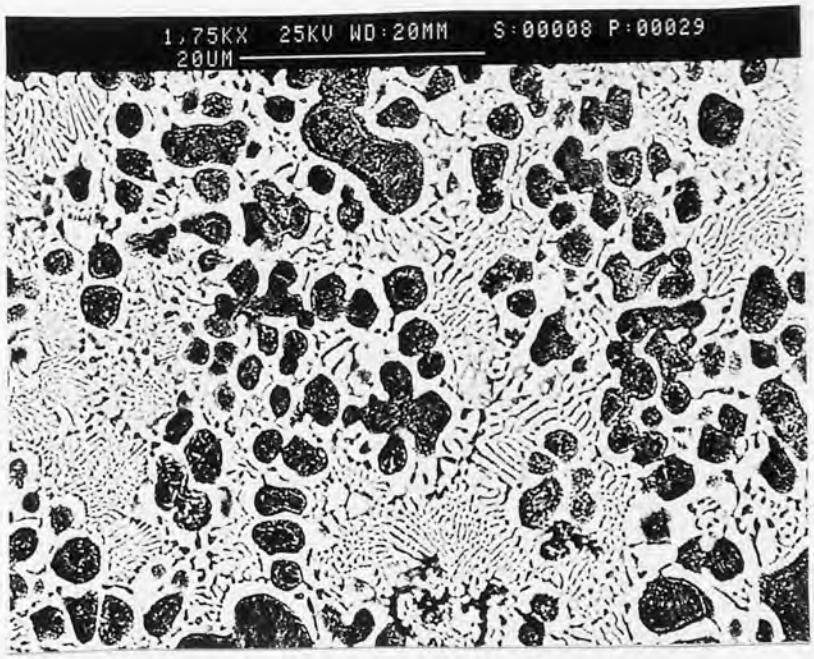

Figure 38: SEM as-cast structure of ZA8 showing a variety of decomposition structures in the former β dendrites, and lamellar eutectic morphologies.

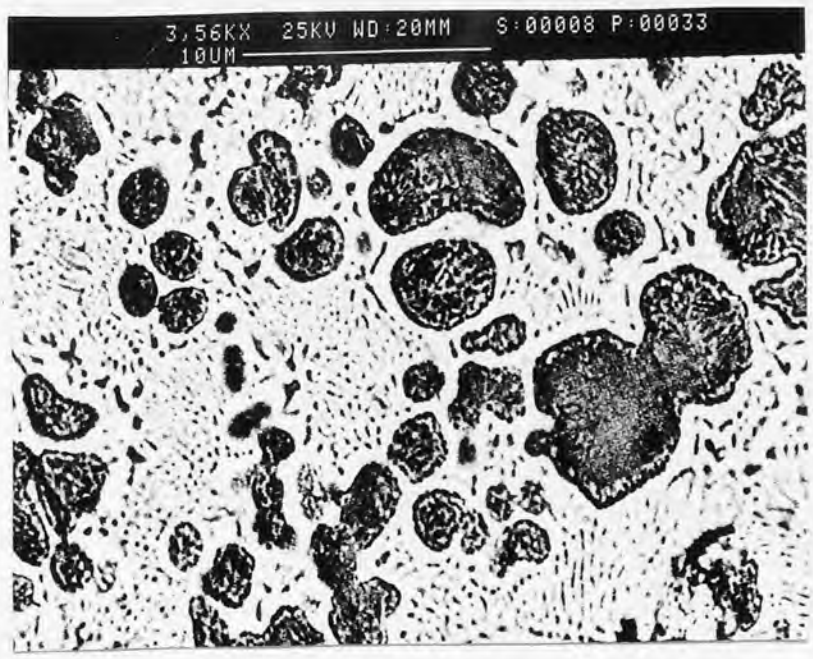

Figure 39: SEM as-cast structure of ZA8 showing decomposed β and eutectic matrix, figure also shows some particulate eutectic morphologies.

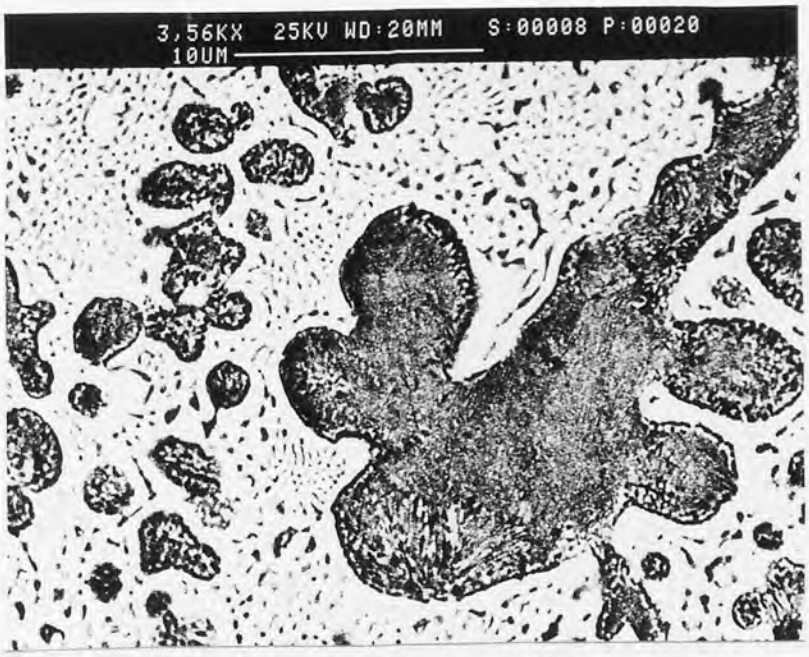

Figure 40: SEM as-cast structure of ZA8 showing decomposed β and eutectic matrix. The figure focused on a peculiar shaped β dendrite.

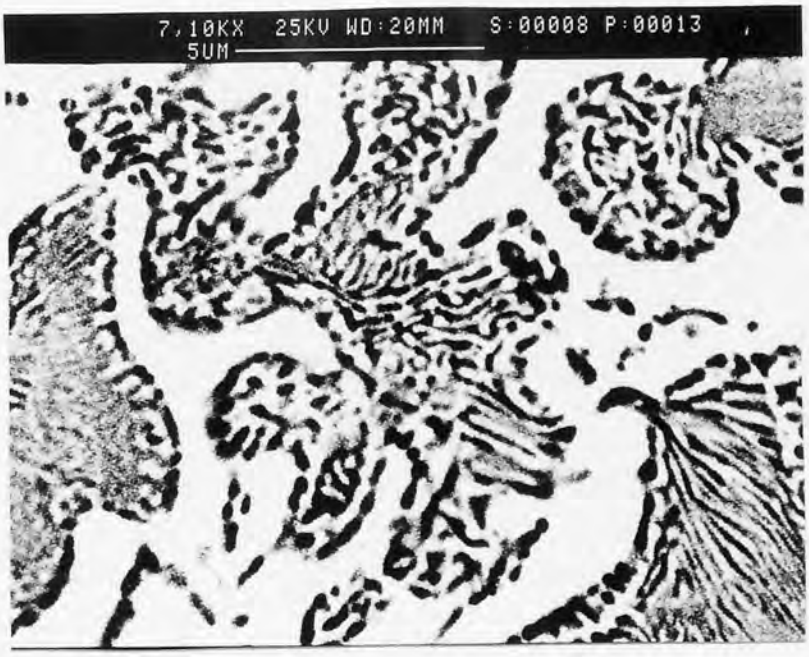

Figure 41: SEM as-cast structure of ZA8 using different contrast to figure 40 showing the decomposition of β into nicely formed lamellae and a coarse mixture of phases at the edge.

4.2.3 ZA27 ALLOYS

4.2.3.1 ZA27

The as-cast structure of ZA27 is shown in Figures 42-46 at five different magnifications. The structure of this alloy was heterogeneous and showed a multi-phase complex structure. The dark phase was fine dendritic α, enclosed within a much smaller volume of zinc-rich β and with interdendritic eutectic zinc η, as shown in Figure 42 at low magnification. Higher magnifications as in Figure 43-46, revealed that the solidification of this alloy had started with the formation of aluminium-rich α-α' dendrites, this was then followed by the formation of zinc-rich β phase mainly around the primary dendrites, through a peritectic reaction between the first formed α phase and the residual liquid. This peritectic reaction was far from complete due to the rapid cooling, so that much aluminium was locked up in the dendrite cores. The zinc-enriched residual liquid had finally solidified by an eutectic reaction.

On cooling through the region of solid-state transformation after casting, the α' cores had decomposed by a mixture of spinodal and cellular reactions, the former producing areas of fine precipitates too small to resolve in the SEM. The cellular decomposition was initiated by the decomposition of the β rim, the lamellar colonies of which grew into the α' cores. The zinc-rich lamellae widened their spacing as they grew into the cores, reflecting the higher aluminium content of that phase relative to β, this is clearly shown in Figures 45 and 46.

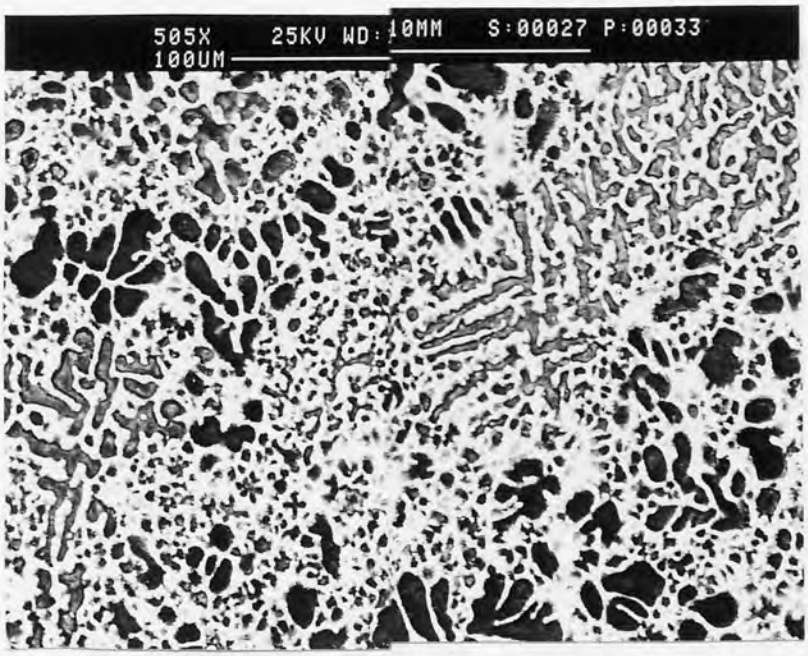

Figure 42: SEM as-cast structure of ZA27, showing dark phases of fine α dendrites surrounded by β with small amounts of interdendritic η.

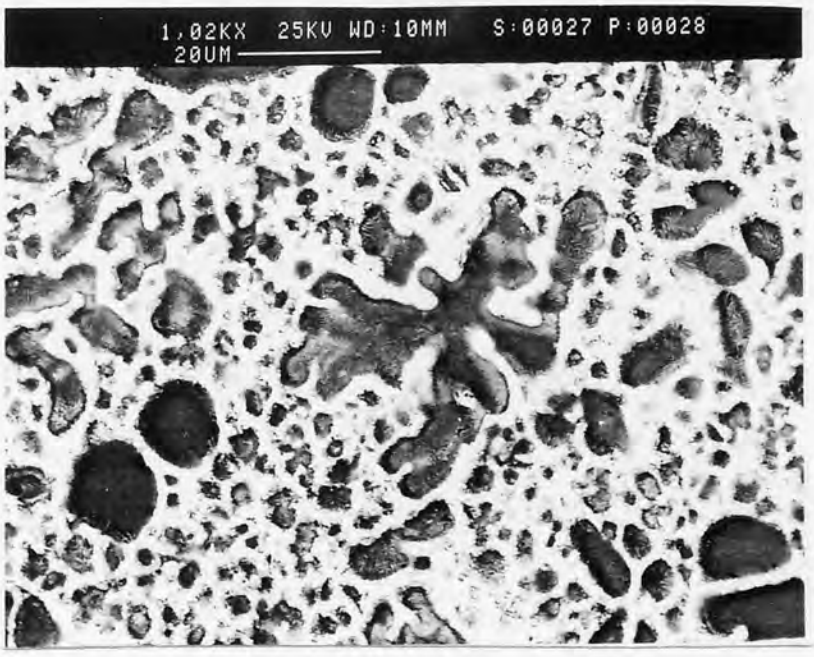

Figure 43: SEM as-cast structure of ZA27 showing a fine structure of former α particles surrounded by β and interdendritic η.

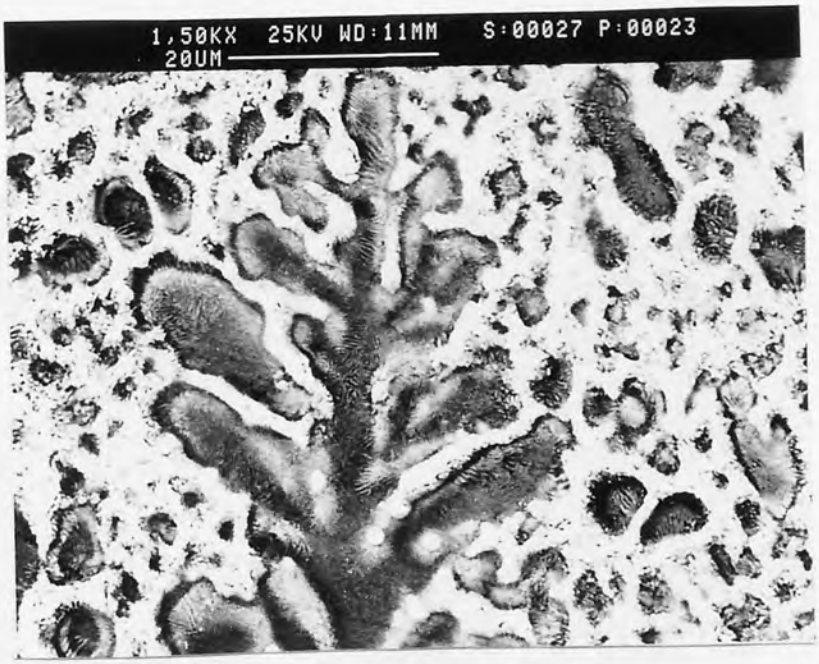

Figure 44: SEM as-cast structure of ZA27 showing the decomposed α' and β.

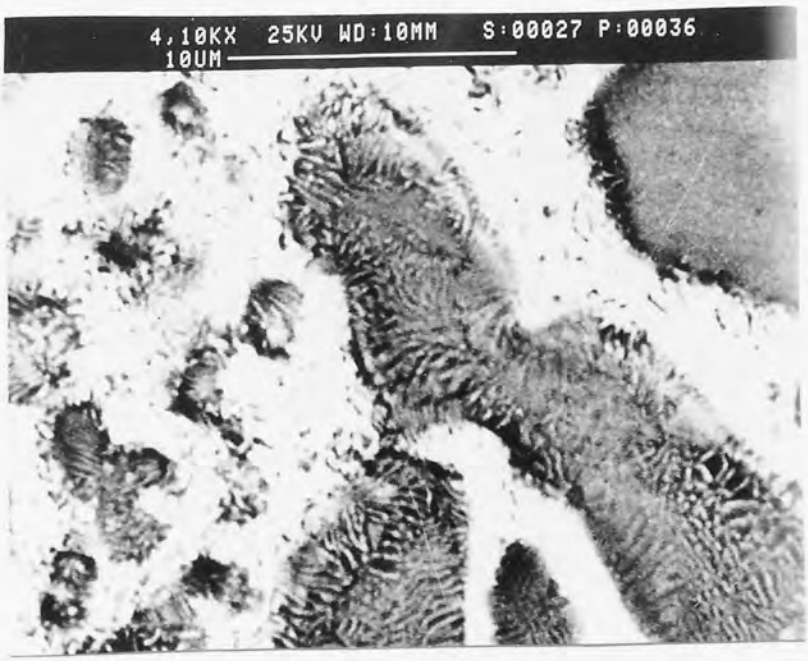

Figure 45: SEM as-cast structure of ZA27 showing the decomposition of α' particles.

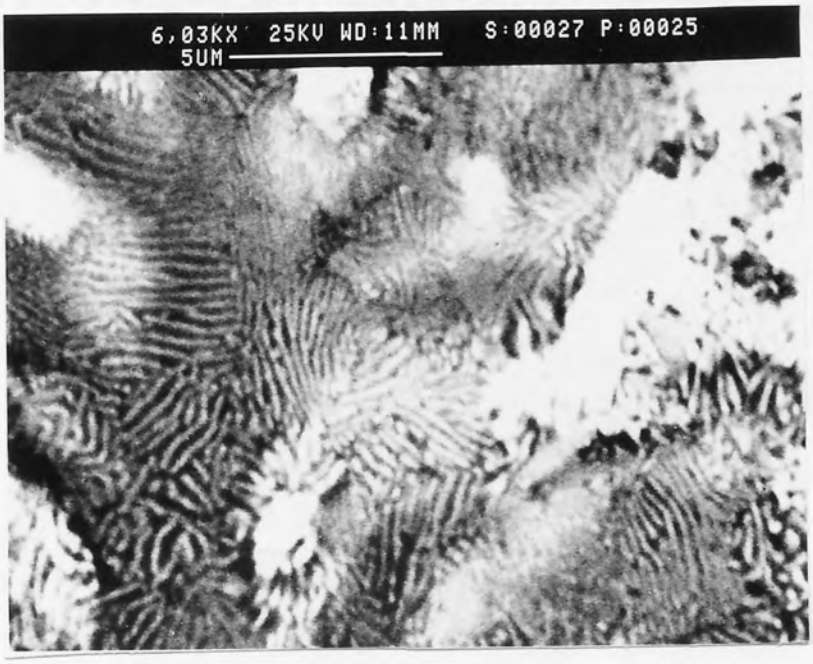

Figure 46: SEM as-cast structure of ZA27 at high magnification showing the final product of decomposition of α' and β.

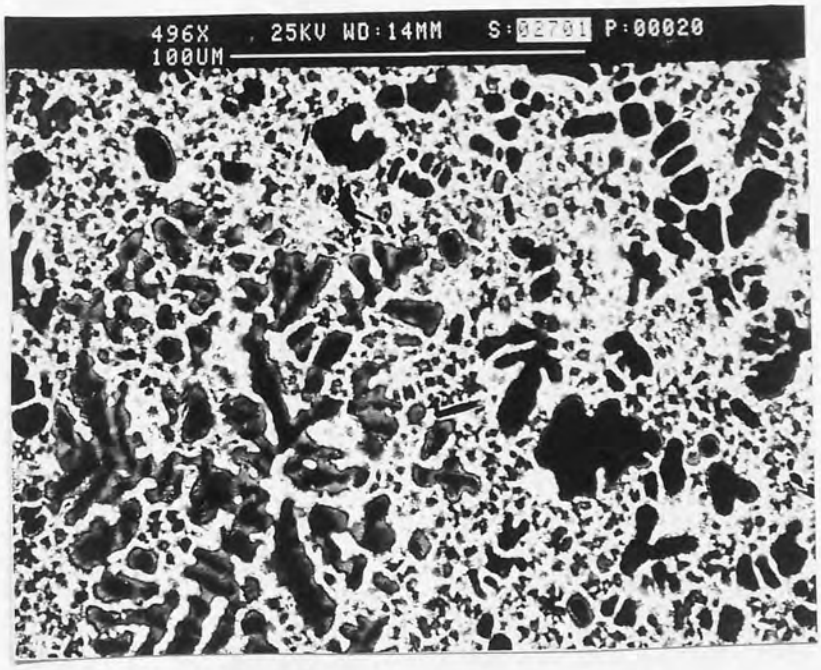

Figure 47: SEM as-cast structure of ZA27H1 showing α' dendrites surrounded by β with small amounts of interdendritic η, also seen are some rod like intermetallic particles.

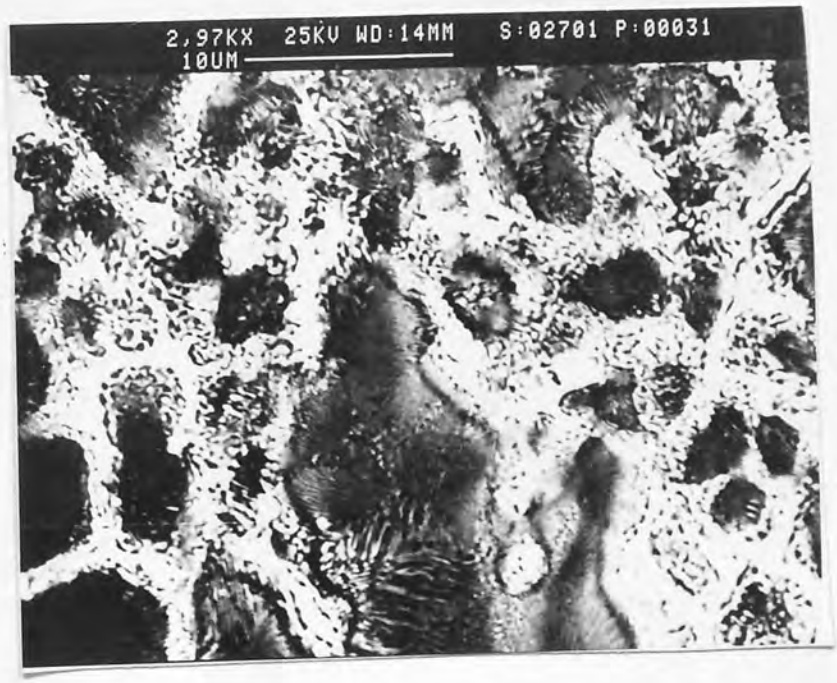

Figure 48: SEM as-cast structure of ZA27H1 showing the decomposition of α' into fine particles or lamellar products.

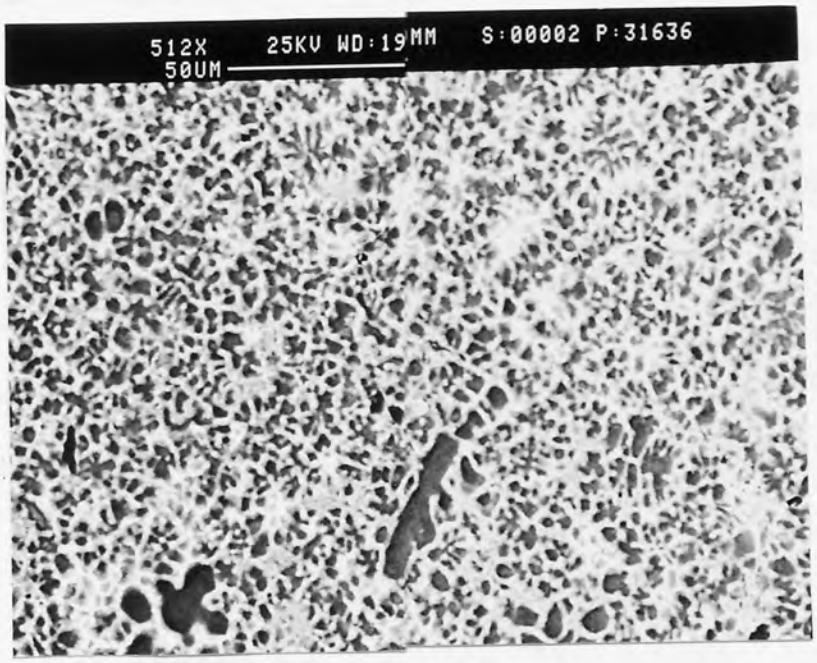

Figure 49: SEM as-cast structure of ZA27H2 showing a fine structure of former α' primary particles surrounded by β and interdendric η, also present in this figure are some silicon particles.

Figure 50: SEM as-cast structure of ZA27H2 showing the decomposition of α' into particles.

4.2.3.2 ZA27H1

The as-cast structure of ZA27H1 is shown in Figures 47 and 48 at two different magnifications. The structure of this alloy was very similar to that of ZA27 . Figure 47 at low magnification shows α' dendrites surrounded by β with small amounts of interdendritic η, also present in this figure are some rod-like intermetallic particles. At high magnification, Figure 48 shows the decomposition of α' into fine particles or lamellar products as in ZA27.

4.2.3.3 ZA27H2

The as-cast structure of ZA27H2 is shown in Figure 49 and 50 at different magnifications. The structure of this alloy is similar to that of ZA27 and ZA27H1. At low magnification, Figure 49 shows a fine structure of former α' particles surrounded by β and interdendrite η ; also present in this figure are small dark silicon particles. The structure of this alloy consisted of fine irregular sized α dendrites surrounded by β. Figure 50 at higher magnification shows the decomposition of α' particles as described for ZA27.

4.2.4 ZM11

The as-cast structure of ZM11 is shown in Figures 51-54 at different magnifications. The structure of this alloy was heterogenous in that it contained a few large dendrites and many smaller primary particles and was clearly hypereutectoid. Figure 51, at low magnification shows the general structure of this alloy to consist of former α dendrites surrounded by a mixture of α and η particles, which were the results of the decomposition of the

surrounding β at the eutectoid temperature. The structure is in between that of ZA27 and ZA8, consistent with the aluminium content being slightly lower than that of ZA27. The dark particles seen in this figure were analysed and were found to consist mainly of silicon.

Figure 52 at higher magnification shows a coarse mixture of α+η in the former β region and small dark particles of silicon, mostly associated with the aluminium-rich areas.

Figure 53 and 54 at two different magnifications show nicely formed lamellae in dendrites. Also seen in these figures, are cellular colonies in the α' and β, where the cells have nucleated on the η then spread though the β and thickened as they penetrated the α' phase, which is what occurred in ZA27.

The structure of this alloy was also examined by TEM as shown in Figures 55-58.

Figure 55 shows part of an α dendrite such as those seen in Figure 53. In the centre of the α - dendrite, widely spaced lamellae branch out in a three-dimensional network sectioned by the plane of the foil. Figure 56 was taken from the edge of an α-dendrite. The lamellae in this case were mostly oriented parallel to one direction.

Figure 57 shows a discontinuous lamellar arm, also seen in the centre of this lamella are some comparatively large precipitates, which were analysed and were found to be an Al-rich phase. Further analyses were made on Figure 58 and the results are shown in Table 11. A selected area diffraction pattern was taken from the arrowed area in Figure 57 and it was found to be aluminium with a beam direction of $[2\bar{1}1]$. The SADP can be seen in Figure 59, which

also shows the points indexed. Figure 60 shows a stereographic projection with the great circle on which points of indexing lie marked.

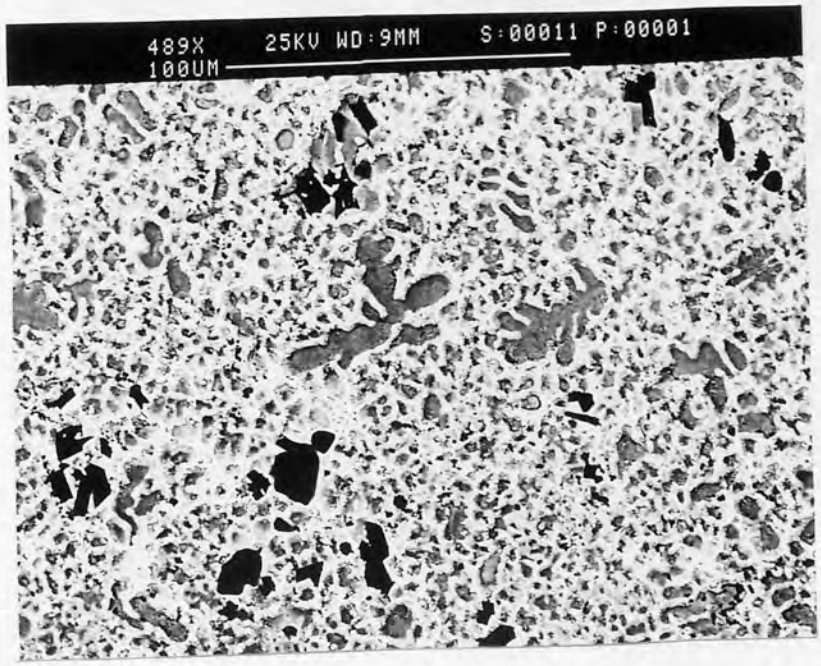

Figure 51: SEM as-cast structure of ZM11 showing the former α' dendrites in a mixture of transformed β and eutectic η . The dark particles are silicon.

Figure 52: SEM as-cast structure of ZM11 showing a coarse mixture of $\alpha + \eta$ (eutectoid), also present are some silicon particles which are associated with the α'.

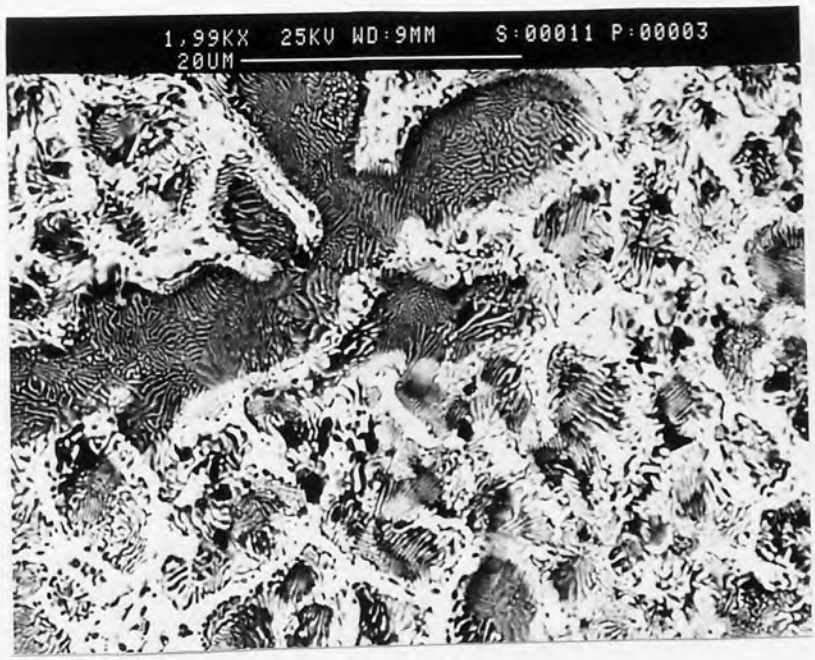

Figure 53: SEM as-cast structure of ZM11 showing an α' dendrite with nicely formed lamellae.

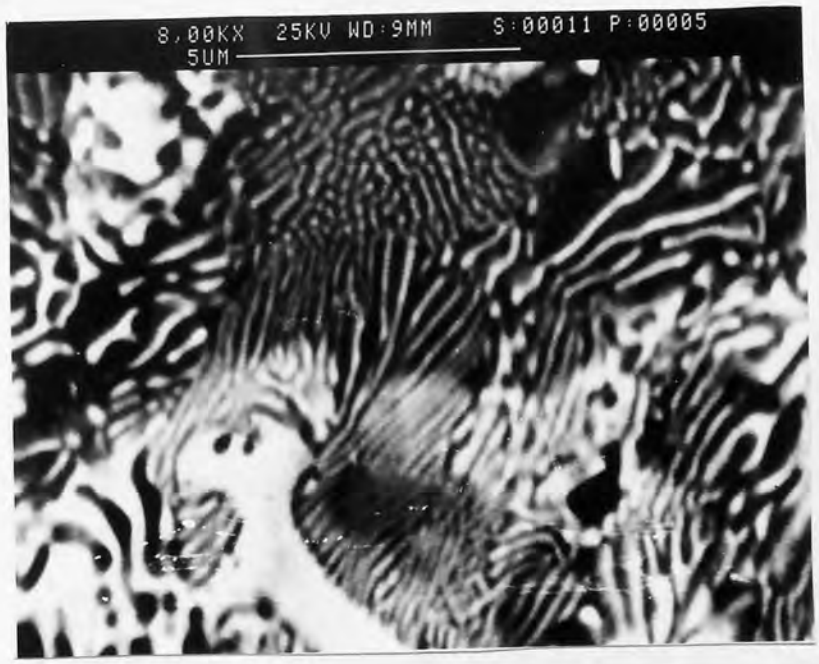

Figure 54: SEM as-cast structure of ZM11 showing Figure 53 at higher magnification, showing nicely formed patterns of cellular decomposition in α and β. The cells are nucleated on the η and thickened as they grew into the α' phase.

Figure 55: TEM as-cast structure of ZM11 taken from an α dendrite showing lamellar arm branching out from the centre in a three dimensional network sectioned by the plane of the thin foil. The irregular mats of dark particles are oxides formed during electro-polishing

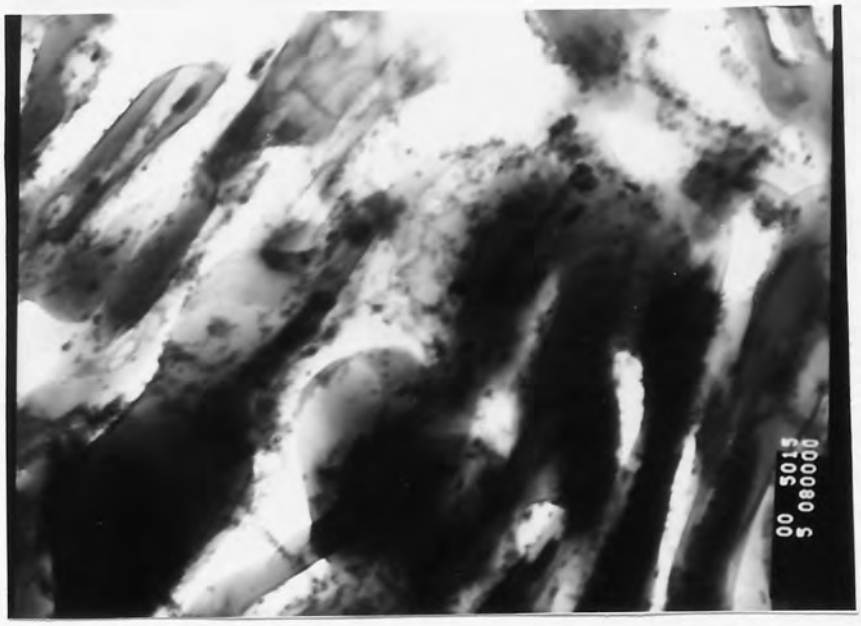

Figure 56: TEM as-cast structure of ZM11 taken from the edge of the α dendrite showing the lamellae arms, also enclosed within these arms were precipitates of different sizes and shapes.

Figure 57: TEM as-cast structure of ZM11 at high magnification showing large precipitates (arrowed) enclosed within the lamellae, these precipitates were analysed and were found to be α_m phase.

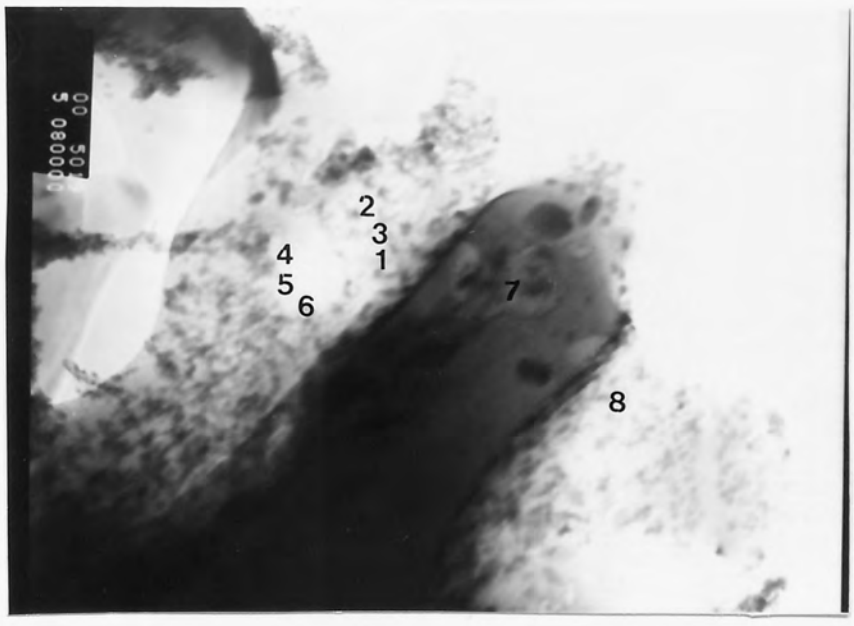

Figure 58: TEM as-cast structure of ZM11 (the numbers on this micrograph, are the points of analyses).

A

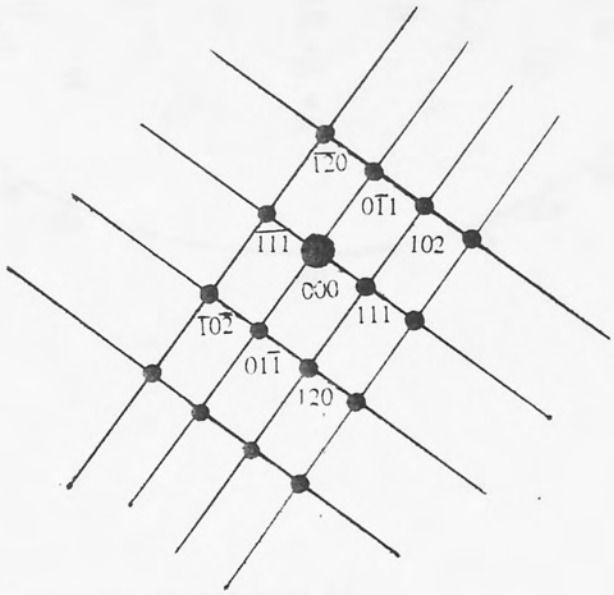

B

Figure 59 : a) SADP taken from the arrowed area on Figure 57, showing a diffraction pattern with a beam direction of $[\ 2\bar{1}\bar{1}\ ]\ \alpha$.

b) Indexing of the above pattern.

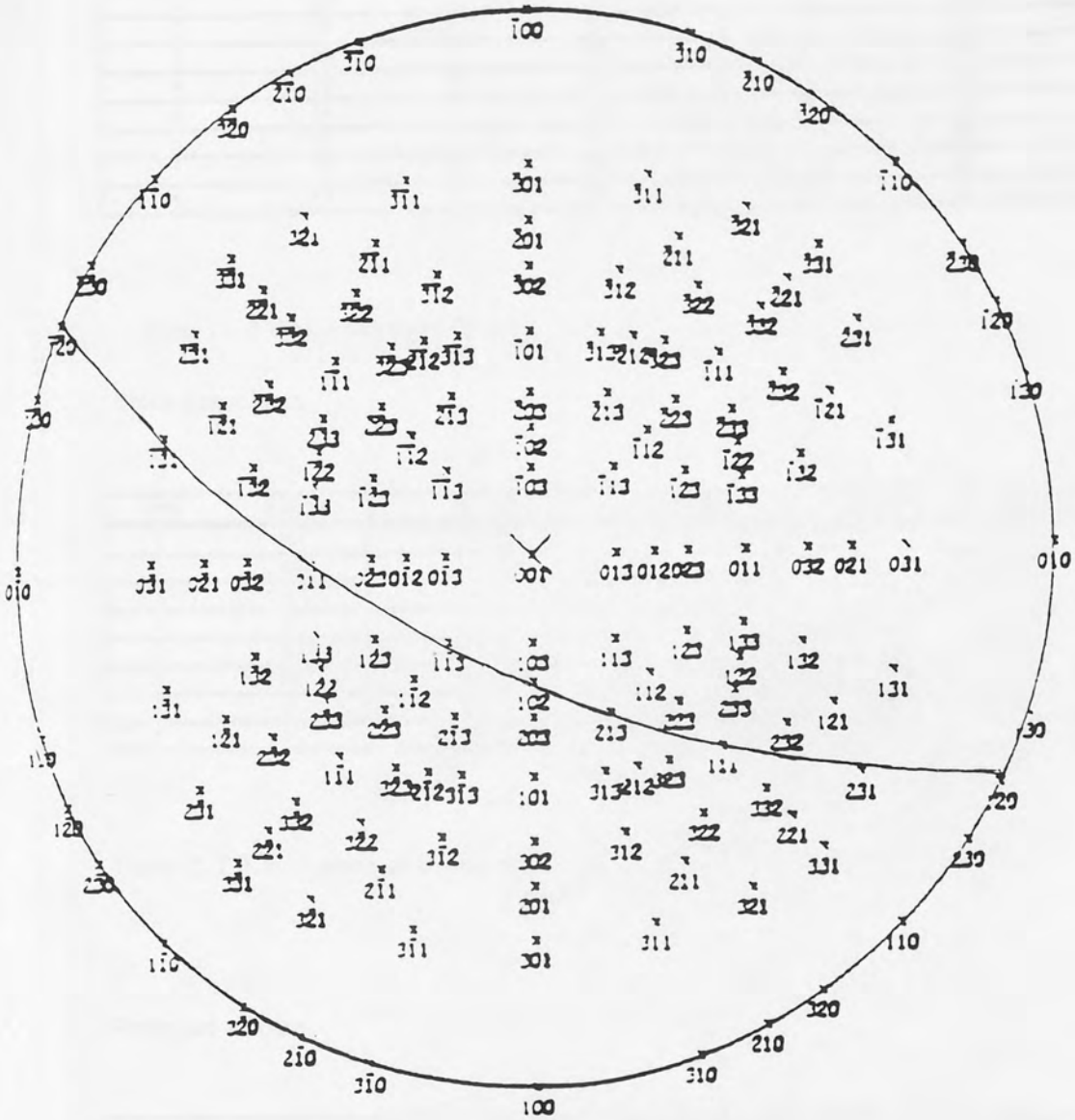

Figure 60 : Stereographic projection of Al

Probe size = 40nm

Area	Figure	Al wt%	Zn wt%
1	58	83.9	16.1
2	58	59	41
3	58	56	44
4	58	16	84
5	58	6	94
6	58	4	97
7	58	88	12
8	58	98	2

Table 11. T.E.M. Analysis of ZM11

Probe size = 30nm

Area	Figure	Al wt%	Zn wt%	Si wt%
1	67	19.5	80.4	0.1
2	67	0.4	99.5	0.1
3	67	0.4	99.5	0.1
4	67	6.3	93.6	0.1
5	67	20.6	79.3	0.1
6	68	61.4	38.5	0.1
7	//	61	38.7	0.1
8	//	78.1	21.8	0.1

Table 12. T.E.M. Analysis of Cosmal

Probe size = 30nm

Area	Figure	Al wt%	Zn wt%	Si wt%
1	75	64.8	33.6	1.6
2	75	79.4	19.4	1.2
3	75	74.3	21	4.7
4	79	5.9	2.4	91.7

Table 13. T.E.M. Analysis of Supercosmal

4.2.5 COSMAL

The as-cast structure of the Cosmal alloy is shown in Figures 61-63 at different magnifications. Cosmal contained much more aluminium than the previous alloys, so the amount of α' was much more and the amount of eutectic η less than for say ZA27H2. The structure of this alloy was heterogeneous and consisted of a few large dendrites and many smaller, rounded primary particles.

Figure 61 at low magnification shows α' dendrites set in β phase with little intermetallics. The dark particles were silicon, and again mostly associated with the aluminium-rich phases.

Figures 62 and 63a at higher magnifications show the Al-rich former α' phase surrounded by η and β phases. The figures also indicate a spinodal decomposition of the α', for the lamellae β stops when reaching the α' phase. Figure 63b at a different contrast showing more clearly that the advance of the β lamellae stops when reaching the α' phase. Further detailed investigations were carried out on the TEM.

A general structure of this alloy is shown in Figure 64, primary β particles in a zinc (η) matrix. Figure 65 at higher magnification shows decomposed β particles in the centre surrounded by α' phase. Figure 66 shows an interdendritic η region surrounded by eutectic β phase, tiny dark spots can be seen enclosed within the η-phase, these dark spots were difficult to analyse due to their small size. A diffraction pattern was taken from the zinc rich area and confirmed it to be zinc, this is shown in Figure 69. The diffraction pattern had a beam direction of $[10\bar{1}1]$. In order to understand the indexing more clearly a stereographic projection is shown in Figure 70 with the great circle on which the points lie shown clearly. Figure 67 shows on the right hand side an eutectic

η phase and on the left hand side a β phase. Analyses were made in the areas indicated in this figure and are shown in Table 12.

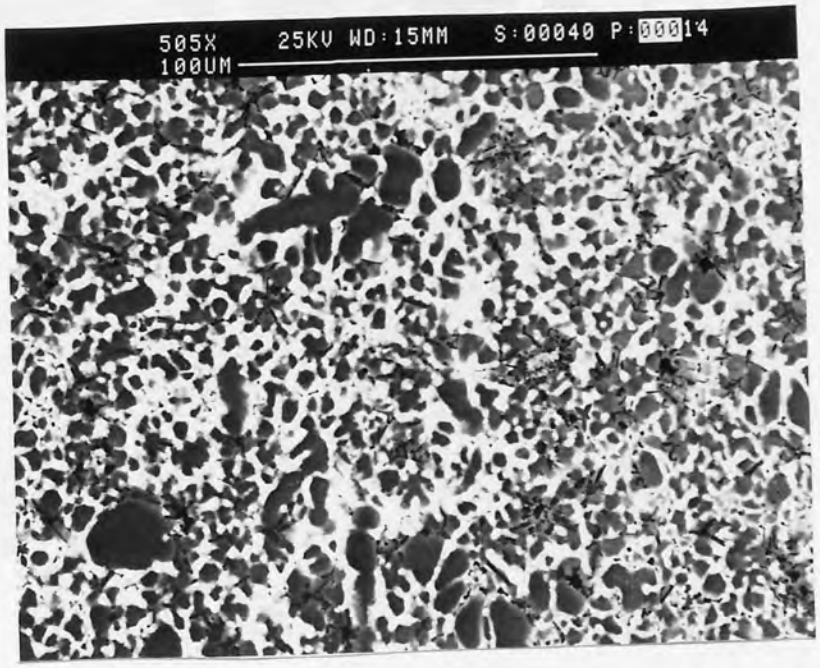

Figure 61: SEM as-cast structure of Cosmal showing α' dendrites with different sizes and shapes and a mixture of β and η, and a eutectic matrix of α + Si.

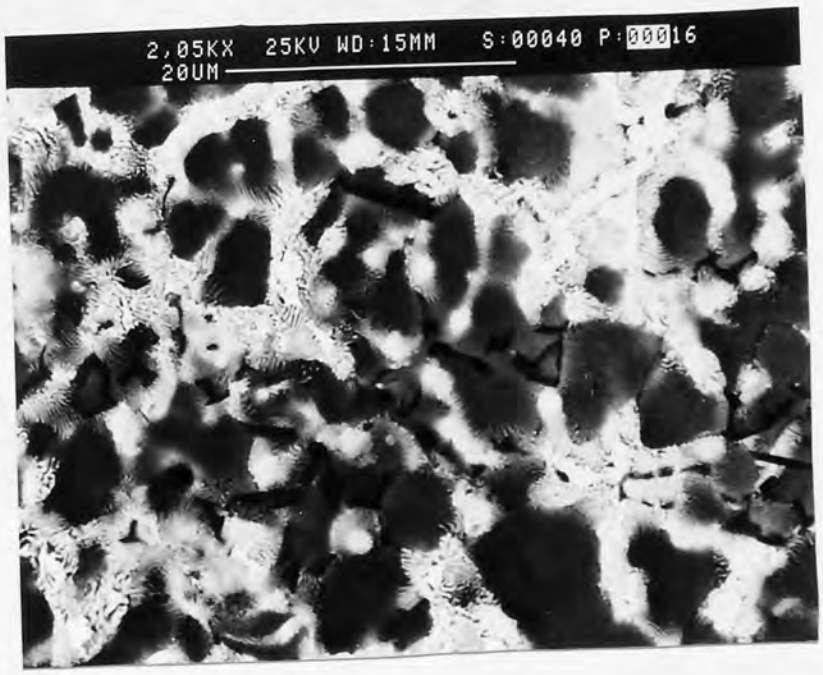

Figure 62: SEM as-cast structure of Cosmal showing aluminium-rich α' phase surrounded by spinodally decomposed β.

A

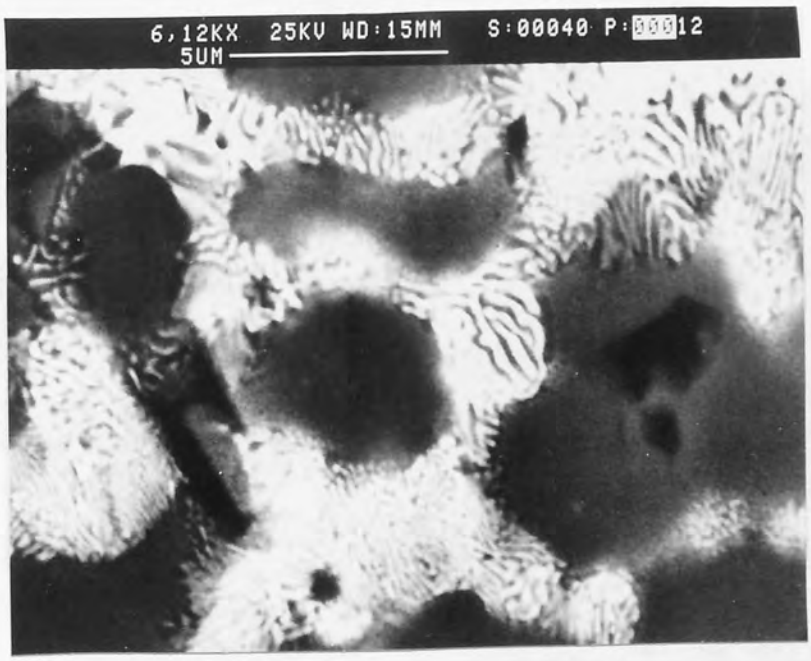

B

Figure 63: SEM as-cast structure of Cosmal showing a higher magnification and at two different contrasts to highlight that the lamellar decomposition of β stops when reaching the α' phase.

Figure 64: TEM as-cast structure of Cosmal alloy showing a zinc-rich area surrounded by spinodally decomposed β.

Figure 65: TEM as-cast structure of Cosmal showing decomposed β particles in the centre surrounded by α' phase

Figure 66: TEM as-cast structure of Cosmal showing an interdendritic η region in the centre surrounded by eutectic β phase. SADP taken from the arrowed area.

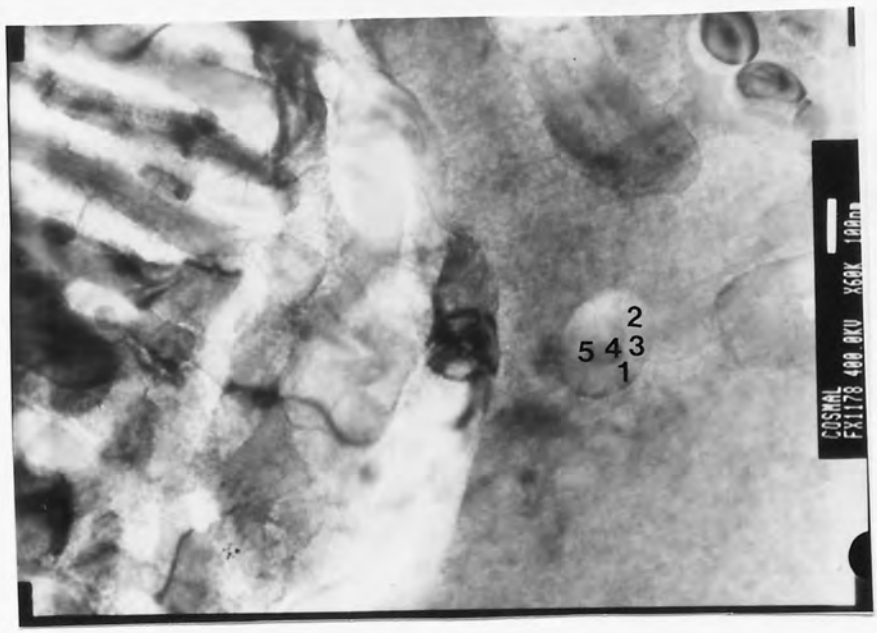

Figure 67: TEM as-cast structure of Cosmal showing on the right-hand side the eutectic η phase and on the left-hand side a decomposed β phase.(The numbers on this micrograph are the points of analyses).

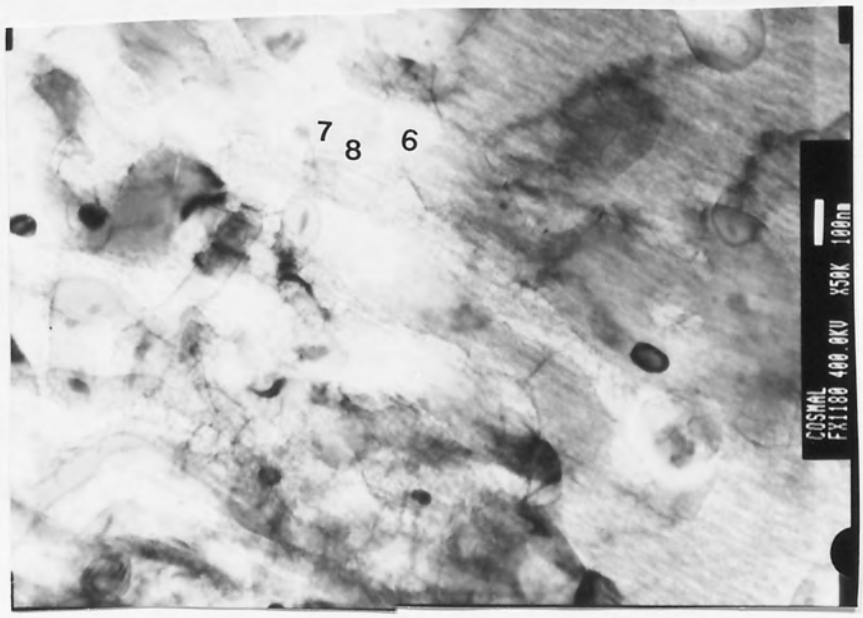

Figure 68: TEM as-cast structure of Cosmal showing decomposed β, also shown in this figure, are fine precipitates.(The numbers on this micrograph are the points of analyses).

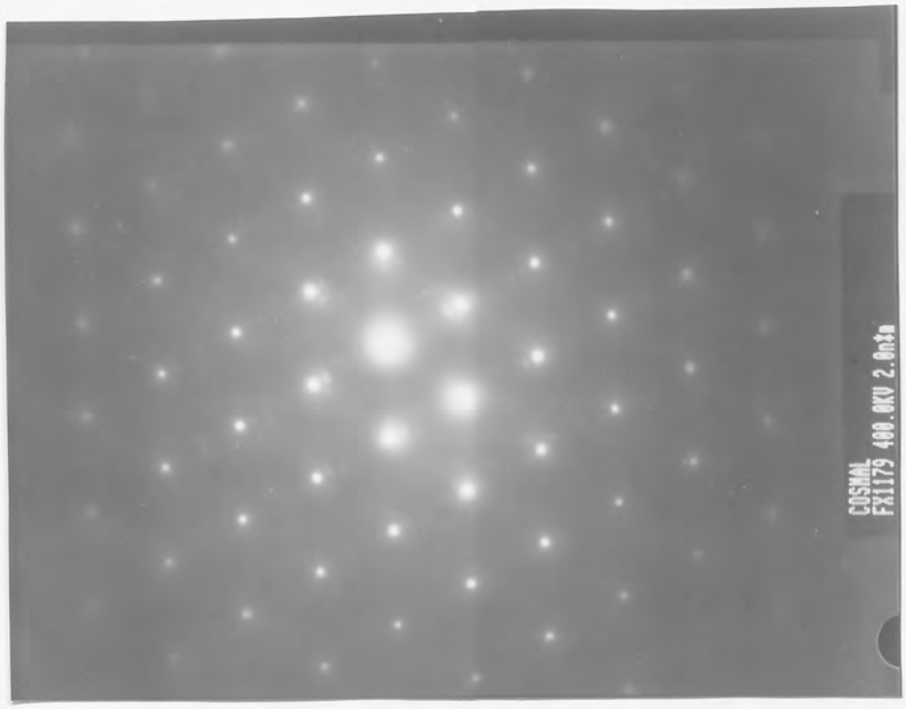

A

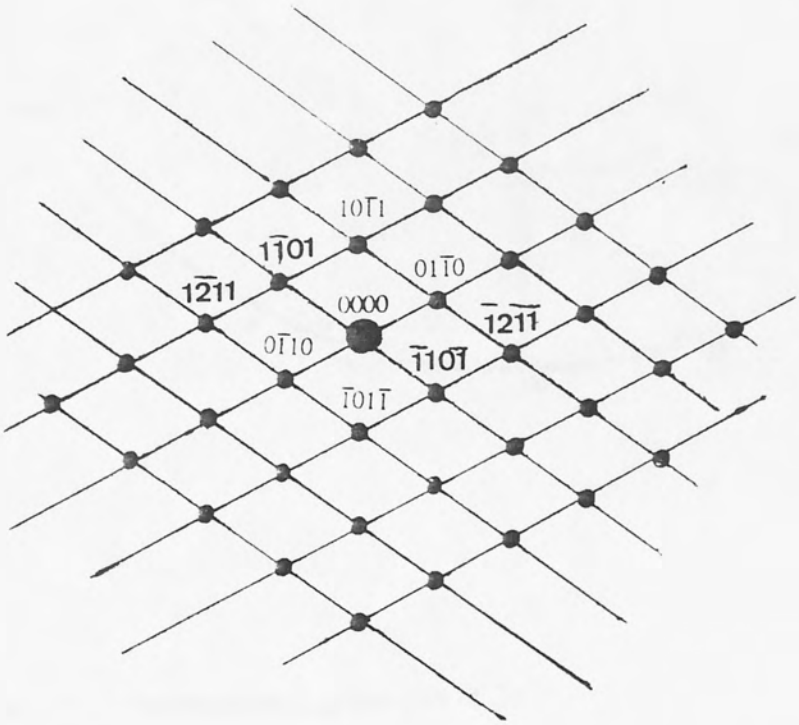

B

Figure 69: a) SADP taken from the arrowed area on Figure 66, showing a diffraction pattern withe a beam direction of $[\ 10\bar{1}\bar{1}\ ]\ \eta$.

b) Indexing of the above pattern.

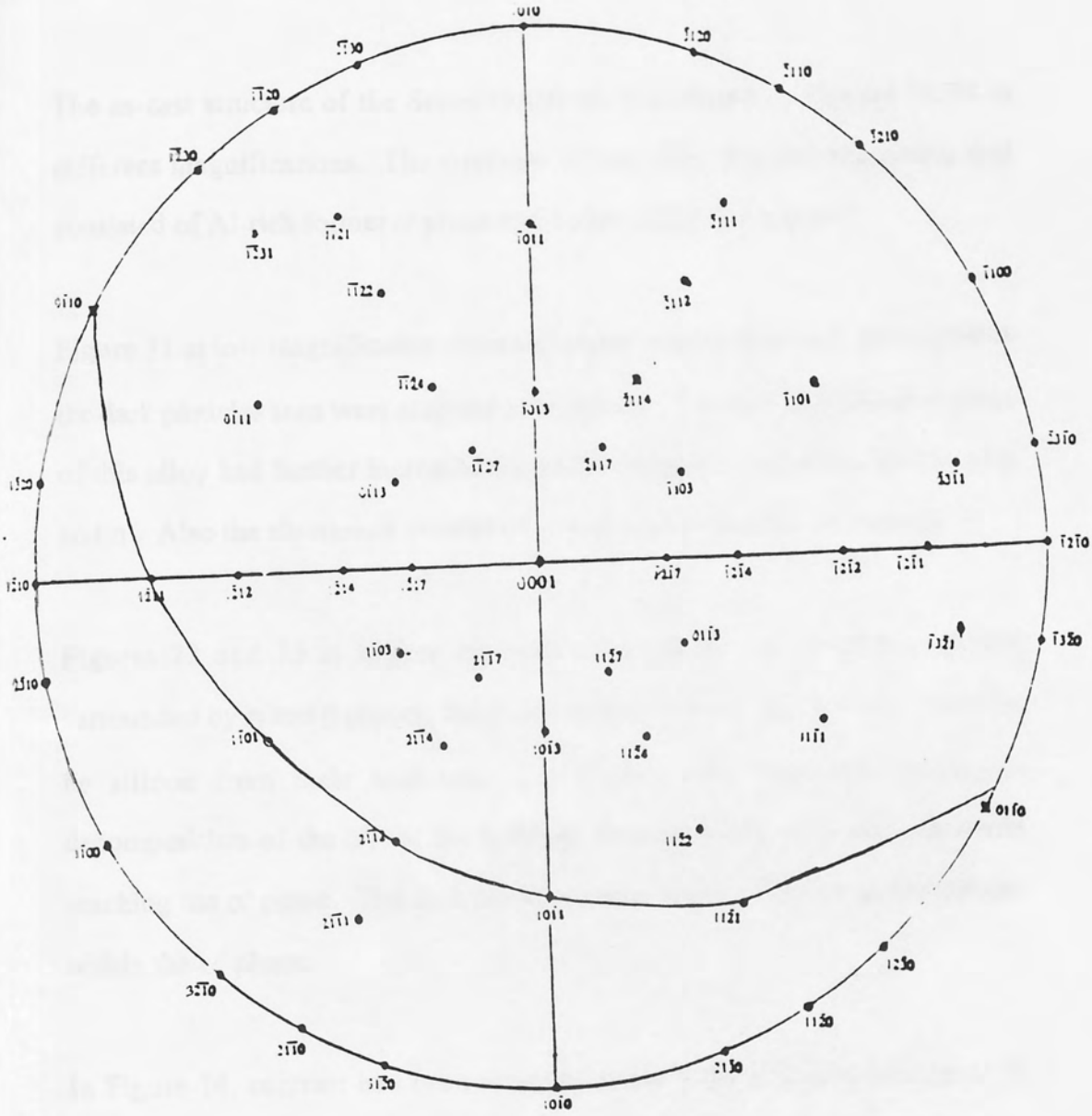

Figure 70 : Stereographic projection of Zn

4.2.6 SUPERCOSMAL

The as-cast structure of the Supercosmal alloy is shown in Figures 71-74 at different magnifications. The structure of this alloy was heterogeneous and consisted of Al-rich former α' phase and a zinc-rich β and η phase.

Figure 71 at low magnification shows α' phase and mixture of β and η phases the dark particles seen were analysed to be silicon. The high aluminium content of this alloy had further increased the proportion of α' and reduced that of β and η . Also the aluminium content of α' was higher than that of Cosmal.

Figures 72 and 73 at higher magnifications show the Al-rich α phase surrounded by η and β phases, the dark particles in these figures were found to be silicon from their analyses. The figure also suggested spinodal decomposition of the α', for the lamellar decomposition of β stopped when reaching the α' phase. The dark particles seem to have formed preferentially within the α' phase.

In Figure 74, contrast had been arranged to view the α' cores, in Figure 73 however the contrast had been arranged to allow the β region to be viewed .

Further investigation of this alloy were carried out on the TEM as shown in Figures 75-78.

Figure 75 shows apparent spinodal decomposition of α'-phase, also seen in this figure is a decomposed β particle. Quantitative analyses were made on the spinodally decomposed α' and are shown in Table 13. A SADP from the same area (arrowed) Figure 75, and it was found to be aluminium-rich area with a beam direction of [013]. The SADP is shown in Figure 79.

Figure 76 shows a former β particle which had decomposed into final products of lamellar and particulate mixture of phases. Figure 77 shows discontinuous decomposition of α' dendrite cores into a lamellar final product. Also seen in this figure is a Si-rich phase. Figure 78 highlights after tilting what is believed to be a Si-rich area in Figure 77. Analyses were made on this area and were found to contain an average of 94% Si this is shown in Table 13.

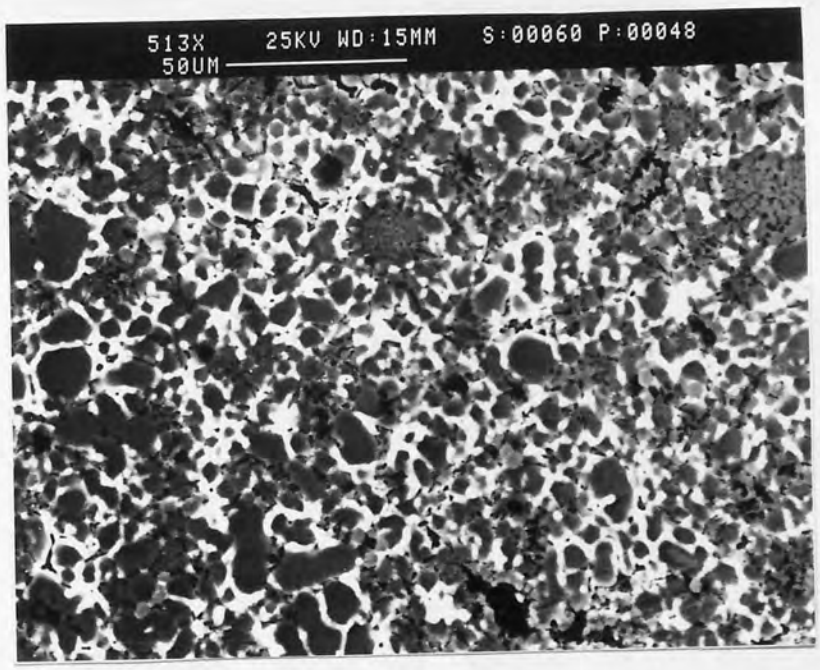

Figure 71: SEM as-cast structure of Supercosmal showing the α' phase and a mixture of β and η.

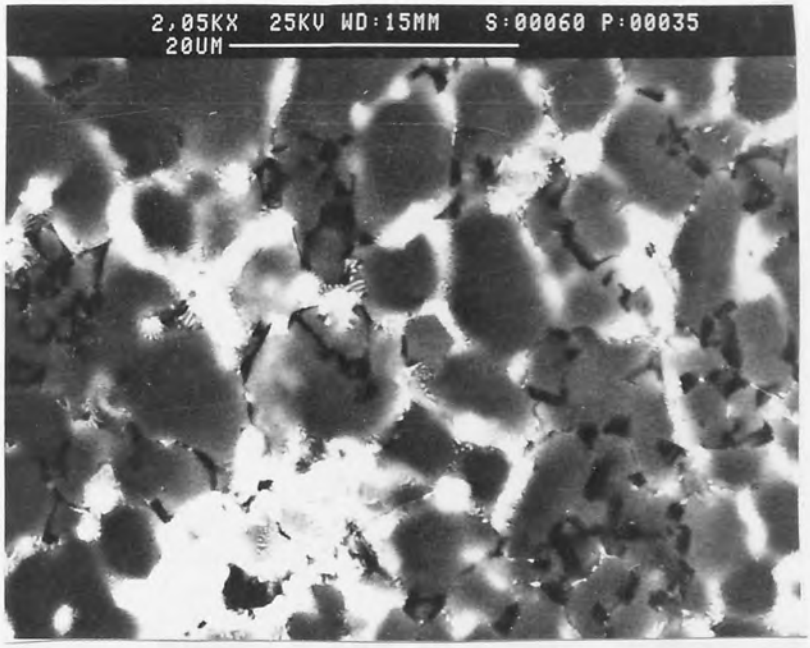

Figure 72: SEM as-cast structure of Supercosmal showing aluminum-rich α' phase surrounded by decomposed β, also seen are some silicon particles associated mainly with the α' phase.

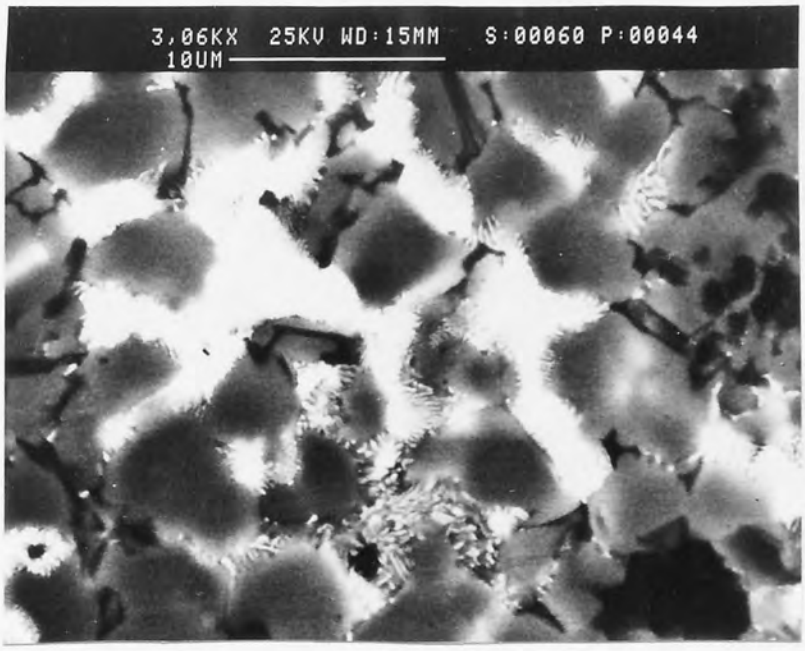

Figure 73: SEM as-cast structure of Supercosmal showing at higher magnification mottled contrast due to the decomposition of α' cores.

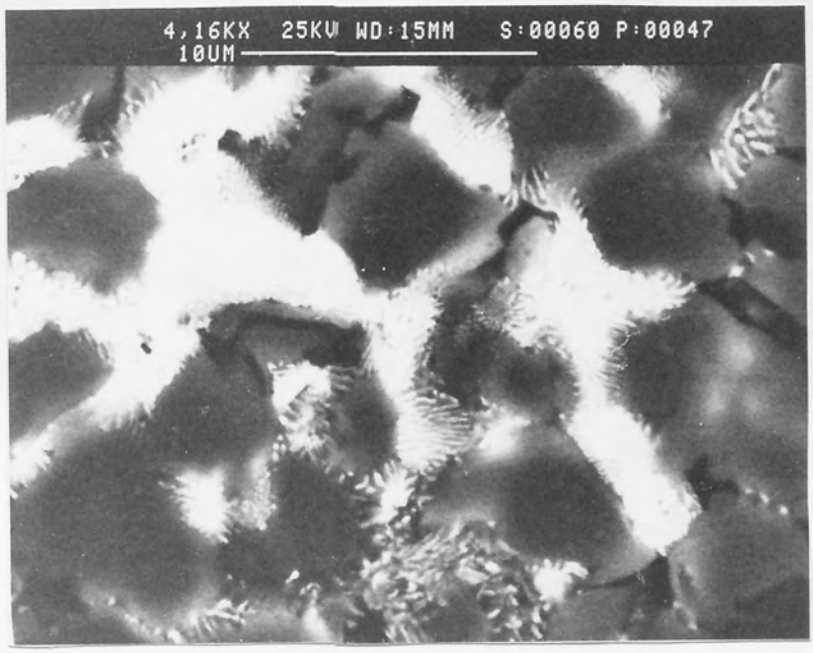

Figure 74: SEM as-cast structure of Supercosmal at higher magnification and different contrast to show lamellar decomposition of the β regions.

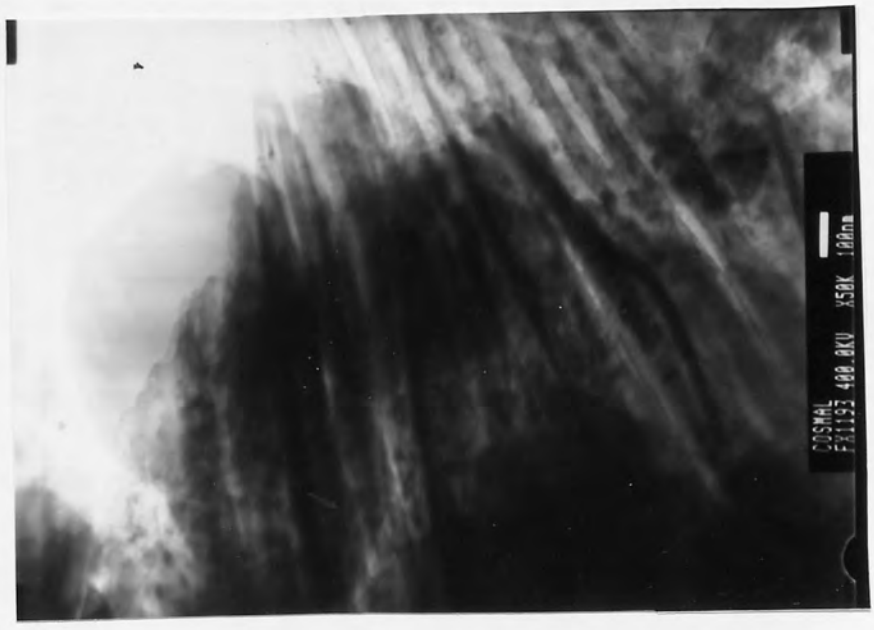

Figure 77: TEM as-cast structure of Supercosmal showing discontinuous decomposition of α' dendrite cores into a lamellar final product, also seen in this figure, a silicon rich particle.

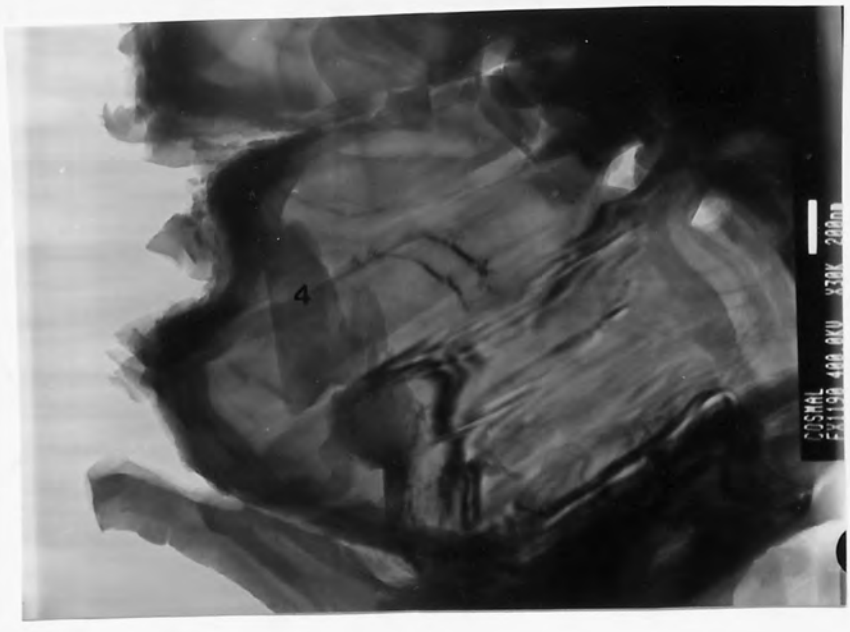

Figure 78: TEM as-cast structure of Supercosmal showing a Si-rich particle taken from Fig.77 after tilting the specimen to highlight the Si-rich area.(The number on this micrograph is the point of analyses).

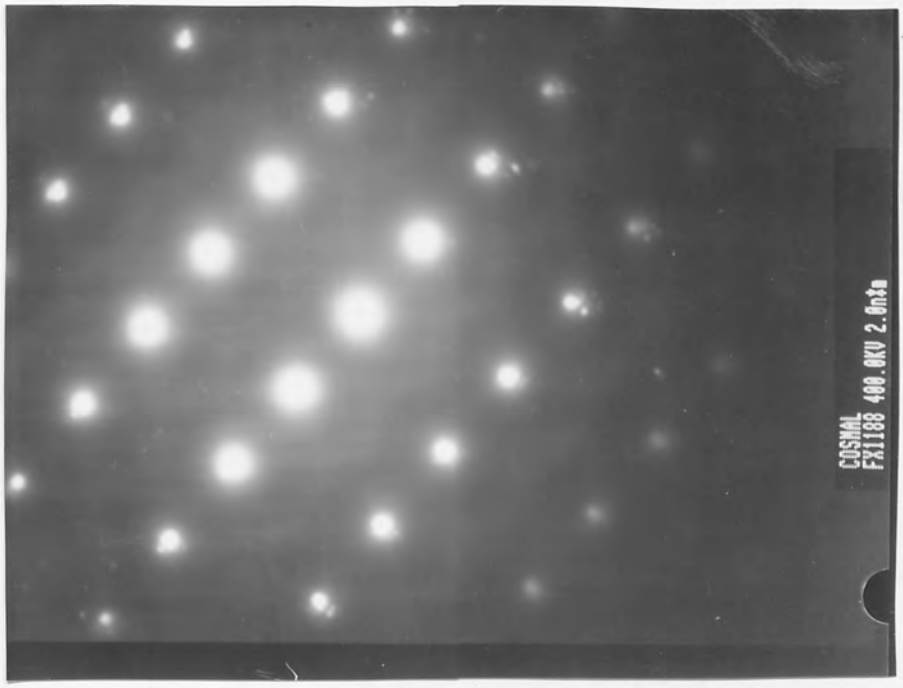

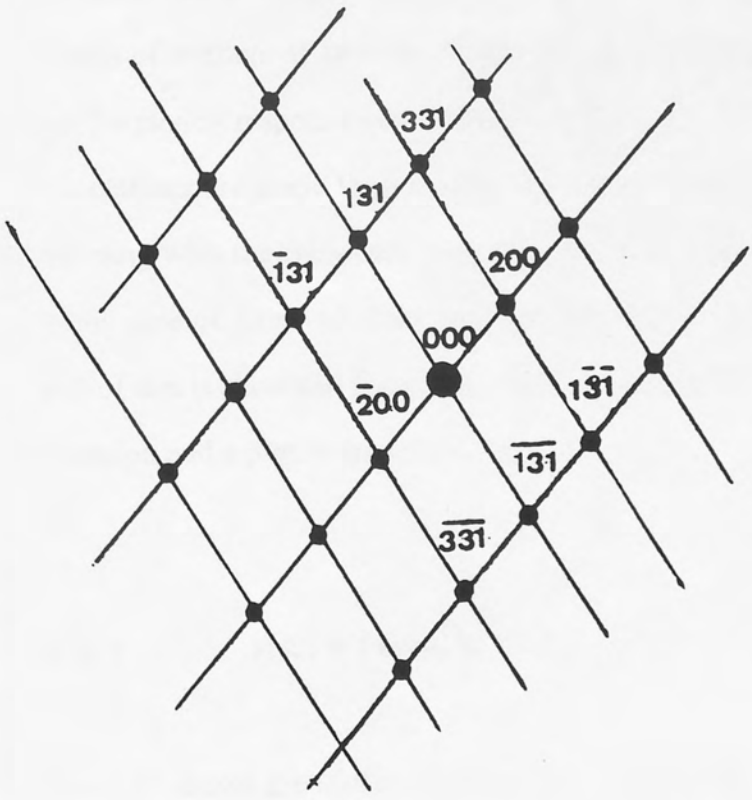

B

Figure 79 : a) SADP taken from the arrowed area on Figure 75. showing a diffraction pattern with a beam direction of [$0\bar{1}3$] α .

b) Indexing of the above pattern.

4.3 DAMPING RESULTS

Damping tests were carried out on the commercial alloys M3, ZA8, ZA27 and Cosmal alloy ZM11, Cosmal and Supercosmal and also ZA21H1 and ZA27H2. Tests were carried out using three different techniques.

4.3.1 MODAL ANALYSIS METHOD (Fitting a Nyquist diagram)

Table 14 shows the results obtained from the modal analysis method. The analyser was set to a frequency span of 0-800Hz, and, only one mode of vibration was excited. The values given for frequencies are indicated by the computer and are representative of the resonance frequencies, all readings are results of average of 10 tests. Figure 80 shows an example of the printout of the frequency response curve with only the first mode of vibration present; calculations are made from the curves. Tables 15 and 16 show the values for damping with the frequency span set to 0-1.6kHz and 0-3.2kHz respectively. In the case of Table 15, only the first two modes of vibration are present. A plot of this is shown in Figure 81. Table 16 represents the first three modes of vibration and a plot is shown in Figure 82.

4.3.2 HALF POWER POINT METHOD

Table 17 shows the results obtained from the half power point method. The first three modes of vibration were used, the values of resonance frequencies corresponding to each mode are also present. Figure 83 shows an example of

Alloy	Damping Q^{-1}	Frequency (Hz)
ZM11	0.0164	618
Cosmal	0.0178	442
S.Cosmal	0.0186	453
ZA27	0.0154	628
ZA8	0.0141	584
M3	0.0157	410

Table 14. Results obtained from modal analysis method.
frequency span of 800 Hz.

Alloy	Damping	Q^{-1}	Frequency(Hz)	
	1	2	1	2
ZM11	0.0285	0.0115	619	1543
Cosmal	0.0293	0.0122	443	1253
S.Cosmal	0.0313	0.0167	459	1303
ZA27	0.0266	0.0118	629	1564
ZA8	0.0246	0.012	596	1498
M3	0.0274	0.0106	412	1159

Table 15. Results obtained from modal analysis method.
frequevcy span of 1.6kHz

Alloy	Damping Q^{-1}			Freq.(Hz)		
	1	2	3	1	2	3
ZM11	0.0491	0.0212	0.0113	617	1545	2998
Cosmal	0.0518	0.0208	0.0129	445	1254	2490
S.Cosmal	0.0514	0.0213	0.0140	458	1302	2590
ZA27	0.0435	0.0231	0.0160	630	1565	2994
ZA8	0.0423	0.0213	0.0145	594	1489	2798
M3	0.0531	0.0201	0.0113	413	1154	2282

Table 16. Results obtained from modal analysis method.
frequency span 3.2 kHz

frequency response. Figure 84 shows one of the modes of vibration magnified to enable calculation.

Alloy	Damping Q^{-1}			Freq.(Hz)		
	1	2	3	1	2	3
ZM11	0.0468	0.0112	0.0041	440	1089	2176
Cosmal	0.0267	0.0094	0.0015	464	1149	2301
S.Cosmal	0.0514	0.0023	0.0014	472	1190	2418
ZA27	0.043	0.0098	0.0048	420	1059	2168
ZA8	0.0221	0.0041	0.0165	485	1319	2692
M3	0.0421	0.0062	0.0014	349	1055	2123

Table 17. Results obtained from the half power point method

TEMP. °C.	26	26	26
MASS . G	33.0302	33.1107	33.5308
FREQ.Hz	680	682	686
N 1	475	425	338
2	462	426	395
3	460	419	390
4	413	424	390
5	424	425	393
6	444	422	393
7	454	420	397
8	451	424	389
9	467	426	391
10	466	425	393
AVERAGE	450	424	392
Q	613.9	578.4	534.7
$Q^{-1} \times 10^{-3}$	**1.63**	**1.73**	**1.87**

Table 18. Results obtined from free decay method (ZM11)

4.3.3. FREE DECAY METHOD

Tables 18-25 are the results obtained from the free decay method. These results are obtained as shown from an average of 10 tests for each reading. Further tests were carried out at elevated temperatures are shown in Tables 26-33. This method of measurement considers the fundamental or the first mode of vibration.

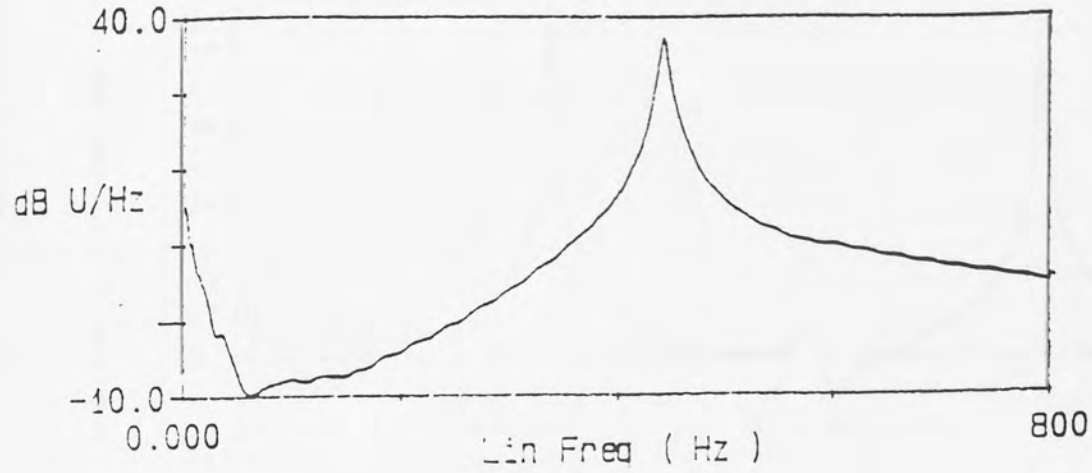

Figure 80 Frequency response curve showing the first mode of vibration.

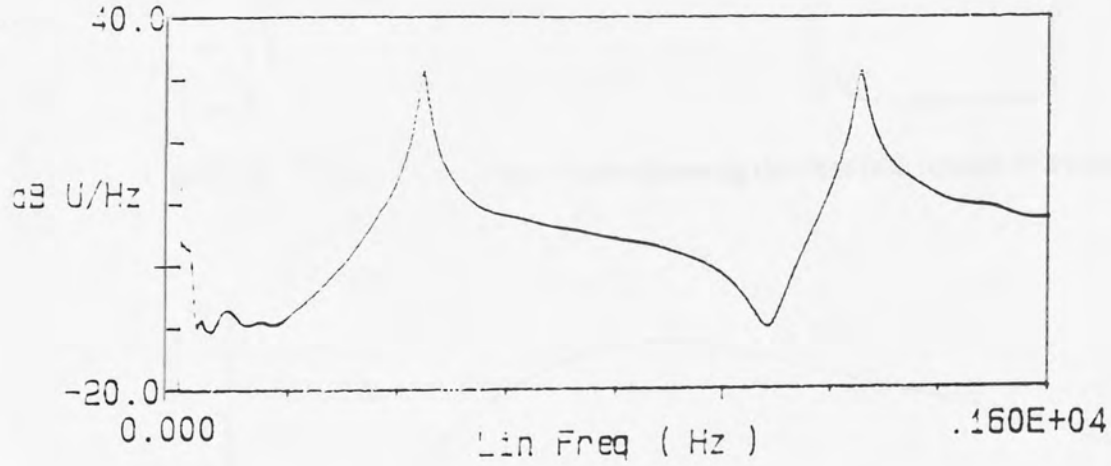

Figure 81 Frequency response curve showing the first two modes of vibration.

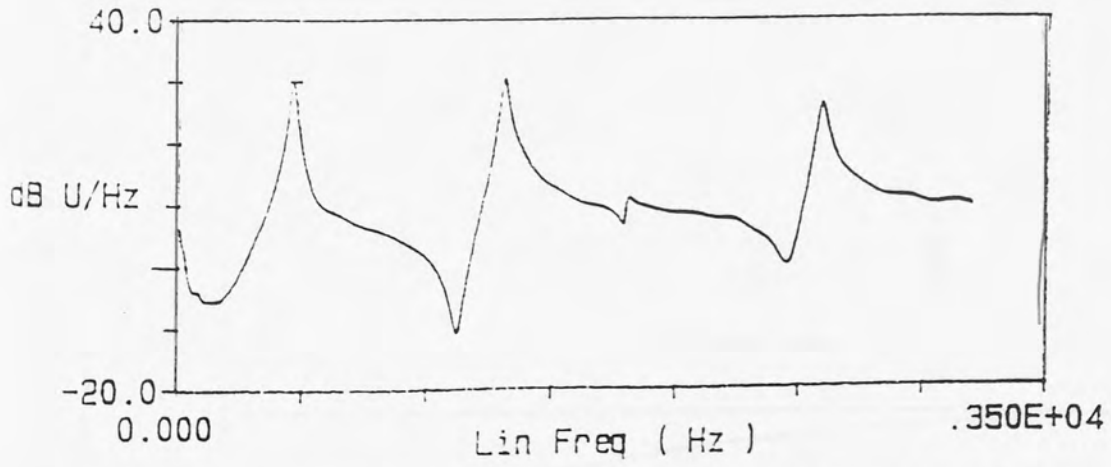

Figure 82 Frequency response curve showing the first three modes of vibration.

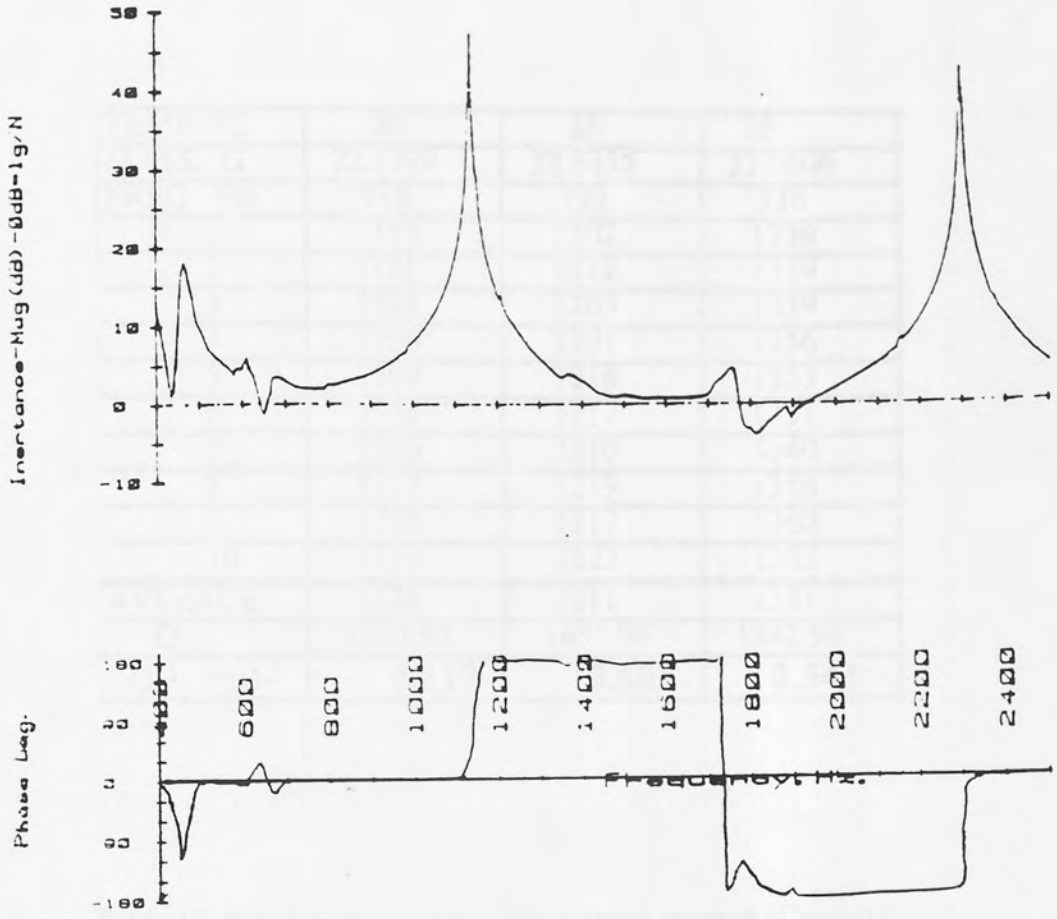

Figure 83 Frequency response curve showing the first two modes of vibration.

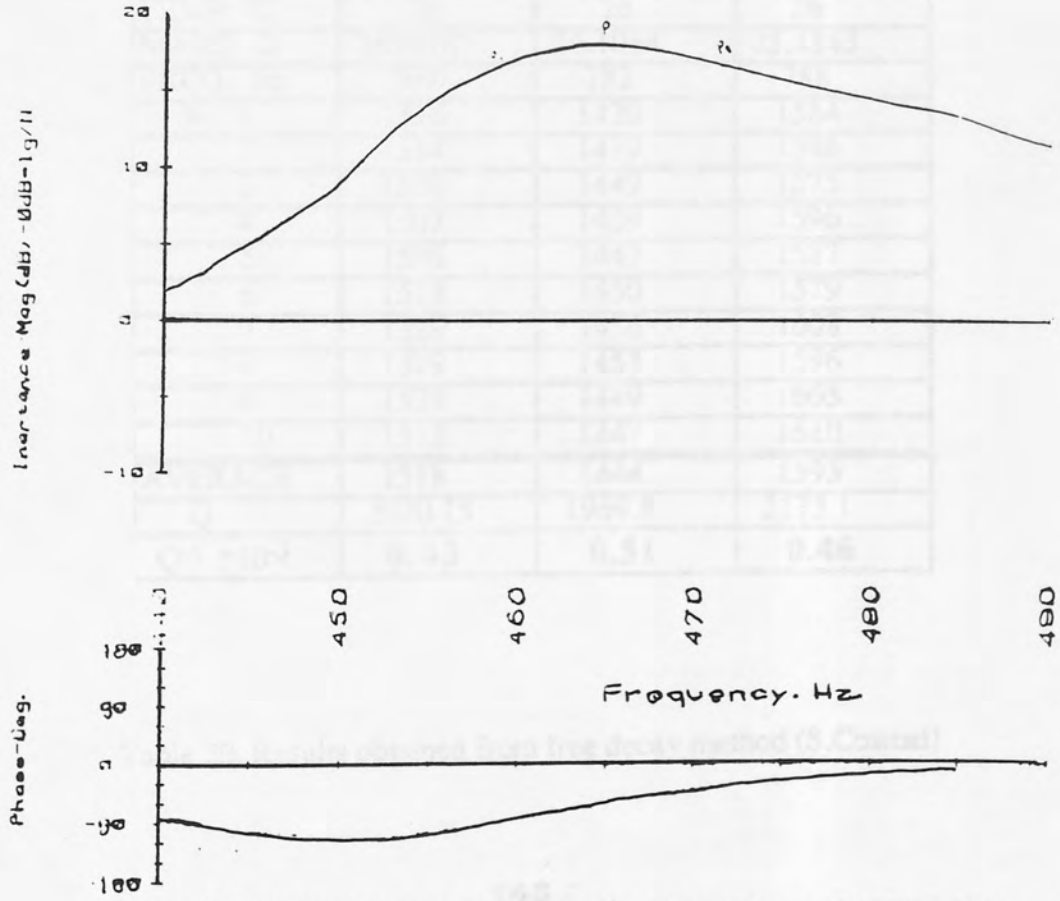

Figure 84 Frequency response curve showing the magnification of one of the

TEMP. °C.	26	26	26
MASS. G	22.1799	22.8835	23.0606
FREQ. Hz	718	722	726
N 1	1173	1202	1339
2	1181	1212	1339
3	1188	1203	1359
4	1180	1201	1356
5	1189	1216	1353
6	1184	1217	1351
7	1190	1210	1340
8	1187	1219	1356
9	1210	1212	1360
10	1119	1223	1362
AVERAGE	1188	1211	1351
Q	1620.59	1651.96	1842.94
Q^{-1} $*10^{-3}$	**0.617**	**0.605**	**0.543**

Table 19. Results obtained from free decay method (Cosmal)

TEMP. °C.	26	26	26
MASS. G	26.0767	26.1064	25.4543
FREQ. Hz	760	782	788
N 1	1516	1420	1584
2	1514	1439	1588
3	1530	1449	1575
4	1507	1439	1596
5	1505	1442	1587
6	1518	1450	1579
7	1529	1456	1608
8	1519	1453	1596
9	1528	1449	1605
10	1515	1447	1610
AVERAGE	1518	1444	1593
Q	2070.75	1969.8	2173.1
Q^{-1} $*10^{-3}$	**0.43**	**0.51**	**0.46**

Table 20. Results obtained from free decay method (S.Cosmal)

TEMP. °C.	26	26	26
MASS. G	33.2362	33.5517	33.2854
FREQ. Hz	692	694	690
N 1	1077	1127	1095
2	1069	1137	1091
3	1068	1145	1106
4	1078	1128	1106
5	1064	1150	1108
6	1067	1150	1102
7	1082	1150	1112
8	1077	1145	1117
9	1085	1139	1112
10	1087	1145	1116
AVERAGE	1075.4	1142	1107
Q	1466.98	1557.84	1510.1
Q^{-1} *10^{-3}	**0.682**	**0.652**	**0.662**

Table 21. Results obtained from free decay method (ZA27)

TEMP. °C.	26	26	26	26
MASS. G	32.0573	31.5785	32.0395	30.792
FREQ. Hz	682	686	676	672
N 1	362	386	386	431
2	364	389	389	427
3	362	390	388	426
4	363	392	388	432
5	361	389	389	432
6	376	390	387	429
7	363	391	391	430
8	365	391	388	433
9	367	391	389	436
10	363	393	394	434
AVERAGE	364	390	389	431
Q	496.54	532.01	530.65	578.9
Q^{-1} *10^{-3}	**2.01**	**1.88**	**1.88**	**1.7**

Table 22. Results obtained from free decay method (ZA27H1)

TEMP. °C.	26	26	26	26
MASS. G	29.4412	30.4115	29.8132	29.9598
FREQ. Hz	686	686	688	698
N 1	397	478	440	512
2	399	474	443	512
3	403	481	446	520
4	400	483	441	520
5	398	481	445	516
6	402	485	442	514
7	401	485	441	517
8	505	485	446	515
9	400	486	446	524
10	403	487	441	515
AVERAGE	411	483	443	517
Q	560.66	658.86	604.31	705.25
Q^{-1} *10^{-3}	**1.78**	**1.52**	**1.65**	**1.42**

Table 23. Results obtained from free decay method (ZA27H2)

TEMP. °C.	26	26	26
MASS. G	42.7172	42.6564	42.452
FREQ. Hz	656	660	658
N 1	1364	1387	1484
2	1362	1394	1496
3	1372	1402	1487
4	1377	1401	1494
5	1377	1404	1493
6	1366	1390	1493
7	1398	1408	1503
8	1387	1404	1503
9	1395	1414	1501
10	1394	1413	1501
AVERAGE	1379	1401	1495
Q	1881.14	1911.15	2039.37
Q^{-1} *10^{-3}	**0.532**	**0.523**	**0.49**

Table 24. Results obtained from free decay method (ZA8)

TEMP. °C.	26	26
MASS. G	45.1767	44.1092
FREQ. Hz	652	642
N 1	1397	1375
2	1397	1388
3	1401	1389
4	1395	1398
5	1401	1404
6	1410	1406
7	1411	1403
8	1412	1409
9	1420	1409
10	1418	1409
AVERAGE	1406	1399
Q	1917.97	1908.42
Q^{-1} *10^{-3}	**0.521**	**0.524**

Table 25. Results obtained from free decay method (M3)

TEMP. °C.	50	40	30
MASS.G	33.1107	33.1107	33.1107
FREQ. Hz	~	~	681
N 1	124	256	346
2	127	255	347
3	145	261	350
4	142	257	354
5	152	262	347
6	152	266	349
7	167	264	347
8	172	263	351
9	161	260	345
10	169	267	345
AVERAGE	151	261	349
Q	205.9	356.2	476.1
Q^{-1} *10^{-3}	**4.86**	**2.81**	**2.1**

Table 26. Results obtained from free decay method at elevated temperatures (ZM11)

TEMP. C	80	70	60	50	40	30
MASS. G	22.8835	22.8835	22.8835	22.8835	22.8835	22.8835
FREQ. Hz	~	~	702	720	722	722
N 1	231	320	460	617	774	1006
2	239	319	462	617	769	1032
3	241	332	453	654	782	1031
4	246	337	503	627	786	1042
5	248	340	475	631	790	1046
6	250	337	489	649	805	1051
7	260	341	487	639	801	1052
8	264	349	497	642	817	1056
9	264	356	500	646	811	1071
10	273	385	503	667	837	1066
AVERAGE	256	342	483	639	797	1045
Q	343.76	466.53	658.87	871.68	1087.2	1425.52
$Q^{-1} * 10^{-3}$	**2.91**	**2.14**	**1.52**	**1.147**	**0.92**	**0.705**

Table 27. Results obtained from free decay method at elevated temperatures (Cosmal)

TEMP. C	90	80	70	60	50	40	30
MASS. G	26.076	26.076	26.076	26.076	26.076	26.076	26.076
FREQ. Hz	736	750	754	754	756	760	760
N 1	338	442	550	691	825	1052	1289
2	343	456	572	709	845	1056	1265
3	347	459	568	699	847	1050	1304
4	354	467	580	727	851	1068	1312
5	362	472	578	723	860	1077	1282
6	360	478	592	730	863	1075	1288
7	358	481	594	744	874	1074	1322
8	367	489	599	741	881	1094	1325
9	377	502	619	756	879	1082	1317
10	381	509	619	756	893	1101	1275
AVERAGE	359	475	583	728	862	1073	1298
Q	489.7	647.96	795.29	993.11	1126.8	1463.7	1770.6
$Q^{-1} * 10^{-3}$	**2.04**	**1.54**	**1.26**	**1.007**	**0.89**	**0.68**	**0.565**

Table 28. Results obtained from free decay method at elevated temperatures (S.Cosmal)

TEMP. °C.	50	40	30
MASS. G	33.2362	33.2362	33.2362
FREQ. Hz	688	690	692
N 1	406	582	820
2	413	590	811
3	421	600	805
4	429	608	812
5	430	599	825
6	432	611	819
7	446	615	830
8	450	625	836
9	451	629	837
10	456	627	839
AVERAGE	433	609	823
Q	590.67	830.75	1122.68
Q^{-1} *10^{-3}	**1.693**	**1.203**	**0.89**

Table 29. Results obtained from free decay method at elevated temperatures (ZA27)

TEMP. °C.	70	60	50	40	30
MASS. G	31.5785	31.5785	31.5785	31.5785	31.5785
FREQ. Hz	~	~	~	~	620
N 1	86	107	142	188	258
2	90	107	139	192	260
3	88	110	144	191	257
4	93	112	143	190	258
5	93	113	145	192	259
6	97	109	147	193	260
7	90	114	146	195	261
8	94	114	154	198	268
9	105	114	151	197	260
10	93	114	152	201	265
AVERAGE	93	111	146	194	261
Q	126.86	151.42	199.16	264.64	356.04
Q^{-1} *10^{-3}	**7.88**	**6.6**	**5.02**	**3.78**	**2.81**

Table 30. Results obtained from free decay method at elevated temperatures (ZA27H1)

TEMP. °C.	70	60	50	40	30
MASS. G	29.8132	29.8132	29.8132	29.8132	29.8132
FREQ. Hz	~	~	~	~	~
N 1	97	130	176	225	310
2	99	131	177	227	310
3	100	130	174	227	313
4	101	131	180	228	311
5	103	132	180	228	312
6	103	133	179	229	312
7	101	131	181	235	314
8	104	137	184	234	320
9	106	135	182	231	315
10	108	139	185	233	320
AVERAGE	102	133	181	230	314
Q	139.14	181.43	246.91	313.75	428.33
Q^{-1} $*10^{-3}$	**7.19**	**5.51**	**4.05**	**3.19**	**2.33**

Table 31. Results obtained from free decay method at elevated temperatures (ZA27H2)

TEMP. °C.	60	50	40	30
MASS. G	42.6564	42.6564	42.6564	42.6564
FREQ. Hz	656	656	660	660
N 1	434	583	826	1120
2	444	593	836	1128
3	440	607	845	1118
4	456	602	846	1109
5	459	607	843	1138
6	468	628	857	1144
7	476	630	886	1137
8	489	632	890	1147
9	482	644	893	1158
10	501	643	897	1152
AVERAGE	465	617	862	1135
Q	634.32	841.67	1175.88	1548.29
Q^{-1} $*10^{-3}$	**1.576**	**1.19**	**0.85**	**0.65**

Table 32. Results obtained from free decay method at elevated temperatures (ZA8)

TEMP. °C.	60	50	40	30
MASS. G	45.1767	45.1767	45.1767	45.1767
FREQ. Hz	646	648	648	650
N 1	425	641	830	1145
2	435	655	831	1154
3	436	659	836	1152
4	444	662	837	1153
5	445	666	834	1166
6	451	670	852	1172
7	457	667	853	1168
8	465	685	873	1176
9	472	683	871	1171
10	473	689	875	1177
AVERAGE	450	668	849	1163
Q	613.86	911.24	1158.15	1586.48
$Q^{-1} *10^{-3}$	**1.629**	**1.097**	**0.863**	**0.63**

Table 33. Results obtained from free decay method at elevated temperatures (ZM3)

4.4 TENSILE TEST RESULTS

Room temperature and elevated temperature tensile tests were carried out on all alloys, and the results are shown in Tables 34 and 35 respectively. Temperatures of 50, 75 and 100° C were used for the high temperature tests. The 0.2% proof stress of these alloys is also shown in these tables.

4.5 HARDNESS TEST

Hardness tests were carried out on all alloys at room temperature using the Vickers hardness test method with a load of 10 kgf the results are shown in Table 36.

Alloy	Hardness HV
ZM11	104
Cosmal	133
S.Cosmal	162
ZA27	139
ZA27H1	75
ZA27H2	109
ZA8	113
M3	89

Table 36. Vicker hardness test results (10Kgf Load)

Alloy	U.T.S. (MPa)	0.2 % P.S (MPa)
ZM11	247	203
Cosmal	269	233
S.Cosmal	365	320
ZA27	360	316
ZA27H1	247	206
ZA27H2	259	233
ZA8	316	264
M3	270	213

Table 34. Tensile test results for all alloys

Alloy	U.T.S. (MPa)		
	100°C	75°C	50°C
ZM11	121	160	223
Cosmal	127	163	229
S.Cosmal	259	287	320
ZA27	158	199	288
ZA27H1	145	205	235
ZA27H2	166	181	226
ZA8	146	211	271
M3	137	206	266

Table 35. U.T.S of all alloys at different temperatures

CHAPTER 5

5.0 DISCUSSION OF THE EXPERIMENTAL RESULTS :

5.1 Metallography of M3

The structure of the alloy was heterogeneous, but clearly hypoeutectic, and consisted of a few large (about 15 μm) and many small (about 8 μm) primary Zn-rich (η) dendrites surrounded by a relatively small volume of eutectic matrix. A few small round dark particles of Al-rich former β phase was also associated with the η particles. Figure 36 taken at medium magnification, showed (at bottom right hand corner) that these dark particles were a pseudoprimary aluminium-rich β phase which had formed on the primary phase at high undercooling during solidification of the eutectic. β is unstable below 275° C (eutectoid temperature), and decomposes into zinc-rich η and aluminium-rich α phase. Figure 36 shows that β in both the particles and the large portion of the β constituent of the lamellar matrix were clearly decomposed.

The solid solubility of aluminium in zinc is very little at room temperature and excess aluminium is removed by precipitation of the aluminium-rich phase (α) in zinc matrix.

In addition to the small dark Al-rich former β particles associated with the primary η particles (Figures 34 and 35), thin haloes of eutectic aluminium-rich phase (α) can be seen. These were probably due to the process of removing the excess aluminium from the super-cooled liquid before normal eutectic solidification took place. Upon subsequent

cooling, this had transformed into a string of $\alpha+\eta$ particles. The eutectic firstly grew asymmetrically to form irregular ribbon-like lamellae, which had acted as nuclei for further growth of irregular lamellae in a complex three-dimensional morphology. On cooling through the β-transformation, the lamellae had transformed into strings of α particles; the zinc portion of the eutectoid adding to the matrix phase.

5.2 Metallography of ZA8

In this alloy the primary phase was β of different sizes and shapes with an average size of 5 μm (figure 37) this was due to the method of casting used to produce this alloy. Eutectic pools were seen surrounding the primary β particles, so that the general structure of ZA8 was very similar to that of alloy M3, but the primary β particles replaced primary η particles and saller and were more uniformly distributed.

Figures 38 and 39 show that ZA8 is a hypereutectic alloy,present also in this alloy, but less frequently in addition to the primary β, were η phase particles with similar sizes and shapes to the primary β. These η particles were formed in highly supersaturated zinc-rich liquid at temperatures below the eutectic temperature during rapid cooling of the castings. In some cases, the eutectic η can be seen as haloes around the β dendrites as shown in Figures 40 and 41 taken at different magnifications. These were much thicker than those of β around the primaries in the alloy M3. One of the hypothesis to explain this phenomena was due to the higher under-cooling applied to ZA8 from the melt, the casting temperature of ZA8 is theoretically higher than that of M3, but in practice the casting temperatures of both alloys are about the same. Therefore, an alternative

hypothesis to explain this phenomenon can be explained by the amount of aluminium present in the M3 and ZA8.

Decomposition of β particles showed two distinct morphologies, a well developed lamellar form usually in the central portion of the grains, surrounded by a rim of a coarser mixture of the phases. Recent work carried out at Aston (108) on the decomposition of β, showed that although both α and η lamellae from the decomposed β were generally in equilibrium, some dark metastable particles were formed within the α lamellae. This investigation revealed that the metastable phases in the aluminium-rich α matrix had a higher aluminium content of about 22.7% than the α' found in the eutectic α. Furthermore, the copper content was lower by about 0.5% to 1.5%. This is in accordance with the metastable extension of the binary Zn-Al system, but was bounded by the extension of (α+α') region to low temperature. Therefore, the metastable phase here is an analogue, not of the β phase but of α' phase, due to the more aluminium-enriched nature of the primary particles than the eutectic β. This may also explain the lower copper content of the latter phase since the β phase dissolves more copper than the α phase at high temperatures (115).

In view of these evidences, it is believed that decomposition of β in this alloy involves two different transformation schemes, depending on the ratio of zinc-aluminium content it contains. Upon rapid cooling, solidification firstly occurs with considerable undercooling followed by retention of the high temperature β phase to low temperatures at which decomposition takes place. At low temperatures the diffusion rates are very small and probably the cellular decomposition would not be the same. In the case of aluminium-rich cores of the primary β, it is suggested

that a lamellar or sub-lamellar product of η and transitional aluminium-rich metastable α'_T was formed, due to the difficulty of reducing the zinc contents of the aluminium-rich plates to that of α in one step. α'_T and α are crystallographically identical and differ only in chemical composition and thus lattice parameter and α'_T is known to persist for a substantial time on low temperature aging (116-118). Therefore, the η plates of the eutectic mixture would be very thin due to the fact that α'_T contains more zinc than α.

In the case of the β lamellae or particles forming part of the eutectic, the process is practically the same. But because of the higher zinc content of the β in this case, however, the metastable phase formed in the cellular decomposition reaction would be the lower aluminium metastable phase indicated by extension of (α + β) phase field to lower temperatures, resulting in the decomposition of β into η plus another higher aluminium version of β, metastable at the transformation temperature.

5.3 Metallography of ZA27

ZA27 in comparison to the previous two alloys (M3 and ZA8) has a higher aluminium and copper content, thus a more complex multi-phase microstructure. The as-cast structure of ZA27 was shown to consist of a fine structure of dendrites in a mass of much smaller aluminium-rich particles and some pools of eutectic zinc. The average size of the α particles was about 12 μm, and because of the very small volumes of eutectic liquid, a regular eutectic such as that seen in M3 and ZA8 was not formed. Instead, a pool of eutectic zinc occupied the interdendritic spaces and the α phase joined the α' phases from the decomposed β of the

dendrites. Figures 44 and 45 at higher magnification show that the solidification of this alloy had begun with the formation of aluminium-rich ($\alpha+\alpha'$) dendrites, and was followed by precipitation of much more zinc-rich β-phase. The zinc-rich β-phase formed around the primary dendrites through a peritectic reaction between the first formed α- phase and residual liquid, and there was an obvious commonest change at the boundaries. However there was no great boundary at this point as the new phase (β) had the same crystal structure as the α', with only a small change in lattice parameters. Some cores had decomposed into a coarse lamellar product but the majority decomposed into a very fine mixture of zinc-rich phases in an aluminium matrix. The β areas subsequently decomposed into lamellar or irregular particles of α and η with eutectic pools occupying the remaining interdendritic areas.

However, Durman (108) showed that copper had precipitated as ε-phase with the η phase of the eutectic and the β transformation products had two distinct morphologies:

Firstly a high density of heterogeneously precipitated ε-phase particles was found in both the eutectic and η from lamellarly-decomposed β. These areas also showed higher than average copper contents. This indicates that copper was preferentially dissolved in the available η in both the eutectic matrix and the decomposed β.

Secondly discrete ε-particles of irregular sizes were also found, distributed irregularly in the interdendritic channels. Durman studied this form of ε-phase and proved that those phases had the C.P.H. structure of the ε-phase. Because of lack of time and the fact that this work had

already been carried out at Aston the present author did not carry out TEM examination of this alloy.

The decomposition of β-phase is very similar to that of ZA 8. The wide freezing range of this alloy makes it prone to microshrinkage and compared to the two previous alloys was the only alloy which contained appreciable amount of interdendritic porosity on casting.

5.4 Metallography of ZA27H1 and ZA27H2

As mentioned earlier, these alloys were based on ZA27 with variations of copper content and the addition of silicon in the case of ZA27H2 to study their effects on damping properties, U.T.S and hardness of the alloys.

The structures of these alloys were very similar to ZA27. In the case of ZA27H1 the presence of some rod-like intermetallic particles was apparent. However, in the case of ZA27H2 the major difference to ZA27 was the presence of some small dark silicon particles.

5.5 Metallography of ZM11

The structure of this alloy was heterogeneous in that it contained a few large dendrites and many smaller primary particles and was clearly hypereutectoid. At low magnification in Figure 51 the structure of the alloy consisted of fine former α' dendrites in a mixture of transformed β and eutectic η. At higher magnification in Figure 52, the alloy consisted of a coarse mixture of α+η with broad β rims set in an interdendrite matrix consisting largely of zinc. This suggests that on cooling after

casting, the supersaturated α cores had decomposed by precipitation of small zinc particles, and the β phase had formed a fine lamellar decomposition product. Silicon has an effect of reducing the proportions of former α and zinc-eutectic phases as well as introducing some discrete silicon particles as shown in Figure 53. Silicon was evidently the first material to crystallise from the melt on cooling and had served as a nucleus for the alpha dendrites which appeared next. Figure 54 at high magnification showed nicely formed patterns of cellular decomposition in α and β. The cells were nucleated on the η and thickened as they grew into the α' phase. Various stages of cellular decomposition are as follows: cells are nucleated by the occurrence of grain boundary allotriomorphs, which indicates the onset of cellular decomposition. During the migration of grain boundary, a narrow region behind the boundary gets depleted of solute elements by diffusion to the allotriomorphs formed concurrently. After nucleation, the cellular products grew to a produce lamellar structure which developed from the grain boundary allotriomorphs and grew into the parent grain as shown in Figure 54. The growth of cells was believed to be due to the continued migration of the boundary. As the lamellae grew, they continued to coarsen as they grew into the α' phase.

The TEM micrograph in Figure 55 and 56 illustrate a typical complex structure of decomposed α dendrites branching out from the centre of the micrograph (Figure 55). This micrograph was taken from an area similar to that shown in Figure 54. Figure 56 which was also taken from a similar area to that of Figure 54, shows the dendrite arm are parallel to each other, also present are cellular precipitates of different sizes and shapes. The irregular mats of dark particles are oxides formed during electro polishing. As shown in both the SEM and TEM micrographs α

and β had decomposed cellularly. Therefore, it is a reasonable assumption that cell nucleation and growth is one of the most important modes of decomposition in this alloy. Upon solidification after the cellular reaction was completed, the alloy entered into the GP zone region and then decomposed into first transitional phase α''_m in equilibrium with the matrix phase α". Finally α_m and η formed by continuous precipitation. Figure 57 shows one such precipitate which was analysed and was found to be α_m phase.

A number of SADP's were taken from different regions of Figure 57; one example of these diffraction patterns is shown in Figure 59 which corresponded to a beam direction of $[2\bar{1}\bar{1}]$ of the FCC α matrix. This figure also shows the points indexed and in order to clarify the figure, a stereographic projection was established and the great circle on which the points of index lie is clearly shown (Figure 60).

Table 11 shows the results of some analyses carried out on points marked on Figure 58, which shows the weight % of aluminium and zinc at eight different points, none of which is consistent with the decomposition of the alloy. The aluminium content of a α region was found to be in the case of analysis number 8 up to 98% . On the other hand η regions (5&6) showed high zinc contents of up to 97%. There are possibilities of errors occurring during the analysis, i.e. an error could have occured by the background fitting process to the characteristic peaks of the elements.

5.6 Metallography of the Cosmal alloy

Cosmal contained a larger volume of aluminium than the previously discussed alloys. Therefore, the amount of α' was much more, this is

clearly demonstrated in Figure 61 which shows the α' dendrites set in β phase with little intermetallics. The small dark particles were silicon which are mostly associated with the aluminium-rich phases.

Figure 62 showed at higher magnification the Al-rich former α' phase surrounded by η and β. This figure indicated spinodal decomposition of the α' for the lamellar β stops when reaching the α' phase. It has been well established that spinodal decomposition does occur in the Zn-Al system and that the results generally conform to the prediction of Chan's theory (109). The evolution of microstructure of a spinodally decomposed system has been found to consist of a number of stages. The spinodal stage occurs initially within the unstable region, and exists in the supersaturated α'-matrix. The next stage to follow is the coarsening stage, the distinct feature of this stage was found to be the continued existence of the well-interconnected microstructure which had not given way to a 'particulate' structure. In spite of significant coarsening occurring during this stage, all the structure had a remarkably high degree of interconnectivity. As can be seen from Figure 63, α and β lamellae of the decomposition products retained a high degree of interconnection. In general, the continuous reaction process which begins with the spinodal decomposition and ends with the appearance of coarse, discreet second phase particles is the result of a series of diffusion-controlled processes. Initially, in the spinodal stage, up-hill diffusion occurs in response to a thermodynamic requirement leading to a very fine multiply-connected structure. These inter-connected periodic lamellae are then found to coarsen by a gradual increasing in wavelength, involving a continuous adjustment in the position of the lamellae during coarsening. This is due to the steady build-up in the amplitude of the composition fluctuations at a constant wavelength, the coherency strains across the adjacent lamellae

increase, which in turn increases the elastic strain energy associated with the decomposition. This increase in the strain energy demands a decrease in the interfacial surface energy so that the total free energy is minimised. This is achieved by the attainment of a larger but more uniform interphase spacing. Finally, the attainment of discrete particles involves the break-up of the aligned lamellae at a constant lamellar spacing.

The structure of Cosmal was further examined using transmission electron microscopy. Figure 64 taken from an area similar to Figure 63 shows the spinodal decomposition clearly at higher magnification. This figure also shows a zinc-rich area in the centre of the micrograph which is surrounded by decomposed β. The phase transformation of this alloy was as follows:

$$\alpha'_s\,(+\sigma) \longrightarrow \beta + \eta(+\sigma)$$

Figure 65 shows in the centre of the micrograph, some decomposed β particles surrounded by α' phase, this micrograph was taken from a small area shown in Figure 63. What must be noted in this micrograph is the absence of any ε precipitates such as those shown in ZA27 and ZA8 (110). The reason for this is not known but the presence of Si and Mn or the absence of Mg may have altered the solubility of Cu in the η phase. Figure 66 shows an interdendritic η region in the centre surrounded by decomposed β phase. Also seen in this figure are chain-like tubular Al-rich phases and in the bottom right hand corner, large amounts of precipitates can be seen. A number of SADP'S were taken from different regions of Figure 66, one example of this diffraction patterns is shown in Figure 69 which corresponds to a beam direction of $[10\bar{1}\bar{1}]$ of CPH structure of η matrix. This figure also shows the points indexed and in

order to clarify the figure, a stereographic projection was established and the great circle on which points of index lie is shown, this proves further the absence of ε precipitates as the only phase present in the micrograph was a zinc-rich phase, (Figure 70). Figures 67 and 68 also show areas of decomposed β and also some zinc-rich regions. Notable also in these two micrographs is the absence of any ε phase precipitates whereas with 1% Cu there would normally be produced some dense precipitates. Analyses were carried out on the numbered regions of the two micrographs and the results show that in some cases (6 & 7) the composition of the alloy was in equilibrium with the original composition of the alloy. In some cases where zinc-rich η phase particles were examined Zn contents of as high as 99% were observed (2, 3 & 4) , the results are shown in Table 12.

5.7 Metallography of the Supercosmal Alloy

Super Cosmal has 60% aluminium and therefore, contained more aluminium than all the previously discussed alloys. Hence the amount of α' was much more, as is clearly demonstrated in Figure 71 .This figure shows the α' phase and a mixture of β and η, the black particle were analysed to be silicon and are mainly associated with the α' phase. The aluminium contents of the α' phase was also analysed and was higher than all previous alloys. Upon solidification the structure of this alloy can be described by two enlarging three-phase fields of α+β+σ,and β+η+σ, when the temperature falls to 266°C, the phase transformation β into α+η occurs. Below this temperature, β-phase transforms into the three phase α+η+σ, silicon has minor effect on phase boundaries, but stabilizes the β phase to lower temperatures. Figures 72 and 73 at higher magnifications

show the aluminium-rich α' phase surrounded by lamellarly decomposed β, these figures also indicate spinodal decomposition of α' as the β lamellae stop when they reach the α' phase this phenomena has already been discussed earlier. However since the aluminium content is high the lamellar of β phase is short and in some places the β phase looks nodular. At higher magnifications again it can be seen more clearly the dark particles of silicon are mostly associated with the α' phase, this is because silicon was evidently the first material to crystallise from the melt on cooling and had served as a nucleus for the alpha dendriites which appeared next. Figure 74 shows the lamellar decomposition of β more clearly this micrograph was taken at a different contrast to highlight this phenomena.

The structure of Supercosmal was further examined using transmission electron microscopy, Figure 75 taken from an area similar to Figure 73 shows on the bottom of the micrograph spinodal decomposition of α' shown as coarse particles. This is further proof that α' was decomposed spinodally.

A number of SADP's were taken from different regions of Figure 75, and one example of these diffraction patterns which was shown in Figure 79 corresponded to a beam direction of $[0\bar{1}3]$ of FCC structure of α' matrix. The SADP was taken from the arrowed area in Figure 75. This was also further proof of the α region existing in the micrograph.

At the top of the micrograph were decomposed β particles. Analyses were also made from the a region of the micrograph and are shown in Table 13. Figure 76 concentrates on a β region and shows decomposed β particles which had produced lamellae with different orientations. As with

the Cosmal alloy what was noticeable was the absence of ε-phase precipitates, the reason for this is not known but in this case may be attributed to the change in solid solubility which has been caused by the addition of silicon. The micrograph also shows a great deal of oxides which has appeared as a result of the polishing technique used. Figure 77 shows a silicon-rich particle in the left-hand side of the micrograph. This has been shown more clearly in figure 78. This particle was analysed and the result is shown in Table 13, the analyses shows that this particle had a composition of about 91% silicon. However as discussed earlier errors in the analysis are possible, one reason for the discrepancies could be due to the method of polishing used when preparing the specimens.

5.8 Damping of the Experimental Alloys

Damping tests were carried out initially on all experimental alloys using the modal analysis method. The results of this method are shown in Tables 14-16. This method allowed the analyser to be set at different frequency spans. This helped to obtain damping results from each mode of vibration, ie at 800 Hz the only mode of vibration excited was the first mode, the damping results of which are presented in Table 14. Figure 80 shows the plot of one such vibration mode. The damping values of these were then calculated using a software known as Spiders by the computer. As the frequency span was increased to 1.6 kHz and 3.2 kHz so increased the number of vibration peaks to 2 and 3 respectively. Therefore, damping could be calculated for 2 and 3 vibration peaks the results of these are shown in Tables 15 and 16. Plots of such peaks are shown in Figure 81 and 82. The results from all three different frequency spans showed not a great difference between each alloy. This was thought to be

due to the mass of the accelerometers attached to each specimen by wax during testing. As the weight of test pieces were small it was thought that the accelerometer's weight could have an effect on the result. One other discrepancy which occurred was that the damping values of alloys increased as the frequency span was increased this can be seen by comparing the damping results of the first mode of vibration in the three different frequency spans in the case of ZM11 it increased from 0.0164 to 0.0491 nearly a threefold increase as the span was increased from 800 Hz to 3.2 kHz. This can only be attributed to the fact that as the span got larger, the errors in the calculation also were greater. Therefore, accepting the frequency span of 800 Hz as the most accurate result Supercosmal proved to have the best damping capacity. However, this was not expected as Supercosmal contains 60% aluminium. Figure 85 shows at a glance each alloy's damping capacity compared with the others. Figure 86 shows that the damping capacity of all alloys reduces with increasing frequency, the rate of reduction is almost the same for all alloys.

In order to find a more reliable method for testing a further damping measurement technique was explored. This was the half power point method and involved fixing a specimen to an electrodynamic vibrator and sweeping slowly through the frequency range of 0-4000 Hz to excite the resonant frequencies damping was then calculated manually using the graphs produced by the plotter an example of such a graph is shown in figures 83 and 84. The results obtained from this method are shown in Table 17. This method also showed damping reduced as the frequency was increased. Figure 87 shows that all alloys had a reduced damping capacity this was very similar to the previous method and showed that all alloys had the same rate of decrease in the damping capacity. Figure 88 shows at a glance a comparison of the damping capacity of all

experimental alloys. This method also showed beyond all expectations, Supercosmal to have the superior damping capacity. Followed closely by ZM11. Because of the unreliability of the results and the fact that they produced some unexpected results, the two previous methods of testing were abandoned and a new method developed at Aston and was known as the Q-meter was adopted.

This method allowed Q^{-1} values to be calculated according to the following equation:

$$Q = \pi N/\lambda$$

where N = number of cycles as shown on instrument

λ = constant = Ln x1/x2 = 2.303

The damping results of all experimental alloys are shown in Tables 18-25 to ensure and prove consistency of results. Several tests were carried out on each alloy. Figure 89 shows at a glance the Q^{-1} values of all experimental alloy. This shows that ZA27H1 had the best damping capacity followed by ZM11 and ZA27H2. It is not surprising that these three alloys exhibited high damping capacity as ZM11 has eutectoid composition and ZA27H1 and H2 are very close to the eutectoid composition. The average damping levels observed for all alloys ranged from $0.43*10^{-3}$ for Supercosmal to $2.01*10^{-3}$ for ZA27H1. However, it is well known that damping capacity of Zn-Al alloy increased with increasing temperature in order to investigate this, tests were carried out at elevated temperatures, results of which are presented in Tables 26-33. As the results show, there is little doubt that ZA-alloys show increased

damping as function of temperature. This is due to thermally activated relaxation mechanisms associated with the internal boundaries of the materials. Figure 90 shows damping as a function of temperature for all experimental alloys. This figure shows that damping is lowest at room temperature and increases rapidly with increasing temperature in all experimental alloys and is highest for the eutectic and the near eutectic alloys. In fact as it can be seen very clearly in this figure, the alloys are almost separated into two groups with Cosmal, Supercosmal, ZA8, M3 and ZA27 showing very similar behaviour in one group (group 1) and ZA27H1, ZA27H2 and ZM11 showing similar behaviour in the other group (group 2).

In group 1 of the alloys, the aluminium contents ranges from 4 to 60%. Hence, there exists a large freezing range therefore, the result may depend on the cooling rate or microshrinkage caused by a wide range of solidification temperatures of the alloys. However, it seems surprising that ZA27 should lie within this group. This indicates that even a 1% reduction in copper contents has significantly increased the damping capacity of ZA27. The second group of alloys all showed superior damping capacity, the mechanism of damping in these alloys is not inconsistent with those of grain-boundary relaxation process. If the damping in these alloys is related to grain boundaries then it seems likely that the high magnitude of the damping is associated with the fine-grained two-phase microstructure of these alloys. It is likely with these alloys as with all experimental alloys, that chemically different boundaries ie Al/Al, Zn/Zn and Al/Zn will contribute to the damping . It is suggested that the increase in damping capacity of the eutectic alloy originates from a reversible grain-boundary sliding mechanism. This is supported by strong evidence for a sliding process being dominant during super-plastic

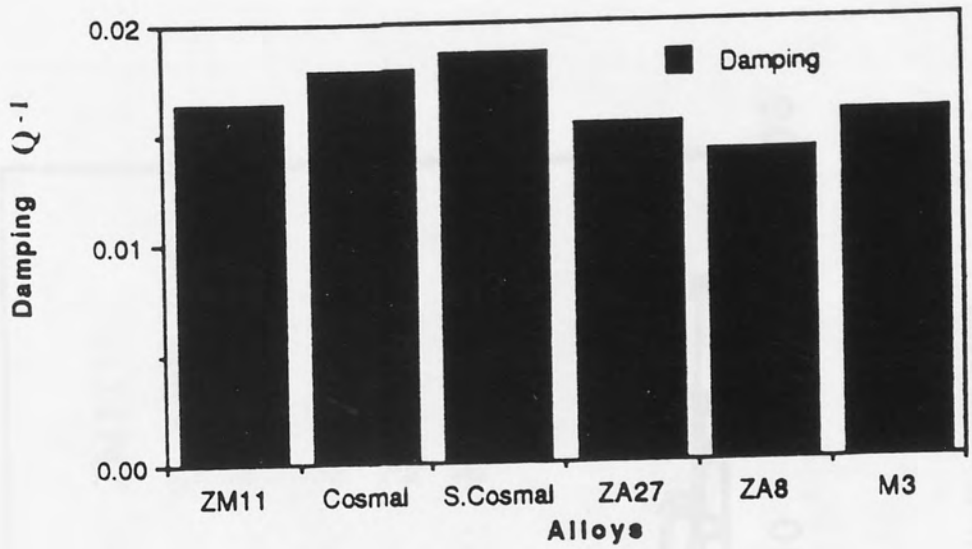

Figure 85: The damping capacity of the experimental alloys as obtained by the modal analyses method.

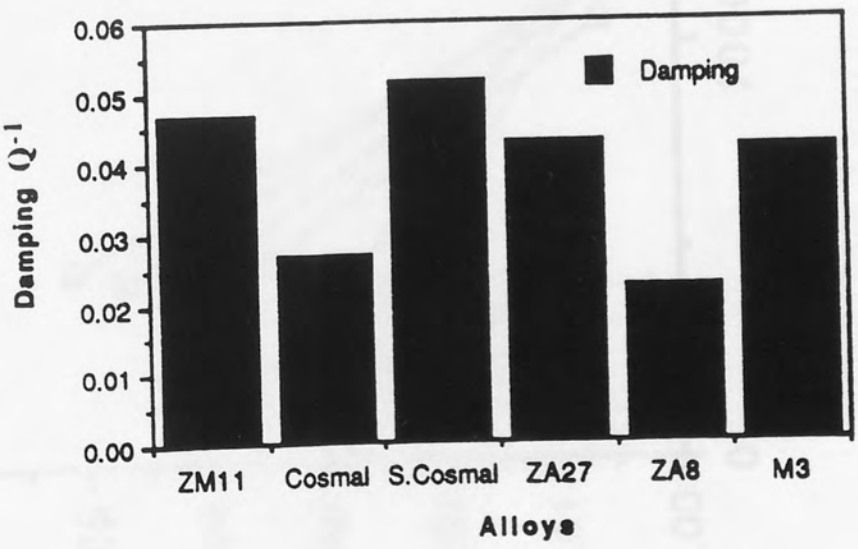

Figure 88: The damping capacity of the experimental alloys as obtained by the half power point method.

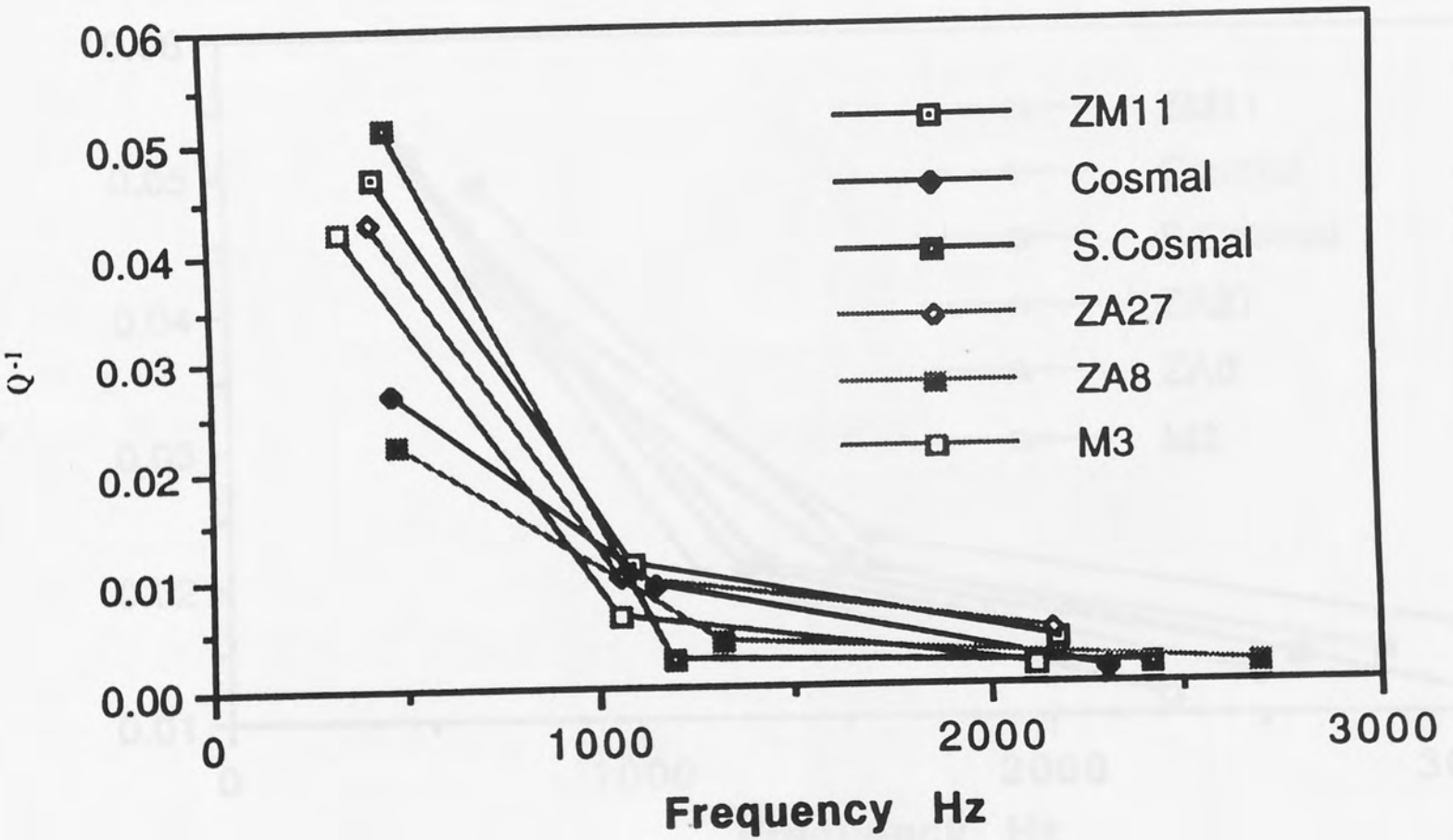

Figure 87: Damping capacity v frequency of vibration. (half power point method)

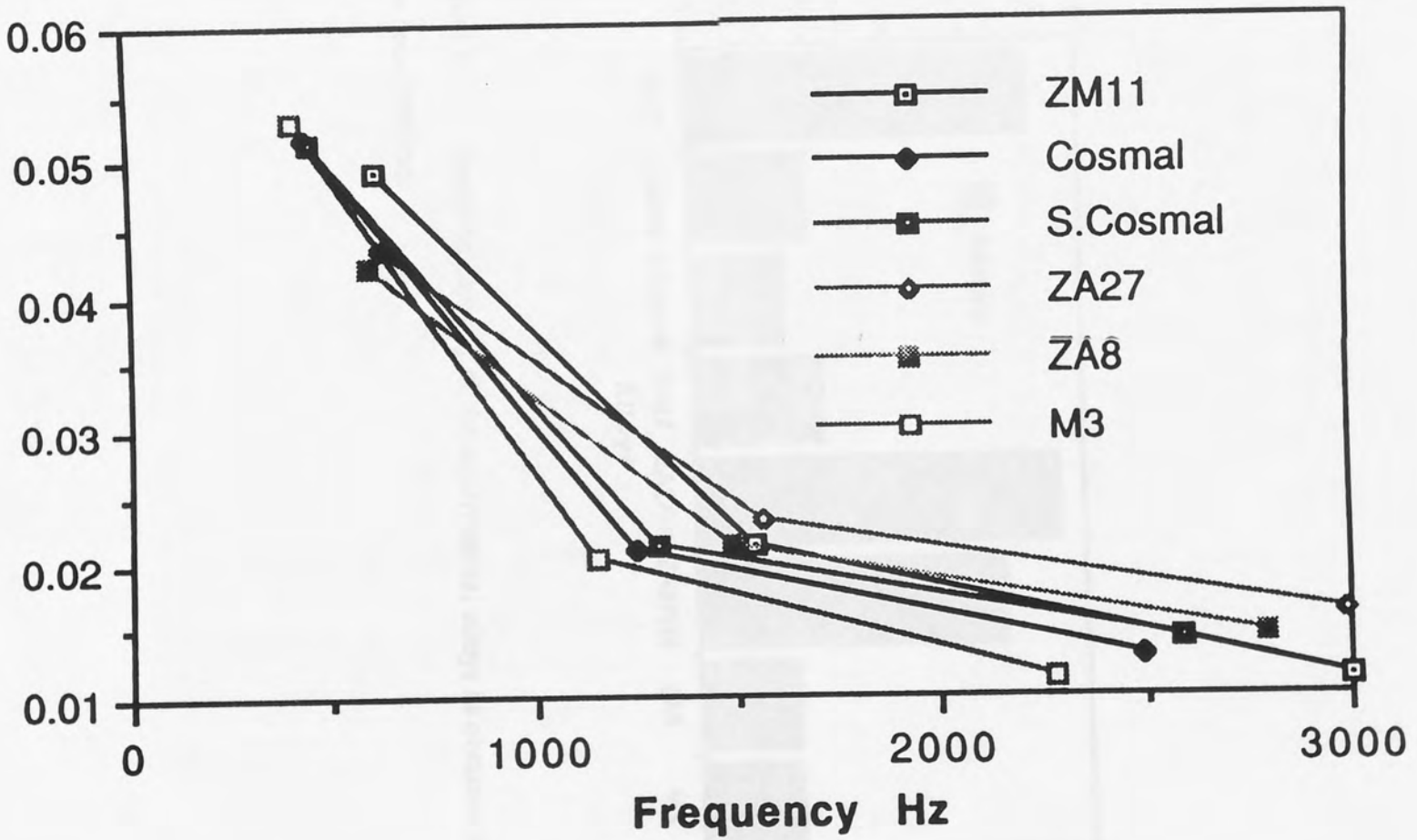

Figure 86 : Damping capacity v frequency of vibaration . (modal analyses method)

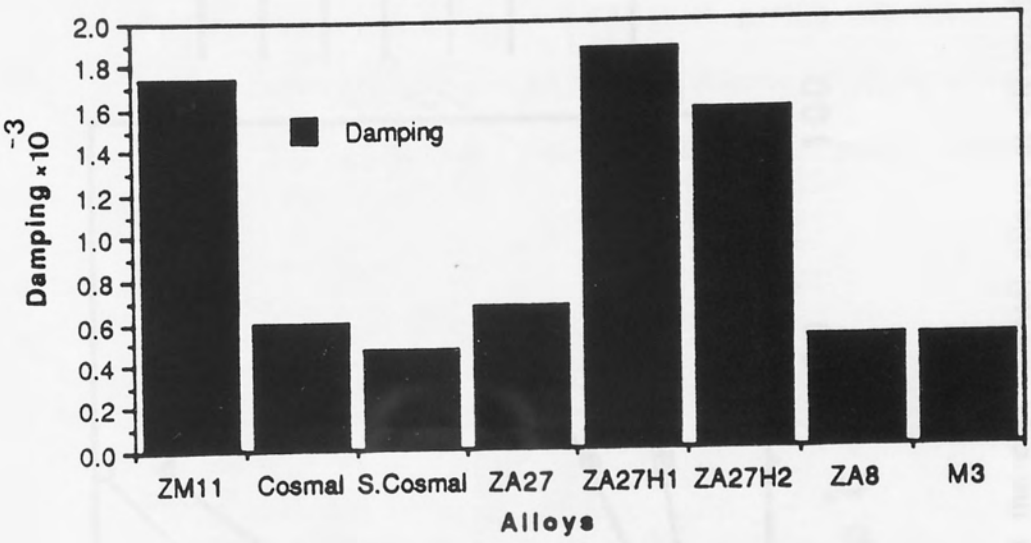

Figure 89 : Damping capacity of the experimental alloys as obtained by the free decay method.

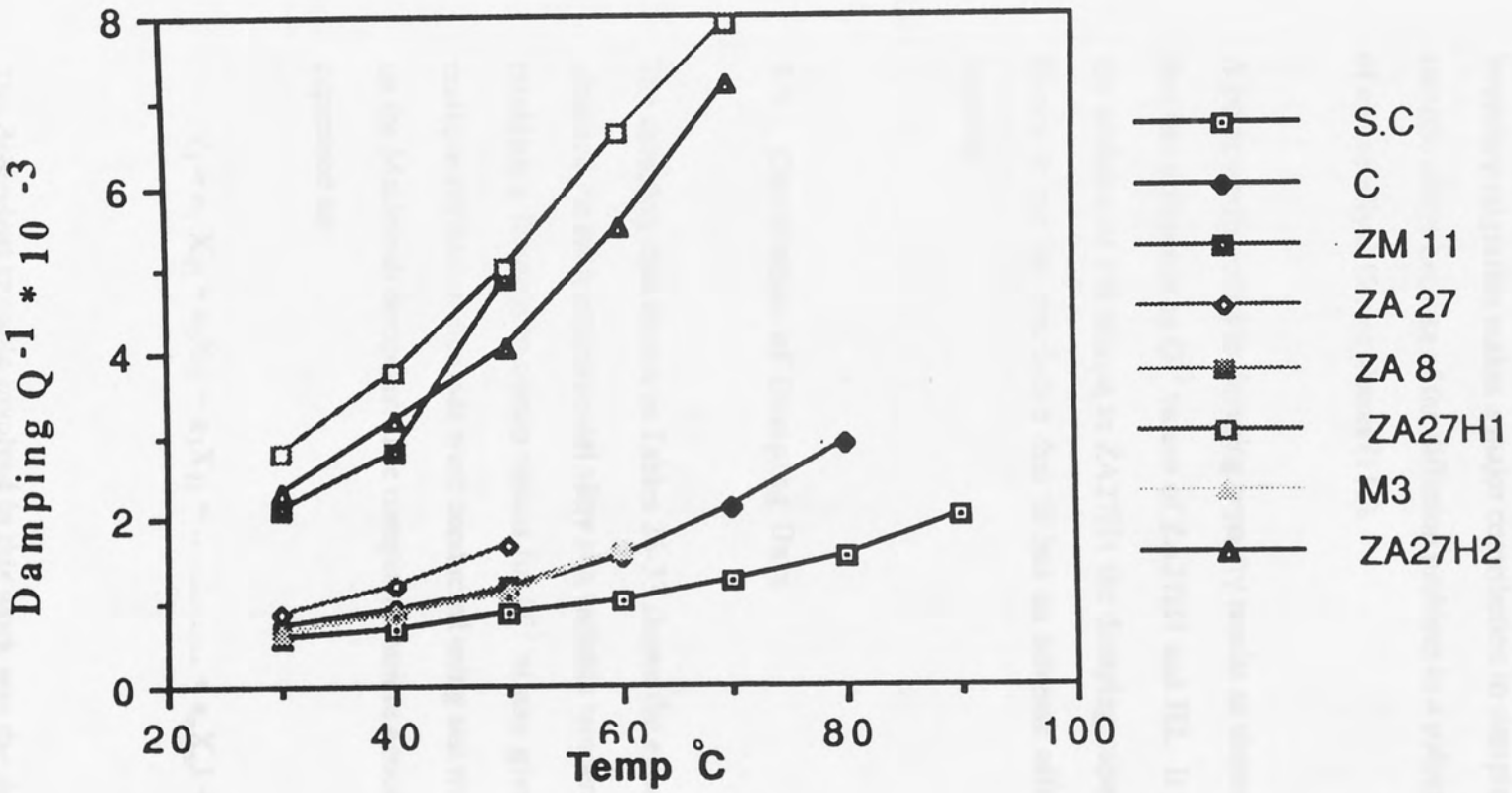

Figure 90: Damping capacity of the experimental alloys at elevated temperatures.

deformation (111, 112) and also by the observation of high damping in other super-plastic alloys. However, it is unlikely that reversible grain-boundary migration makes a major contribution to damping in the present eutectic alloys because of the diffusion problem in a polycrystal composed of chemically different phases (113).

A point worth noting in damping capacity results as shown in Figure 90 is that the difference in Q^{-1} values of ZA27H1 and H2. It is noted that by the addition of 1% silicon to ZA27H1 the damping capacity is lowered. Hence it can be concluded that Si has an adverse effect on damping capacity.

5.9 Correlation of Damping Data

The damping data shown in Tables 26-33 shows the experimental results obtained for each experimental alloy at a variable temperature in order to establish a formula to obtain values for Q^{-1} at any given temperature, multiple regression analyses were conducted using stat work II a program on the Macintosh computer. The computer assumes a model which can be expressed as:

$$Y_i = a_1 X_{1i} + a_2X_{2i} + a_3X_{3i} + \ldots\ldots\ldots\ldots + a_nX_ni + b + \text{error}$$

The dependent variable involved in this work was the damping capacity Q^{-1}. The independent variable was temperature in degrees Celsius. In order to obtain a greater degree of accuracy, one more independent variable was supplied to the computer. This was the inverse of the

Alloys	Formulas obtained from Multiple Regression Analyses	C.D.	C.C	S.E.E	D.W. Stat.
ZM11	Q^{-1}= -0.13355 + 0.00029T + 0.20484 1/T	0.93453	0.96672	0.00034	0.7524
Cosmal	Q^{-1} = -0.00374 + 0.0007T + 0.06696 1/T	0.97619	0.98803	0.00012	0.69245
S.Cosmal	Q^{-1} = -0.00015 + 0.000035T + 0.02952 1/T	0.97252	0.98616	0.00009	0.48062
ZA27	Q^{-1} = -0.00084 + 0.00005T + 0.00803 1/T	0.98272	0.99132	0.00005	0.56895
ZA27H1	Q^{-1} = -.00216 + 0.00014T + 0.01435 1/T	0.98658	0.99327	0.0025	1.14617
ZA27H2	Q^{-1} = -0.00516 + 0.00014T+ 0.01435 1/T	0.98819	0.99408	0.00021	0.4294
ZA8	Q^{-1} = -0.00149 + 0.00004T + 0.02260 1/T	0.98703	0.99344	0.00005	0.68389
M3	Q^{-1} = -0.00188 + 0.00005T+ 0.03004 1/T	0.97399	0.98691	0.00006	1.60582

Table 37: Damping capacity Q^{-1} predictions of experimental alloys at any given temperature.

Where : C.D = Coefficient of Determination
C.C= Coefficient of Corrolation
S.E.E= Standard Error of Estimate
D.W. Stat= Durbin- Watson Statistic

temperature (T^{-1}). The correlations corresponding to the above are shown in Table 37. The table shows the correlated prediction at any given temperature. The equations show a good degree of accuracy and in some cases, the correlated data nearly matched the actual data.

5.10 Tensile and Hardness Properties of the Experimental Alloys

Supercosmal revealed a superiority in its UTS values over the other alloys at all the above temperatures, as shown in Figure 91. The figure shows that at 25° C Super- cosmal had a UTS value virtually identical to that of its nearest rival ZA27 but this deficit increased sharply with increasing temperatures to 39% at 100° C. This difference was greater when compared with other alloys, it was 55% compared with ZM11 at 100° C. ZM11 showed the poorest UTS at elevated temperatures, Cosmal also showed low UTS values this can be attributed to the absence of Mg. With the exception of Cosmal for all alloys UTS was directly proportional to their aluminium contents. The high strength nature of α and α' are responsible for the high tensile strength of Supercosmal, compared to the M3 alloy which is dominated by the low strength η phase. It is also noticeable from Figure 94 that ZA27H2 showed lower UTS values at 50 and 75° C compared with ZA27H1, but showed a higher UTS value at 100° C. This is due to the presence of Si in this alloy which can also be responsible for the high UTS value of Supercosmal as it contains 6% Si. A reduction in the copper contents of ZA27 also seems to have decreased the UTS of ZA27H1 and H2. This is in agreement with a recent work carried out at Aston (114).

The hardness test results shown in Table 36 also reveal that Supercosmal has the superior hardness properties about 15% greater than its nearest rivals ZA27 and Cosmal. The results also show that ZA27H1 shows remarkably lower hardness compared with ZA27, this is again due to the reduction in copper contents however, in ZA27H2 shows higher hardness values very similar to ZM11.

Therefore, in applications where greater strength and hardness is required damping capacity needs to be sacrificed in order to accommodate for the designed needs.

5.11 Theoretical and Metallographical Considerations

It is widely accepted that Zn-Al alloys are considered to be most excellent non-ferromagnetic damping alloys, and several studies have all reported that damping of these alloys increase with rising temperature and all have attributed damping in these alloys to grain-boundary sliding. Nuttall (113) reported that a water-quenched Al-78% Zn alloy increases its damping capacity with rising temperature and showed a maximum at 200 °C, and also the very large damping was yielded by reversible sliding of the grain-boundary between the hard α and the soft β phases. Moreover Norwick (119) reported that the damping values of a furnace-cooled Al-40% Zn alloy with the lamellar microstructure increased continuously up to the eutectoid temperature by the coupled relaxation between the interfaces. Therefore the large damping in some of present alloys must arise from the grain-boundary effect which is operative at room temperature as well.

It is apparent that the grain-boundary effect on damping becomes larger with the increase in the boundary area. Accordingly, it is reasonable that damping of the alloys with finer grain, i.e. the larger boundary area should be higher.

The high damping capacities of the eutectoid and the near eutectoid alloy i.e. ZM11, ZA27H1 and H2 can be attributed to their fine grain size. ZM11 had fine (about 2 μm) α dendrites as seen in Figure 51. The α dendrites in turn were formed from nicely formed lamellae with an interlamellar spacing of approximately 0.15 μm. ZA27H1 showed mainly small α' dendrites of about 4μm and some larger α' dendrites of about 12 μm. ZA27H2 however showed a more uniform grain size of about 4μm. As the grain size of these alloys are quite small , and they showed good damping qualities it is safe to assume that grain-boundary sliding is the main factor contributing to damping in these alloys, and that damping is directly related to the metallographic structure of the experimental alloys.

The alloy M3 which showed very low damping properties compared with the other experimental alloys, had the least complex microstructure, consisted mainly of primary η particles set in a eutectic matrix as discussed earlier. ZA8 also showed poor damping, the structure of this alloy as seen in Figure 37 showed to have very rounded primary particles this was the same in M3, it was thought that grain-boundary sliding although effective was not the main mechanism contributing to damping in these alloy, and that the damping in these alloys could be due to the motion of dislocations as suggested by Granato and Lucke and described earlier in Chapter 2.

Cosmal and Supercosmal alloys also showed relatively poor damping, their microstructures consisted mainly of aluminium-rich α' phase, with particle sizes of between 8 and 10μm. It was not surprising that these alloys showed poor damping, because of their large aluminium contents, but these alloys proved to be more stable at elevated temperatures, up to 90° C. This would cover the range of temperatures found in under-bonnet applications in the automotive industry. Moreover, at temperatures in excess of 100° C, the creep and strength properties of the alloys would preclude their use in most applications. Cosmal and Supercosmal alloys as their chemical composition lies within the Norwick theory discribed earlier, there is possibility of damping arising from coupled relaxations between interfaces. Norwick suggested that the distribution of incoherent interfaces in relation to the sphere of relaxation of an individual interface is important, and that when the relaxation spheres overlap stress relaxation at one interface can produce a significant increase in the shear stress across a second interface, resulting in large non-elastic strains. However it is not clear whether or not this was the mechanism of damping in the present work for Cosmal and Supercosmal.

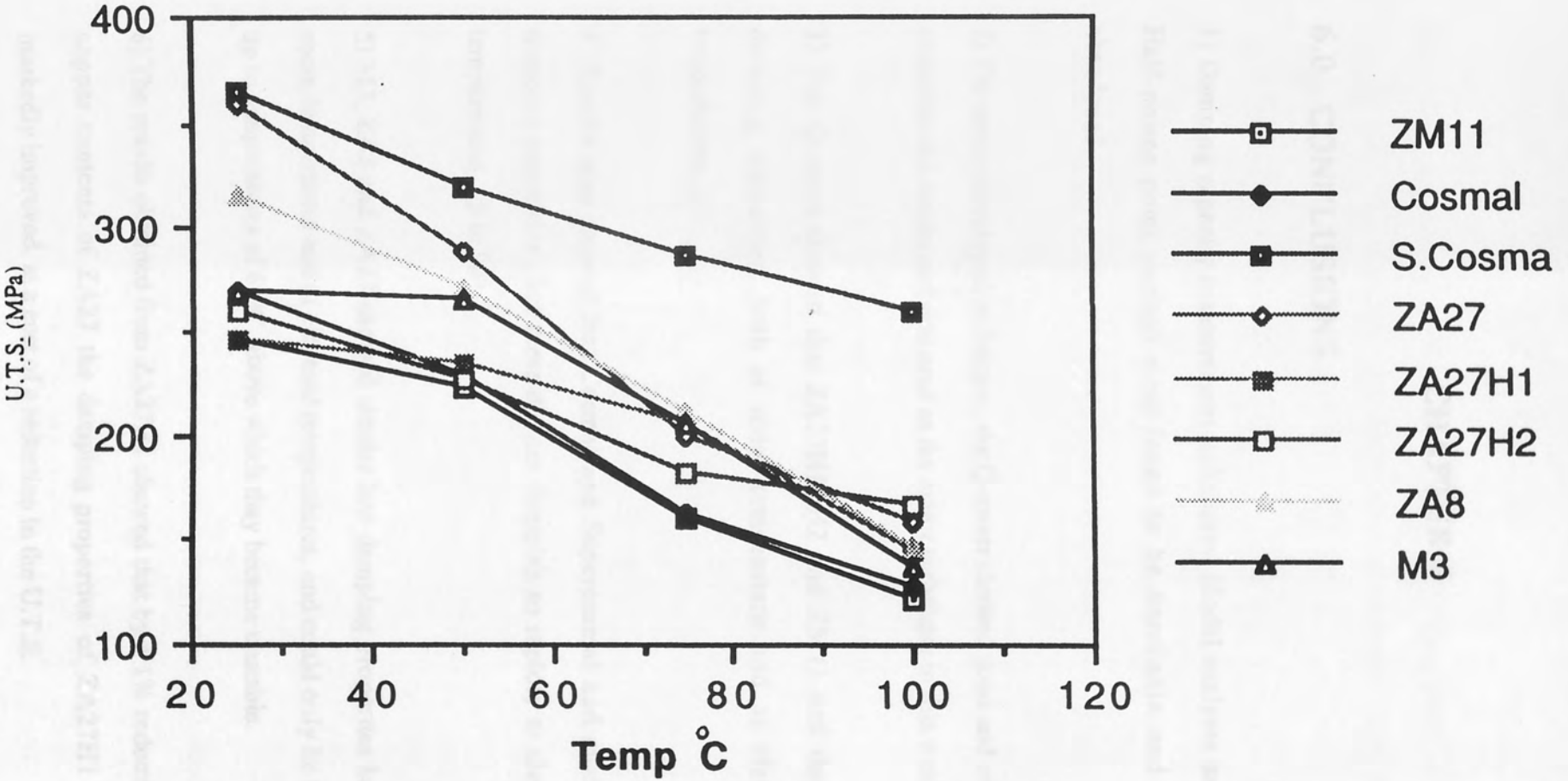

Figuer 91 : U.T.S v temperature

CHAPTER 6

6.0 CONCLUSIONS

1) Damping capacity measurement techniques, Modal analyses and the Half-power point method were found to be unreliable and later abandoned.

2) The newly developed technique , the Q-meter showed good and reliable experimental results and was used as the major technique in this work.

3) The Q-meter showed that ZA27H1, H2 and ZM11 had the best damping properties, both at room temperature and at elevated temperatures.

4) Results also showed that Cosmal and Supercosmal had moderate damping properties , but these did not diminish so rapidly at elevated temperatures, up to 90° C.

5) M3, ZA8 and ZA27 showed similar low damping properties both at room temperature and at elevated temperatures, and could only be tested up to temperatures of 60°C, above which thay became unstable.

6) The results obtained from ZA27H1 showed that by a 1% reduction in copper contents of ZA27 the damping properties of ZA27H1 were markedly improved, at a cost of a reduction in the U.T.S.

7) Supercosmal showed a similar tensile strength to that of ZA27 at room temperature, but was much more stable and stronger at elevated teperatures, up to 39% stronger at 100° C.

8) ZA8, ZA27H1, ZA27H2, M3, and the Cosmal alloys all showed simillar tensile properties both at room temperature and at elevated temperatures.

9) The Cosmal alloy despite its high aluminium content, showed very low tensile properties due to the absence of Mg in this alloy.

10) The hardness test results revealed Supercosmal to have the superior hardness, followed closely by Cosmal and ZA27. ZA27H2, ZM11, and ZA8 all showed very similar hardness values.

11) ZA27H1 showed that a 1% reduction in its copper content compared to ZA27 had drasticaly reduced its hardness values by 46%. M3 showed a similarly low hardness value.

12) The reason for large variation in damping capacity, tensile strength and hardness of the experimental alloys was due to thire microstructure.

13) The main damping mechanism found in all experimental alloys was thought to be that of grain-boundary sliding, most alloys showed very fine grain sizes, which can contribute to high damping capacity.

14) The absence of ε-phase precipitates in the Cosmal and the Supercosmal alloys was thought to be unusual as they contained over 1%

copper, however this was attributted to a change in the solid solubility of the alloys, which might have been caused by the addition of silicon.

15) The SEM micrographs revealed no signs of phase transformation which might happen at test temperatures of 100° C.

CHAPTER 7

7.0 Suggestions for future work

1) The damping properties of the as-cast alloys at room temperature and at elevated temperatures have been determined, but it is necessary to carry out heat treatment on the experimental alloys to ascertain the optimum damping capacity of these alloys.

2) Further TEM and SEM micrographs should be obtained from the heat treated alloys to compare their microstructures with those of the alloys in the present work.

3) Testing of 70/30 manganese-copper alloy is required to compare its damping properties to those of the zinc-aluminium alloys used in the present work.

4) ZA27H1 and ZA27H2 were examined by SEM to study their microstructures. The SEM showed that there was no structural difference between these alloys and that of ZA27, except for some intermetallic particles in the case of ZA27H1 and some dark silicon prticles in the case of ZA27H2. Further TEM work might reveal the reason for the great differences between these alloys.

REFERENCES

1) BNF Guide to better aluminium diecasting. The British non-ferrous metals research association, Grove Laboratories, Wantage, Berkshire, Nov, 1973.

2) Upton B. Pressure diecasting, Part 1, Metal Machines, Furnaces, 1st Ed. Pergamon Press Ltd. 1982.

3) M Durman. The creep behaviour of pressure die-casting Zn-Al based alloys. Ph.D. Aston University, June 1989.

4) K. Sawalha. The fatigue behaviours of pressure diecasting Zn-Al based alloys. Ph.D. Aston University, March 1991.

5) Loong C.A., Gervais E. and Lefebrer M. Properties and die-casting ZA alloys. Tran 13th SDCE Int. Diecasting congress and exposition paper No. G-T85-055. June 3-6, Milwakee USA, 1985.

6) Gervais E., Kandeil A.Y. and Levert H. Properties and diecasting of the Zn-27% Al-2% Cu-0.01% Mh alloy. 11th SDCE Int. diecasting congress paper No. G-T81-086, Cleveland Ohio, June 1-4 `1981.

7) Yorgladis A. Damping capacity of materials Pro. Eng. 1954.

8) James D.W. High damping metals for engineering applications. Mat. Sci. and Eng. 1969 p. 1-8.

9) Lazan B.J. Stress-strain-times. Relations for idealised material. A.S.T .M. 1962.

10) James D.W. High damping metals for engineering applications, Mat. Sci. and Eng. 1969 4 p 1-8.

11) Koehler. Imperfections in nearly perfect crystals (John Wiley and Sons Inc, New York 1952).

12) Granato A , Lucke K. J. Appl. Phys. 27, 583 (1956)

13) Granato A., Lucke K. J. Appl. Phys. 27 789 (1956).

14) Lucke K. and Granato A. Dislocation and mechanical properties of crystals (John Wiley and sons Inc, New York 1957).

15) Swartz J.C. and Weertman J. Modification of the Koehler-Granato-Lucke dislocation damping theory. J Appl Phys V32 1961.

16) Murphy S. Lecture notes Dept Metallurgy, Aston University, Birmingham.

17) Zener C.H. Elasticity and anelasticity of metals. University of Chicago Press, 1948.

18) Lazan B.J. Damping of material and members in structural mechanics. Pergamon Press 1968.

19) Ibrahim S.F. AIAA Journal 22, 817-823, 1984.

20) Wentz K.R. and Les J. Mechanical system and signal processing. Vol 1, No. 4, 4 Oct 1987.

21) Jensen J.W. Damping capacity. Its measurement and significance. U.S Bureau of Mines, Washington (1959).

22) Beards C.F. Structural vibration analysis. Ellis Horwood series 1983.

23) Pisarenko. Dissipation of energy during mechanical vibration. Vol 1, 1962.

24) Nashif A.D. Vibration damping, 1985.

25) Zener C. Elasticity and anelasticity of metals. University of Chicago Press, 1948.

26) Jensen J.W. Damping capacity, its measurement and significance. U.S. Bureau of Mines, Washington, 1959.

27) Ke T.S. J. Appl Phys 2D 1949, 274.

28) Nuttal K. J. Inst Metals 99 1971. P. 266-271.

29) Nuttal K. and Nicholson R.B. Phil Mag. 17. 1968, 1082.

30) Chaudari. Acta Met 15, 1967, 1777.

31) Hayden, Gibson and Brophy. Sci. American 220, (3) 1969 28-35.

32) Holt D.L. and Backhofen W.A. Trans ASM 59 1966 755-768.

33) Johnson, Packer, Anderson and Sherby. Phil. Mag. 18, 1968, 1309-1314.

34) Brophy and Parker. Trans ASM 24, 1936, 919.

35) Kimball. Trans ASME 63 1941 A135-140.

36) Macy and Sakono-Oku. Central Research Inst. Mitsubishi Metal Corp (1985).

37) Murray J.L. Bulletin of alloy phase diagram, Vol 4, Vol 1 55-73 1983.

38) Mondolfo Lif. Aluminium alloys-structure and properties. Butterworth London 1976.

39) Mykura N. Zhu Y.H., Murphy S. Canada Metallurgical Quarterly Vol 25 No. 2. pp151-159 1989.

40) Hanson D and Gayler M.L.V. J. Inst Met Vol 27 267-306. 1922.

41) Tanabe T. J. Inst Met V.32 415-453. 1924.

42) Isihara T. J. Inst Met V.32 73-990 1925.

43) Owen E.A. and Pickup L. Phil Mag. Vol 20 761-777, 1935.

44) Ellwood E.C. J. Inst. Met Vol 66 87-96, 1940.

45) Ellwood E.C. J. Inst Met. Vol 80 217-227. 1951-1952.

46) Fink W.L. and Willey L.A. Trans American Inst Min Met Eng Vol 122 244-265, 1936.

47) Grayler M.L.V. and Sutherlank E.G. J. Inst. Met. Vol 63, 123-147, 1938.

48) Presnyakov A.A., Gorban Yu., Chervyakova V.V. Russian Journal of physical chemistry, Vol 35, No. 6. 632-600, 1976.

49) Goldak G.R. and Parr J.G. J. Inst. Met. Vol. 92, 230-233, 1963-64.

50) Mondolfo L.F. Aluminium alloys-structure and properties. Butterworth, London 1976.

51) Zhu Y.H. Ph.D. Thesis, Aston University, 1983.

52) Hansen M and Anderko K. Constitution of binary alloys, 2nd ed. McGraw Hill Book Co. USA. 1958.

53) Metals Handbook. Phase diagram of binary alloy system. 8th ed. Vol 8. American Soc. of Metals, Ohio, 1973.

54) Pearson W.B. A handbook of the lattice spacing and structures of metals and alloys Vol. 2. Pergamon Press, London, 1967.

55) Lohberg K. Rontgenographische Bestmmung des Losurgsvermogens des zink fur aluminium uncl kupfer. Z. Metallkunde, Vol 32 86-90, 1940.

56) Lohberg K. Z. Metallkunde Vol 32. 86-90 1940.

57) Massalski T.B. and King H.W. Acta Met., Vol. 10, 1171-1181, 1962.

58) Zhu Y.H. Ph.D. Thesis, Aston University, 1983.

59) Savaskan T. Ph.D. Thesis, Aston University, Birmingham, 1980.

60) Gurnler A. Solid State Physics. Vol 9, Academic Press, New York p.294, 1959.

61) Borelins G. J. Metals 3 (1951) pp447-484.

62) Merz W and Anantharamen T.R. Phys Status Solidi 8(1965) KJ.

63) Merz W, Gerold V. Z Metallk, 57, (1966).

64) Wahl R.P. Corr. Sci, 38 (1969) 1.

65) Simerska M and Synecek Y. Acta Metall 15, (1967) pp 223-230.

66) Carpenter G.J.C. and Garwood R.D. Met. Sci. J. 1 (1967) p. 202.

67) Wahl P.P. and Ros V.V.P.M. K. Trans. Inst. Metals 23 (1970) 20.

68) Krishna K and Herman H. Met Sci and Eng. 1 (1966) p. 262.

69) Strongiss B.G. Phys Met Metallog 23 (1967) p.55.

70) Nikkwiski T and Sumbulli. Mat. Sci. J. 3 (1969) p.23.

71) Anantharaman T.R. Ramas V, and Butler E.P. J. Matls. Sci 9 (1974) p. 240.

72) Krishan K and Herman H. Matls. Sci and Eng (1966-67) p. 162.

73) Kleschev G.V and Sneynkman A.J. Phys. Met and Metallog. 23, (1961) p 56 and 173.

74) Anantharaman T.R. and Satyanarayanu K.G. Scripta. Met 7 (1973) pp 189-192.

75) Carpenter G.J.C. and Garwood R.D. Metals SCI J. Vol 1 pp 202-216. 1967.

76) Simerska M and Syneck V. Acta Metall vol 15. pp 223-230, 1967.

77) Neissmann S and Kirtain M. J. Appl. Phys 42 (1971) pp 2603-2611.

78) Simerska M and Synecek V. Acta. Metall Vol 5 , pp223-230 (1967).

79) Carpenter G.J>C. and Garwood R.J. Met. Sci. J. Vol 2 pp202-211 (1967).

80) Jacobs M.H. Met. SCI. J. Vol 6 pp.143-148 (1972).

81) Ramaswamy R.P. and Anantharman T.R. Acta. Metall. Vol 30, pp 1147-1155. 1982.

82) Vijayalakshmi M and Seetharaman V. Acta Metall. Vol 30, pp 1147-1155. 1982.

83) Vijayaalakshmi M and Seetharaman V. Mat. Sci. Eng. Vol. 52 pp 249-256. 1982.

84) Fournelle R.A. and Clark J.B. Metall. Trans Vol 3 pp 2757-2767. (1972).

85) Boswell P.G. and Chadwick G.A. Acta Metall Vol 25 pp 779-792. (1977)

86) Cheetham D. and Ridley N. J. Metals Vol 99 pp 371-376 (1971)

87) Garwood R.D. and Hopkins A.D. J. of the Inst of Metals Vol 81. pp 407-415 (1952-53).

88) Ardell A.J. and Nuttal K. Proc. International conference, University of Manchester. The metallurgy committee of the Institute of Metal. pp 22-26 (1966).

89) Panserr C.P. and Federighi T. Acta. Met Vol. 8 p.217. (1960).

90) Huston L. and Oahi J.W. Acta Met. Vol 14 p.1503. (1960)

91) Toldin V.A. and Sibumilov G.V. Fiz. Metal Metalloved Vol. 40, No. 6, pp.1223-1226. (1975).

92) Zhu Y.H. Ph.D. Thesis. Aston University, Birmingham. 1983.

93) Apelian D. and Pallval M. J. Metals. Vol 33, pp12-20, Nov 1981.

94) Morgan S.W.K. Zinc and its alloys, industrial material series, MacDonal and Evens Ltd.

95) Engineering properties of zinc alloys, published by Int. Lead Zinc Research Organisation. 2nd Ed. N.Y. 1981.

96) Mazak zinc alloys for pressure diecastings. A booklet for designers. Mazak Ltd. Bristol UK 1972.

97) Loog C.A. and Gerivais E. Trans 13th SDCE Int. diecasting congress and exposition paper No. G-785-055 June 3-6 Milwakee USA, 1985.

98) Bess M. and Loog C.A. Trans 13th SDCE Int. diecasting congress and exposition. June 3-6, Milwakee USA, 1985.

99) Rutherford J. Trans, 13th SDCE Int diecasting congress and exposition. June 3-6, Milwakee USA 1985.

100) Murphy S., Hill J., and Durman H. Creep behaviour of commercial pressure diecast zinc alloys presented at 12th Int pressure diecaster of Florence, Italy, 1987.

101) Mao Y and Sakong Oka. New diecasting alloys with high damping capacity. Central Research Institute, Mitsubishi Metal Corp. Ohmiya, Saltma 330, Japan.

102) Gervais E. and Bess M. 84th Casting congress and exposition, and published in the transactions of the American Foundrymens Society. St. Louis, Missouri, USA April 21-25, 1980.

103) Blouke M.M. Holonyak N. and Zwicker H.R. J. Phys. Chem. Solids 1970, p.31 and 173.

104) Thurmond C.D. and Kowalchik M. Tech. J. 1960, 39, 169.

105) Morell P.J. United States Patent No. 1815479, application field 18 June 1930 (serial No. 462141) Patented 21 July 1931.

106) Wasserman E and Falk H. Z. Metallkd, 1969 100, 623.

107) Snoek J.L. Internal damping of ferromagnetic materials, Nederland, Tydschr. Natuurkunde, 8, 177-179, 1941.

108) Durman M. Creep of Zn-Al alloys. Ph.D. Thesis. 1989. Aston University, Birmingham.

109) Chan J.W. Ibid 10 (1962) 179.

110) Durman M. Ph.D. Thesis. Aston University, 1989.

111) Gifkins J. J. Inst Metals, 1967, as, 373.

112) Lee D. Acta Met 1969, 17, 1057.

113) Nuttal K. Phil Mag 1968, 17, 1087.

114) Sawalha K. Ph. D. Thesis 1991. Dept of Mech. Eelec Eng Aston University.

115) Murphy S. Solid phase reaction in low copper part of Al-Cu-Zn system. Z Metallkunde Vol. 71, 96-102, 1980.

116) Jacobs M. Morphology of crystal structure of new precipitate in rapidly quenched aluminium-zinc alloy. Met Sci J. Vol. 6. 143-148.

117) Simerska M., and Synecek V. The mechanism of structure transformation in supersaturated Al-Zn alloys. Acta Metall Vol. 15 223-230, 1967.

118) Merz W. and Anantharman T.R. Phys Status Solid Vol. 8 K5, 1965.

119) Nowick A.S. J. Appl Phys 22 (1951) 923.

120) Durman M. and Murphy S. Acta Metall Vol. 39 No 10 pp 2235-2242 1991

121) Durman M.Sawalha K. and Murphy S. Mat.Sci. and Eng. A130 (1990) 247-256